

The Off-Line Computation System for
Supervising Performance of JOYO
—JOYPAC System—

Part 2

The Detailed Calculation Subsystem Predicting
the JOYO Nuclear and Thermo-Hydraulic Characteristics
— HONEYCOMB, FDCAL and FATEC Codes —

October, 1976

日 本 原 子 力 研 究 所

Japan Atomic Energy Research Institute

JAERI レポート

この報告書は、日本原子力研究所で行なわれた研究および技術の成果を研究成果編集委員会の審査を経て、不定期に刊行しているものです。

研究成果編集委員会

委員長 山 本 賢 三 (理事)

委 員

赤石 準 (保健物理安全管理部)	佐々木吉方 (研究炉管理部)
朝岡 卓見 (原子炉工学部)	佐藤 一男 (動力炉開発・安全性研究管理部)
天野 恕 (製造部)	田川 博章 (原子炉化学部)
石塚 信 (動力試験炉部)	田中 正俊 (核融合研究部)
石原 豊秀 (安全管理室)	長崎 隆吉 (燃料工学部)
伊藤 太郎 (企画室)	能沢 正雄 (安全工学部)
大内 信平 (材料試験炉部)	浜口 由和 (物理部)
大森 栄一 (技術情報部)	原田吉之助 (物理部)
岡下 宏 (原子炉化学部)	平田 実穂 (動力炉開発・安全性研究管理部)
小幡 行雄 (核融合研究部)	堀田 寛 (研究部)
栗山 将 (開発試験場)	

入手 (資料交換による)、複製などのお問い合わせは、日本原子力研究所技術情報部 (〒319-11 茨城県那珂郡東海村) へ、お申しこみください。なお、このほかに財団法人原子力弘済会情報サービス事業部 (茨城県那珂郡東海村日本原子力研究所内) で複写による実費頒布をおこなっております。

JAERI Report

Published by the Japan Atomic Energy Research Institute

Board of Editors

Kenzo Yamamoto (Chief Editor)

Jun Akaishi	Hiroshi Hotta	Masao Nozawa	Kazuo Sato
Hiroshi Amano	Toyohide Ishihara	Yukio Obata	Hiroaki Tagawa
Takumi Asaoka	Makoto Ishizuka	Hiroshi Okashita	Masatoshi Tanaka
Yoshikazu Hamaguchi	Taro Ito	Eiichi Omori	
Kichinosuke Harada	Isamu Kuriyama	Shinpei Ouchi	
Mitsuho Hirata	Ryukichi Nagasaki	Yoshikata Sasaki	

Inquiries about the availability of reports and their reproduction should be addressed to the Division of Technical Information, Japan Atomic Energy Research Institute, Tokai-mura, Nakagun, Ibaraki-ken, Japan.

編集兼発行 日本原子力研究所
印刷 三美印刷株式会社

JAERI 1247 Errata

Page	Line	Printed	To be corrected
3	↓ 1	possibel	possible
5	↓ 23	Fig. 2.1.3—1.	Fig. 2.1.3.
7	↑ 10	There are <u>such</u> many	There are <u>many</u>
7	↑ 4	analysi <u>s</u>	analys <u>e</u> s
10	Eq. of β_{eff}^m	$\overline{\cdots \sum_i \chi_p^i \phi^{*i}} dV$	$\overline{\cdots \sum_i \chi_p^i \phi^{*i}} dV$
17	↓ 16	stand <u>alone</u>	stand- <u>alone</u>
24	↑ 7	(j_1, i) <u>n</u> eans	(j_1, i) <u>m</u> eans
25	Eq. (4)	$a_{2,i,i+1}^n = \cdots$	$a_{2,j,i+1}^n = \cdots$
27	↑ 2	$\underline{\phi}_{jik}^n = \begin{cases} \phi_{j-3,i-3,k}^n, \cdots \\ \underline{\phi}_{jik}^n, \cdots \end{cases}$	$\underline{\phi}_{jik}^n = \begin{cases} \phi_{j-3,i-3,k}^n, \cdots \\ \underline{\phi}_{jik}^n, \cdots \end{cases}$
28	↓ 2	<u>A</u> round	<u>a</u> round
29	↑ 7	grad $\phi = (\vec{\phi}_2 - \underline{\phi}_1)/t$	grad $\phi = (\vec{\phi}_2 - \vec{\phi}_1)/t$
30	↓ 16	<u>b</u> = 2t. While ...	<u>a</u> nd b = 2t. While ...
36	↑ 3	$S_{ijk}^q = \cdots$	$S_{jik}^q = \cdots$
38	↓ 4	$\Sigma_s^{g \rightarrow h} = \sum_{i \in g} \cdots$	$\Sigma_s^{g \rightarrow h} = \sum_{i \in g} \cdots$
43	↓ 4	$\cdots = -\frac{1}{2} \underline{\delta}(s_0).$	$\cdots = -\frac{1}{2} \underline{f}(s_0).$
44	↑ 7	2.5.3.7 Example ...	2.5.3.7 Examples ...
56	Table caption	$\cdots, Z: ZPR-3-6 F^{(45)}$	$\cdots, Z: ZPR-3-6 F^{(24)}$
61	↑ 16	\cdots auxiliary and emergency	\cdots auxiliary _____
61	↑ 15	cooling systems and ...	_____ and ...
62	Fig. 3.2.1-1	Fuel Irradiation Pot	Material Irradiation Pot
64	↓ 18	\cdots two equations ⁵¹⁾ , ...	\cdots two equations ²⁵⁾ , ...
77	↑ 19	SMART- <u>M</u> ASTOR	SMART/ <u>M</u> ASTOR
91	↓ 17	Format	Formats
91	↓ 17	for <u>p</u> hoton Production	for <u>P</u> hoton Production

The Off-Line Computation System for Supervising Performance of JOYO —JOYPAC System—*

Part 2

The Detailed Calculation Subsystem Predicting the JOYO Nuclear and Thermo-Hydraulic Characteristics —HONEYCOMB, FDCAL and FATEC Codes—

Tomoo SUZUKI, Akira HASEGAWA, Masayuki AKIMOTO,
Yoshiaki MIYAMOTO and Satoru KATSURAGI

Working Group on Fast Reactor Safety Analysis Codes,
Nuclear Code Committee of Japan,
Japan Atomic Energy Research Institute,
Tokai-mura, Naka-gun, Ibaraki-ken

Received June 21, 1976

The calculation codes HONEYCOMB, FDCAL-2 and FATEC-3 have been programed for the purpose of developing a series of computer programs to be capable of predicting the detailed and fundamental informations about the core characteristics indispensable for supervising operational performance of the Japan Experimental Fast Reactor "JOYO".

HONEYCOMB is a code for detailed calculations in analyzing nuclear characteristics of the reactor. It performs criticality calculation in diffusion model and burn up calculation, for 3-dimensional hexagonal-z geometry. It can predict the critical insertion depth of control rods and calculate the 3-dimensional power distribution required by thermo-hydraulic calculation. Power distribution and burn up are also obtained for fuel pins, if necessary, as well as for assemblies.

FDCAL-2 predicts coolant flow distribution in every coolant channel between inlet and outlet plenums in the reactor vessel. In calculating the flow distribution in the assemblies, the sub-channel model is used, and the thermal mixing effect is expressed in terms of an apparent heat transfer coefficient.

FATEC-3 calculates temperature distribution within some assemblies, optionally specified in the given core matrix. At the same time, it estimates the hot-spot temperature, one of the informations for confirming the safe operation.

FDCAL-2 and FATEC-3 have been combined so as to remove their unnecessary overlapping parts, and have consequently formed a detailed calculation code for analyzing thermo-hydraulic characteristics of the reactor, FDCAL-3. FDCAL-3 has been linked to HONEYCOMB as a segment of overlay structure, and this combination of HONEYCOMB and FDCAL-3 forms the

* Work performed under the contracts between Power Reactor and Nuclear Fuel Development Corporation and Japan Atomic Energy Research Institute.

detailed calculation subsystem in the JOYPAC system.

The detailed calculation subsystem produces the data file of the detailed fundamental informations such as distributions of neutron flux, power etc. about the reactor under stationary performance. This file is required by the quick and simple calculation subsystem SMART and the recording subsystem MASTOR described in Part I. The code SMART predicts the various characteristics changes in a short term, utilizing the informations stored in this file. Thus, times of resorting to the time-consuming detailed calculation are reduced as far as possible, and supervision of reactor performance is realized in both features of practically sufficient accuracy and reasonable computer cost.

In this Part 2, the outline of the detailed calculation subsystem is described mainly about their functions and methods of calculation.

「常陽」運転監視用オフラインコードシステム

——JOYPAC システム——*

第 2 部

「常陽」詳細核熱水力特性解析サブシステム

——HONEYCOMB, FDCAL, FATEC コード——

日本原子力研究所

原子力コード委員会 原子力コード評価専門部会

高速炉安全性コード開発ワーキンググループ

鈴木友雄, 長谷川明, 秋元正幸, 宮本喜晟, 桂木 学

1976 年 6 月 21 日 受理

高速実験炉「常陽」の運転監視に必要な基本的な詳細データを提供できる計算プログラムを開発することを目的として、詳細計算コード HONEYCOMB, FDCAL-2 および FATEC-3 が作成された。HONEYCOMB は 3 次元六角- z 格子体系を対象に、拡散モデルによる臨界計算と燃焼計算を行う詳細核特性解析コードであり、制御棒挿入深度予測と熱水力コードから要求される詳細熱出力分布の算出も行う。さらに必要に応じて燃料ピン毎の熱出力や燃焼の計算を行うことが出来る。FDCAL-2 は炉容器内の下部プレナムから上部プレナムへ至るすべての冷却材流路の流量配分を計算する。集合体内の流量配分はサブチャンネルモデルを用いて計算され、熱的混合効果は見掛けの熱伝達率として表わされている。FATEC-3 は与えられた炉心構成における任意の集合体の内部において温度分布の計算を行い、安全性確認の一つのデータであるホットスポット温度の算出も併せて行う。FDCAL-2 と FATEC-3 は重複した部分が多いので、両者を結合して詳細熱水力特性解析コード FDCAL-3 としてまとめ、FDCAL-3 をオーバーレイ方式で HONEYCOMB に結合して、JOYPAC の中の詳細計算サブシステムを構成する。この詳細計算サブシステムは、第 1 部に述べた簡易計算ならびに記録用サブシステムが必要とする定常運転時の基本的な詳細データ（中性子束分布、熱出力分布等）のファイルを作成し、短期的な特性変化の予測は、簡易計算サブシステム SMART が、この詳細データファイルを基に計算する仕組みになっている。このようにして、計算時間が長くなる詳細計算を行う回数を出来るだけ少くして、運転監視を実用上十分な精度と計算費用の両面から実現しようとしたのである。この第 2 部では詳細計算サブシステムの概略について、その機能や計算法を中心に報告している。

* 本報告書は、日本原子力研究所が動力炉・核燃料開発事業団の委託により行った研究の成果である。

Contents

1. Introduction	1
2. HONEYCOMB, the Detailed Calculation Subsystem	
Predicting the JOYO Nuclear Characteristics	4
2.1 Summary of the code HONEYCOMB	4
2.1.1 Configuration of the reactor treated in calculation	4
2.1.2 Summary of input data	5
2.1.3 Flow of calculation and code structure	5
2.2 Preparation of few-group cross sections	7
2.2.1 Library data of group constants	7
2.2.2 Twenty-five-group effective cross sections	8
2.2.3 Weighting spectra for collapsing group constants	9
2.2.4 Few-group cross sections and kinetics parameters	10
2.2.5 Three-group constants for γ -ray production and transport	11
2.3 Two-dimensional triangular diffusion code TRI-2D	12
2.3.1 Subroutine TRI 2D	13
2.3.2 Subroutine TRI 2DA	16
2.3.3 Subroutine TRIPOW	17
2.3.4 Inclusion of TRI-2D into HONEYCOMB system	17
2.3.5 Comparison between calculational results of TRI-2D and HEXA	17
2.4 Three-dimensional criticality calculation	21
2.4.1 Two-dimensional r - z diffusion code RZ	21
2.4.2 Two-dimensional hexagonal diffusion code HEXA	23
2.4.3 Three-dimensional hexagonal- z diffusion code HEXAZ	26
2.4.4 Improvement of accuracy of predicted neutron flux values in and around control rods	28
2.4.5 Criticality adjustment by insertion depth of control rods	34
2.4.6 Three-dimensional distribution of adjoint neutron flux	35
2.5 Three-dimensional power distribution	36
2.5.1 Three-dimensional distribution of heat deposition by neutron-induced γ -ray	36
2.5.2 Total power generation in each of 3-dimensional volume segments	38
2.5.3 Detailed power distribution for each fuel pin	39
2.6 Burn up calculation	46
2.6.1 Burn up calculation in each 3-dimensional volume segment	46
2.6.2 Burn up calculation for each fuel pin	48
2.7 Applicability tests of the code HONEYCOMB	50
2.7.1 A sample problem	50
2.7.2 Examination of mesh size effects	55
3. FDCAL-3, the Detailed Calculation Subsystem Predicting the JOYO Thermo-Hydraulic Characteristics	60
3.1 Summary of the code FDCAL-3: the combination of the codes FDCAL-2 and FATEC-3	60
3.2 Method for calculating the coolant flow distribution in the reactor vessel	61

3.2.1	Analytical model and equations for predicting the coolant flow distribution	61
3.2.2	Numerical method for pressure balance calculation	64
3.3	Method of pressure drop calculation for the assembly.....	66
3.3.1	Analytical model and equations for pressure drop calculation	66
3.3.2	Numerical method of pressure balance calculation in subchannels consisting of pin bundles of nuclear fuel elements	68
3.4	Method of the temperature distribution calculation in coolant and fuel elements in the assembly	69
3.4.1	Analytical model and equations for the temperature calculation.....	69
3.4.2	Numerical method for temperature calculation.....	72
3.5	Examples of calculational results of the code FDCAL-3.....	75
4.	Concluding Remarks	77
	Acknowledgments	77
	References.....	77

目 次

1. 序 論.....	1
2. 「常陽」詳細核特性解析サブシステム HONEYCOMB	4
2.1 HONEYCOMB コードの概要	4
2.1.1 計算対象としての原子炉の形状.....	4
2.1.2 入力データの概要.....	5
2.1.3 計算手順とコードの構成.....	5
2.2 少数群断面積の準備	7
2.2.1 炉定数ライブラリー.....	7
2.2.2 25群実効断面積の計算.....	8
2.2.3 群数縮約用重みスペクトラムの計算.....	9
2.2.4 少数群断面積および動特性パラメータ.....	10
2.2.5 γ 線生成および輸送計算用 3 群定数.....	11
2.3 2次元三角格子用拡散コード TRI-2D	12
2.3.1 サブルーチン TRI2D	13
2.3.2 サブルーチン TRI2DA	16
2.3.3 サブルーチン TRIPOW	17
2.3.4 HONEYCOMB と三角格子計算コード群との連結	17
2.3.5 計算結果の比較検討.....	17
2.4 3次元臨界計算	21
2.4.1 2次元 r - z 格子用拡散コード RZ	21
2.4.2 2次元六角格子用拡散コード HEXA	23
2.4.3 3次元六角- z 格子用拡散コード HEXAZ	26
2.4.4 制御棒内とその近傍の中性子束の精度の改良.....	28
2.4.5 制御棒挿入深度による臨界調整.....	34
2.4.6 3次元随伴中性子束分布.....	35
2.5 3次元熱出力分布	36
2.5.1 二次 γ 線による3次元発熱分布	36
2.5.2 3次元体積要素毎の熱出力.....	38
2.5.3 燃料ピン毎の詳細熱出力.....	39
2.6 燃焼計算	46
2.6.1 3次元体積要素毎の燃焼計算.....	46
2.6.2 燃料ピン毎の燃焼計算.....	48
2.7 HONEYCOMB コードの適用性検討	50
2.7.1 例題.....	50
2.7.2 メッシュ効果の検討.....	55
3. 「常陽」詳細熱水力特性解析サブシステム FDCAL-3	60
3.1 FDCAL-2, FATEC-3 結合コード FDCAL-3 の概要	60
3.2 炉容器内冷却材流量配分計算法	61
3.2.1 流量配分計算モデル.....	61
3.2.2 圧力バランスの数値計算法.....	64
3.3 燃料集合体内における圧力損失計算法	66
3.3.1 圧力損失計算モデル.....	66
3.3.2 燃料要素ピンバンドルから成るサブチャンネル内の圧力バランスの数値計算法.....	68
3.4 燃料集合体内の冷却材および燃料要素中の温度分布計算法	69
3.4.1 温度計算のためのモデルと式.....	69

3.4.2	温度計算用数値計算式.....	72
3.5	FDCAL-3 コードの計算結果例	75
4.	結 言.....	77
	謝 辞.....	77
	文 献.....	77

1. Introduction

The JOYPAC* system is an off-line computation system for supervising and planning performance of the Japan Experimental Fast Reactor, "JOYO". The development work of the system was commenced in 1971 for the purpose of predicting and checking the nuclear and thermo-hydraulic characteristics of the reactor system in coming operation cycle, as well as for the purpose of recording the operational history and statistics.

According to the required functions, the program system consists of four subsystems:

- (1) HONEYCOMB*, the detailed calculation subsystem predicting the nuclear characteristics
- (2) FDCAL* and FATEC*, the detailed calculation subsystem predicting the thermo-hydraulic characteristics
- (3) SMART*, the simple calculation subsystem
- (4) MASTOR*, the recording subsystem

This report (Part 2) is for describing the outline of the detailed calculation subsystems HONEYCOMB and FDCAL-3 (a combination of codes FDCAL-2 and FATEC-3), mainly about their functions and methods of calculations, while SMART and MASTOR subsystems are described in Part 1²⁸⁾, together with the general introduction of the JOYPAC system. A user's manual will be published separately in the future.

HONEYCOMB, described in Chapter 2, is a diffusion criticality and burn up calculation program dealing with the geometry of the core as a 3-dimensional hexagonal- z mesh structure. It produces the fundamental informations about the core under stationary operation, such as detailed power distribution required by both FDCAL-3 and SMART, and 3-dimensional distribution of neutron flux required by SMART. It can predict also the critical insertion depth of control rods, 3-dimensional density distribution of fuel nuclides etc., which will change through the burn up of the core. Power distribution and burn up are also obtained for fuel pins, if necessary, as well as for assemblies. For the 2-dimensional criticality calculation in x - y mid-plane geometry, a triangular mesh diffusion code TRI-2D is also prepared in addition to the hexagonal mesh diffusion code HEXA. The JAERI-Fast set is used for the group constants in this subsystem HONEYCOMB, with some additions from the ABBN set. Neutron spectrum in each material zone is calculated by 25-group r - z diffusion program with a coarse mesh structure, in order to collapse the group constants into a few groups for use in 2-dimensional fine-mesh and 3-dimensional coarse-mesh criticality calculations. Kinetics parameters are also prepared by this 25-group r - z diffusion model. Three-dimensional adjoint neutron fluxes can also be calculated after regular fluxes are obtained. In the calculation of the 3-dimensional power distribution, the effect of the neutron-induced γ -ray in the core is considered. Burn up calculation is made about nine nuclides of ^{235}U , ^{236}U , ^{238}U , ^{239}Pu , ^{240}Pu , ^{241}Pu , ^{242}Pu , LFP (lumped fission products) and ^{10}B .

In the development of the HONEYCOMB code, main effort was devoted to achieve both accuracy of results and efficiency in computation compatible for practical use. Special imple-

* Names of the subsystems have come from the following meanings.

HONEYCOMB: The geometrical shape of hexagonal- z assemblies in the core

FDCAL: Flow Distribution Calculation

FATEC: Fuel Assembly Temperature Evaluation Code

SMART: Simplified Method to Analyze the Reactor Technical performance

MASTOR: Monitoring And Supervising Tool on Operation of Reactor

JOYPAC: JOYO Performance Analysis Code

mentation can be summarized in the following three points :

- (1) The 3-dimensional criticality calculation is applied only to the central radial zones, inside the fictitious boundary set in the middle of radial blanket, so as to save the computation time. This is because the outer zones have very little influence on the reactivity, which had been confirmed previously by design calculations. Hence, in these outer zones, the 3-dimensional distribution of neutron flux is approximated by synthesizing the 2-dimensional flux distributions obtained by r - z and hexagonal calculations.
- (2) Accuracy of the predicted flux values is enhanced in and around control rods without making mesh sizes fine, by preparing separately diffusion coefficients, locally modified by a simple transport model (§ 2.4.4).
- (3) Efficiency in calculating the detailed power distribution for each fuel pin in fuel assembly is raised by using 1-group 2-dimensional diffusion model for each 3-dimensional coarse volume segment and by engaging a method of potential theory (§ 2.5.3).

FDCAL-3, described in Chapter 3, is a combination of the coolant flow distribution calculation code FDCAL-2 and the temperature distribution calculation code FATEC-3.

FDCAL-2 calculates the steady state flow rates in all coolant flow paths between inlet plenum and outlet plenum in the reactor vessel. Flow rate distribution over these flow paths is calculated to achieve an equal pressure drop for all flow paths between inlet and outlet plenums. In this calculation, pressure gradient in each plenum such as high pressure plenum is assumed to be uniform.

A net pressure drop of an assembly, in which fuel elements are arranged hexagonally, is predicted taking account of flow distribution in the assembly, because power distribution is given 3-dimensionally in the assembly. Flow distribution in an assembly is calculated by using triangular subchannel model. Thermal mixing effects in the subchannel, resulting from thermal conduction and turbulent crossflow, are assumed to be expressed in terms of an apparent heat transfer coefficient. Momentum interchanges are, however, neglected between adjacent schannels. Each subchannel is assumed to contain 1-dimensional single phase flow. The equations expressing mass, momentum and energy balances are solved as an initial value problem by using finite difference method, with a given inlet total flow rate into an assembly, inlet coolant temperature as the initial condition and power distribution. The numerical procedures involve an iterative technique keeping pressure drop in each subchannel equal. In other coolant channels not adjoining fuel elements, pressure drop is calculated by using friction loss coefficients determined from experiments, and by taking account of approximate uniform γ -ray heating.

FATEC-3 calculates the temperature distribution of coolant and fuel elements in an assembly. Coolant temperature distribution is calculated by using again subchannel model. There, subchannel flow distribution is given by FDCAL-2 results, or if necessary, FATEC-3 itself can calculate it as well as coolant temperature distribution. The temperature within a fuel element is calculated in the 1-dimensional (r) or 2-dimensional (r - θ) model. FATEC-3 is applied to some assemblies optionally specified in a given core configuration. At the same time, hot-spot temperature can also be estimated as one of the informations in order to make sure the safe operation.

The subsystem FDCAL-3 has been linked to HONEYCOMB as a segment of overlay structure, consequently forming the detailed calculation subsystem in the entire system JOYPAC. The detailed calculation subsystem produces the data file of the detailed fundamental informations about the reactor under stationary performance, this data file being supplied to the SMART/MASTOR combination. SMART predicts changes of the various characteristics in a short term, utilizing the informations stored in the data file. Thus, the time spent by resorting to the de-

tailed but expensive calculation is reduced as far as possible, and supervision of reactor performance is made possible with practically sufficient accuracy and within the practical limit of computation time.

Listed below are the members of the Working Group on Fast Reactor Safety Analysis Codes including those who were once members of the group.

Japan Atomic Energy Research Institute: S. KATSURAGI, chief of the Nuclear Codes Evaluation Sub-Committee
T. SUZUKI, group leader of the Working Group
A. HASEGAWA, M. AKIMOTO, Y. MIYAMOTO, K. SANOKAWA,
K. IKAWA, Y. MURAO

Power Reactor and Nuclear Fuel

Development Corporation:

Tokyo Shibaura Electric Co., Ltd.:

Japan Atomic Power Co., Ltd.:

Mitsubishi Atomic Power Industries Inc:

Tokyo Institute of Technology:

T. INOUE, F. YOSHINO, Y. MIYAWAKI, H. MIZUTA

M. SUZUKI, A. SHIMIZU

S. NAGAYAMA, Y. KUGE

T. IWAKI, M. KITAMURA, Y. SEKI, K. SAKAI

R. TAKAHASHI

2. HONEYCOMB, the Detailed Calculation Subsystem Predicting the JOYO Nuclear Characteristics

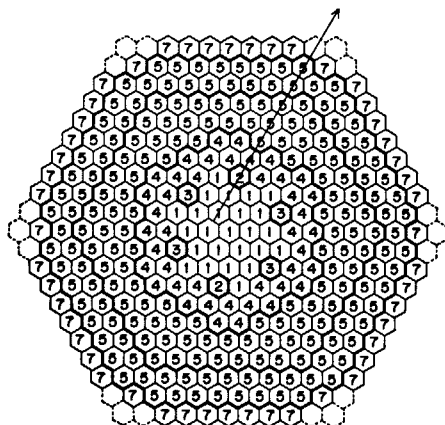
2.1 Summary of the Code HONEYCOMB

In this section, the fundamental concepts or outlines are described in order to make it easy to understand each method given in Sections from §2.2 to §2.7.

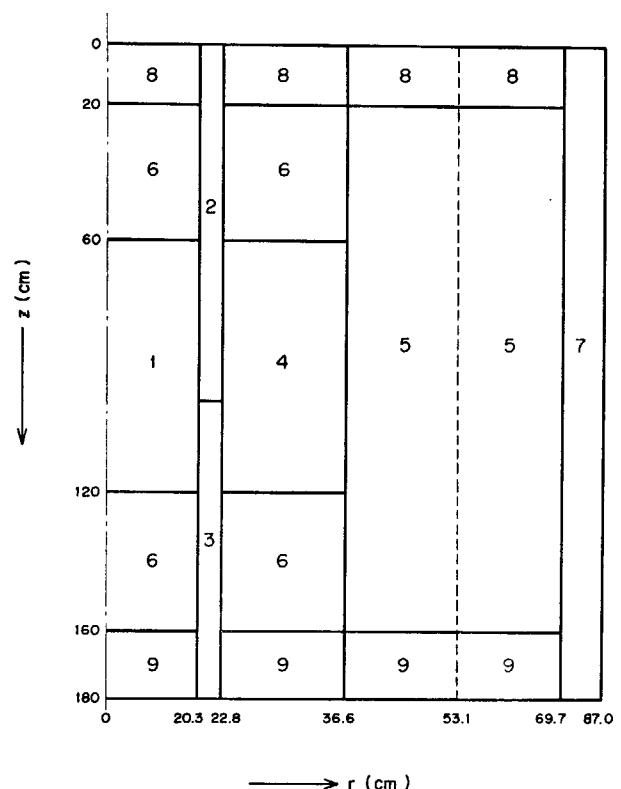
2.1.1 Configuration of the Reactor Treated in Calculation

HONEYCOMB deals mainly with hexagonal assemblies, which are regions of fuel, blanket, control rods and reflector materials arranged in a hexagonal cell. The outer regions of pressure tube and shielding material are not treated in this code with the exception of the subroutine RZ (§2.4.1). Boundary condition for vacuum ($\phi/|\nabla\phi|=0.7104\lambda_{tr}$) is given at the radial outer surfaces of reflectors, at the top of upper sleeve and at the bottom of lower sleeve. Core matrix in the horizontal plane at the middle height is given in Fig. 2.1.1-1. Let the central assembly be the first zone, the six assemblies around it be the second zone and so on, then the core matrix consists of 11 zones.

The 3-dimensional, hexagonal- z , criticality calculation is performed for the region containing up to the 8th zone, whereas the outer 3 zones are dealt with by 2-dimensional r - z and 2-dimensional hexagonal calculation, because these outer zones have very little influence on criticality of the core. Thus the number of assemblies are reduced to about half for the time-consuming 3-



1. fuel (inner) 2. control rod (inserted) 3. control rod (pulled out)
4. fuel (outer) 5. radial blanket 7. reflector
Fig. 2.1.1-1 The core matrix of JOYO (pitch=8.15cm).



6. axial blanket 8. upper sleeve 9. lower sleeve
Fig. 2.1.1-2 Vertical cross section of the reactor simulated for r - z calculation.

dimensional calculation. Figure 2.1.1-2 shows the right half of schema of the reactor in the vertical plane (r - z plane).

2.1.2 Summary of Input Data

The input data for HONEYCOMB are divided into two kinds.

- (1) Data invariable by problems, which are supplied in binary form by means of a magnetic tape or disk.
- (2) Data variable by problems, which are given by cards in decimal or character form.

The kind (1) is the library of reactor constants in 25 energy group structure, consisting of tables of cross sections and resonance self-shielding factors for 20 nuclides (the major part being taken from the JAERI-Fast set¹⁾), fission spectrum, atomic weights etc.

The kind (2) consists of

- (a) Data about components of each material composition.
- (b) Data of reactor configuration.
- (c) Data to control the calculation.

Nuclides and their densities, and temperature for each material are contained in (a). The (b) defines the size of calculational object, mesh structure and arrangement of material zones for each of 25-group r - z (§2.2.3), a few group r - z (§2.4.1), hexagonal (§2.4.2) and hexagonal- z (§2.4.3) calculations, and the detailed hexagonal- z calculation for each fuel pin (§2.5.3 and §2.6.2). In (c), contained are a few group structure, total generation rate of thermal power from the reactor, time intervals for burn up calculation, condition for stopping the burn up calculation, specifications for each optional item of calculation, output print control and so on.

2.1.3 Flow of Calculation and Code Structure

Flow of calculation in the code HONEYCOMB is illustrated in Fig. 2.1.3-1. Since the period of one burn up cycle is usually about 45 days, variation of material densities will be small in the term. Thus, their effects are considered to be negligible on the effective microscopic cross sections and 25-group spectrum in each material zone. In other words, a-few-group microscopic cross sections are assumed to be constant through a burn up cycle. So, the control returns to a-few-group r - z calculation after Δt days' burn up step (see the mark ① in Figs. 2.1.3-1 and 2.1.3-3).

Effective macroscopic cross sections after Δt days' burn up are obtained by the products of these constant microscopic cross sections and effective densities of nuclides, the latter being obtained by averaging the new densities after Δt days' burn up in each volume segment, over each material region shown in Figs. 2.1.1-1 and 2.1.1-2. These new densities in each detailed 3-dimensional mesh region (volume segment) are stored in a disk storage and used as initial values for the burn up calculation at the next time step.

The principal axis of burn up calculation consists of iterations of the next two kinds of calculation.

- (1) Obtaining the neutron flux distribution over space and energy at a fixed time.
- (2) Obtaining the densities of each burnable nuclides after Δt days by the use of the flux values at the beginning of this time interval.

Around this axis, added are various calculations of output data such as the distribution of power generation rate so as to meet requirements from other subsystems. About the details of each procedure, Sections §2.2 through §2.6 describe in the order of the flow of calculation.

HONEYCOMB has been programed in the so-called overlay structure with the following 19 segments (the 18th segment is FDCAL-3).

- (1) Control segment
- (2) Data reading and 25-group effective cross sections
- (3) Effective cross sections for control rod assemblies
- (4) 25-group r - z flux
- (5) 25-group r - z adjoint flux
- (6) Kinetics parameters and few-group effective cross sections
- (7) Few-group r - z flux (with more detailed mesh than in (4))
- (8) Few-group r - z adjoint flux
- (9) 2-dimensional hexagonal or triangular flux
- (10) 2-dimensional hexagonal or triangular adjoint flux
- (11) Correction factor for net current into control rods
- (12) Hexagonal- z flux and criticality adjustment
- (13) Hexagonal- z adjoint flux
- (14) Detailed hexagonal- z flux for each fuel pin within some specified assemblies
- (15) 3-dimensional distribution of heat deposition by γ -ray
- (16) 3-dimensional power distribution
- (17) 3-dimensional detailed power for each fuel pin
- (18) (Subsystem FDCAL-3)
- (19) Data file for SMART and MASTOR

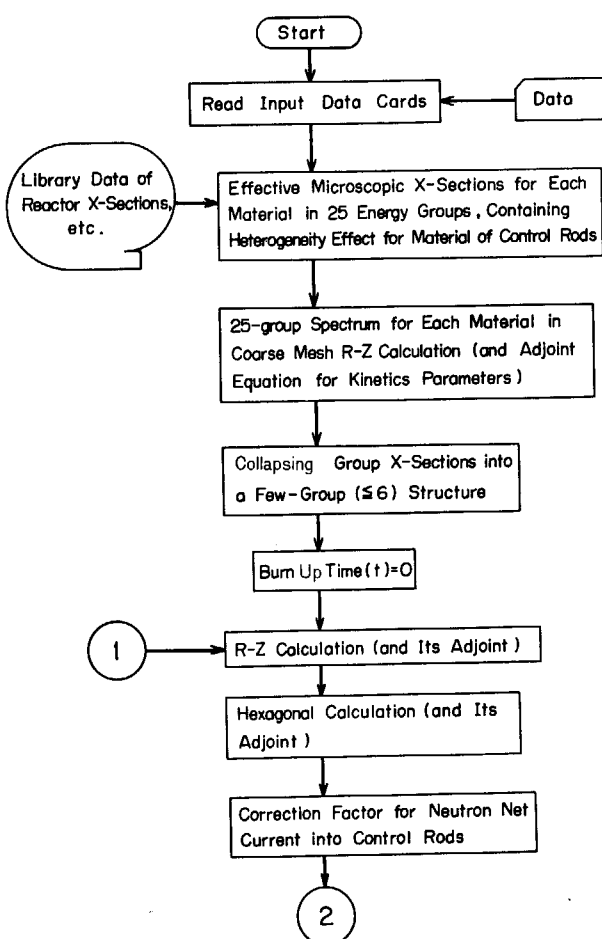


Fig. 2.1.3-1 Flow diagram of HONEYCOMB code.

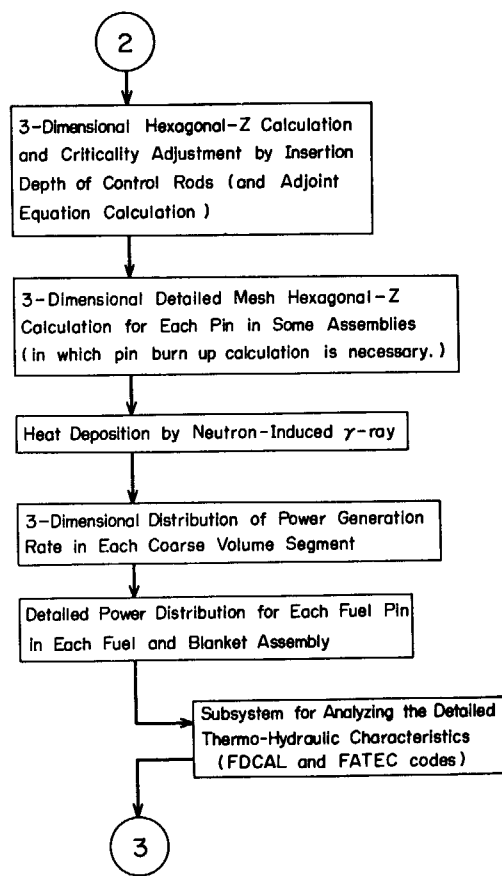


Fig. 2.1.3-2 Flow diagram of HONEYCOMB code (continued).

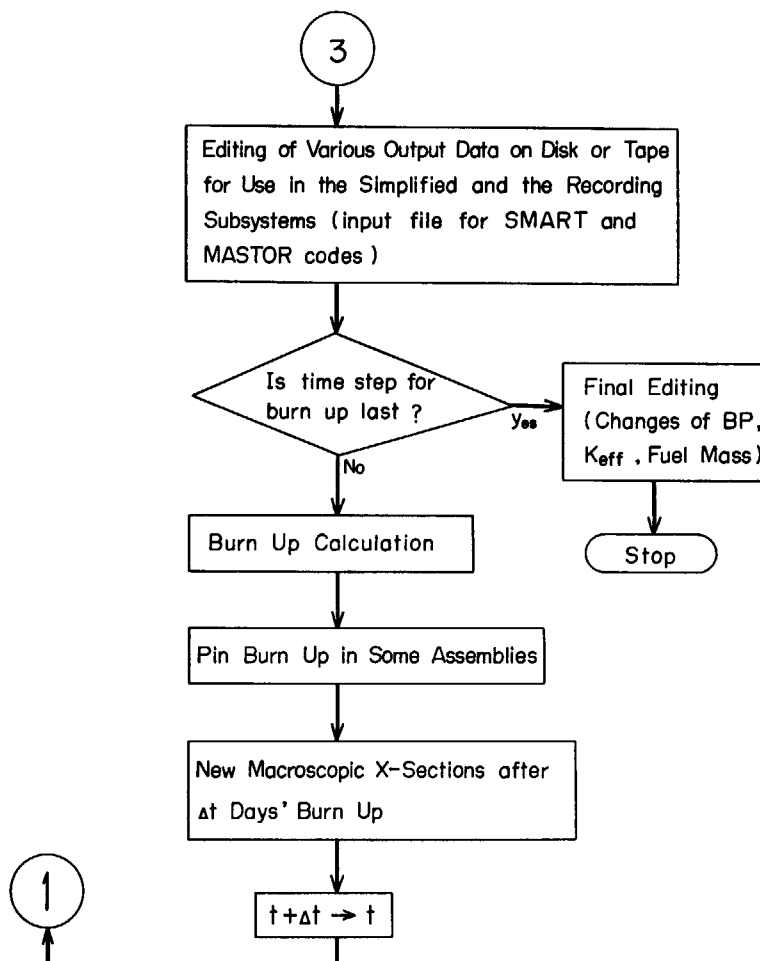


Fig. 2.1.3-3 Flow diagram of HONEYCOMB code (continued).

- (20) 3-dimensional burn up, 3-dimensional pin burn up within some specified assemblies, macroscopic cross sections used in the next time step (control transfers to (7)) and the final editing of burn up history (only at the last step).

On IBM-360/K195 computer, HONEYCOMB uses about 500K bites of core memory and 10 auxiliary memories (disks) for storing input/output data and intermediate results.

2.2 Preparation of Few-group Cross Sections

2.2.1 Library Data of Group Constants

There are such many input data invariable with each problem of the criticality calculation, such as fission spectra, lethargy widths, atomic weights of nuclides, infinite dilution cross sections for various reactions of neutrons with nuclei, group transference matrix for elastic or inelastic scattering, and resonance self-shielding factors. It is convenient that these data are automatically supplied through a library tape/disk in binary form. The code LTFR-4²⁾ was used to make the library tape from 25-group JAERI-Fast and ABBN³⁾ constants data punched on cards. Twenty nuclides were selected for use in fast reactor analysis, and reactor constants of these nuclides have been stored in the library for the HONEYCOMB code (TABLE 2.2.1-1).

This library would be easily updated if some new constants for any nuclides are given by cards in the format of JAERI-Fast or ABBN type.

TABLE 2.2.1-1 Nuclides stored in the cross-section library tape for HONEYCOMB code

Order of nuclides in the tape	Nuclide ID No. (Code number)	Nuclide	Data source
1	925	²³⁵ U	JFS*
2	949	²³⁹ Pu	JFS
3	940	²⁴⁰ Pu	JFS
4	926	²³⁸ U	ABBN ³⁾
5	928	²³⁹ U	JFS
6	942	²⁴² Pu	ABBN
7	40	Zr	ABBN
8	42	Mo	JFS
9	999	LFP(²³⁹ Pu)	ABBN
10	11	Na	JFS
11	24	Cr	JFS
12	26	Fe	JFS
13	28	Ni	JFS
14	8	O	JFS
15	4	Be	ABBN
16	6	C	JFS
17	105	¹⁰ B	JFS
18	115	¹¹ B	JFS
19	1	H	ABBN
20	941	²⁴¹ Pu	JFS

* JAERI-Fast Set¹⁾

2.2.2 Twenty-five-group Effective Cross Sections

Microscopic cross sections are obtained for each energy group and for each mixture in the same way as in the code EXPANDA-4²⁾. Densities of nuclides and temperature (°K) are given by card input. First, the table of self-shielding factors, $f_x^{mi}(R, \sigma_0, T)$, are inter- or extra-polated to the value $R_k^m, \sigma_{0,k}^{mi}, T_k$. There m, i, x and k mean nuclides, group, reaction and mixture, respectively. The R_k^m is defined for only three nuclides (²³⁵U, ²³⁹Pu and ²⁴⁰Pu) by

$$R_k^m = N^{238}/N^m,$$

and $\sigma_{0,k}^{mi}$ is defined for these three nuclides by

$$\sigma_{0,k}^{mi} = \sum_{n \neq m, 238} N_k^n \sigma_t^{ni}. \quad (2.2.2-1)$$

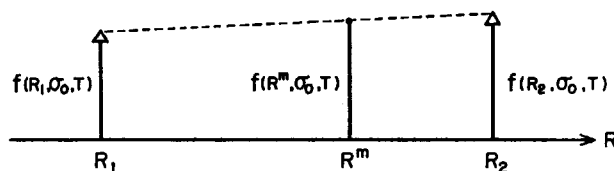
For other nuclides, R is not defined and

$$\sigma_{0,k}^{mi} = \sum_{n \neq m} N_k^n \sigma_t^{ni}. \quad (2.2.2-2)$$

The tables of self-shielding factors (f -table) are given for two values of R which are shown in TABLE 2.2.2-1, and for up to six values of σ_0 ((0, 10, 10², 10³, 10⁴, 10⁵) or (0, 1, 10, 10², 10³, 10⁴)), and for three values of temperature T (300, 900, 2100). First, interpolation about the parameter R is performed linearly as illustrated in Fig. 2.2.2-1, for each tabulated value of σ_0 and T . Then, f -tables are unified in the form $f(\sigma_0, T)$. After that, procedure goes completely same as described in Ref. 2) or 4), that is, the iteration technique is used in the interpolation about σ_0

TABLE 2.2.2-1 Values of R_1 and R_2 for ²³⁵U, ²³⁹Pu and ²⁴⁰Pu and for each value of σ_0 used in tabulation of the self-shielding factors

Element	R σ_0	R_1				R_2			
		10	10 ²	10 ³	10 ⁴	10	10 ²	10 ³	10 ⁴
²³⁵ U	0.2	1	20			0.6	5	50	
²³⁹ Pu	1	5	50			2	10	100	
²⁴⁰ Pu		5	20	200			15	50	500

Fig. 2.2.2-1 Interpolation of f -table values about R .

for determination of $\bar{f}_{t,k}^{mi}$, $\bar{f}_{c,k}^{mi}$, $\bar{f}_{e,k}^{mi}$ and $\bar{\sigma}_{t,k}^{mi}$. Then, $\bar{f}_{t,k}^{mi}$ and $\bar{f}_{r,k}^{mi}$ are obtained without iteration. In the above, f, c, e, t and r mean the kinds of reactions, that is, fission, capture, elastic scattering, total and elastic removal, respectively.

Effective microscopic cross sections are now given by

$$\begin{aligned}\bar{\sigma}_{t,k}^{mi} &= \bar{f}_{c,k}^{mi} \sigma_c^{mi} + \bar{f}_{t,k}^{mi} \sigma_t^{mi} + \bar{f}_{e,k}^{mi} \sigma_e^{mi} + \sigma_{in}^{mi}, \\ \bar{\sigma}_{D,k}^{mi} &= \{\bar{f}_{t,k}^{mi} \sigma_t^{mi} - (\bar{\sigma}_{t,k}^{mi} - \bar{f}_{c,k}^{mi} \sigma_c^{mi})\} (1 - \mu_e^{mi}) + (\bar{\sigma}_{t,k}^{mi} - \bar{f}_{c,k}^{mi} \sigma_c^{mi}), \\ \bar{\sigma}_{f,k}^{mi} &= \bar{f}_{f,k}^{mi} \sigma_f^{mi}, \\ \bar{\sigma}_{c,k}^{mi} &= \bar{f}_{c,k}^{mi} \sigma_c^{mi}, \\ \bar{\sigma}_{a,k}^{mi} &= \bar{\sigma}_{t,k}^{mi} + \bar{\sigma}_{c,k}^{mi}, \\ (\nu \bar{\sigma}_f)_k^{mi} &= \nu^{mi} \bar{\sigma}_{f,k}^{mi}, \\ \bar{\sigma}_{T,k}^{mi} &= \bar{\sigma}_{a,k}^{mi} + \bar{f}_{r,k}^{mi} \sigma_r^{mi} + \sigma_{in}^{mi} - \sigma_{in}^{m,i \rightarrow i}, \\ \bar{\sigma}_{s,k}^{mi} &= \bar{f}_{e,k}^{mi} \sigma_e^{mi} + \sigma_{in}^{mi}, \\ \bar{\sigma}_{s,k}^{m,i \rightarrow i+j} &= \sigma_{eH}^{i \rightarrow i+j}, \quad m=H, \quad j=0, 1, \dots, 11, \\ \bar{\sigma}_{s,k}^{m,i \rightarrow i} &= \bar{f}_{e,k}^{mi} \sigma_e^{mi} - \bar{f}_{r,k}^{mi} \sigma_r^{mi} + \sigma_{in}^{m,i \rightarrow i}, \\ \bar{\sigma}_{s,k}^{m,i \rightarrow i+1} &= \bar{f}_{r,k}^{mi} \sigma_r^{mi} + \sigma_{in}^{m,i \rightarrow i+1}, \\ \bar{\sigma}_{s,k}^{m,i \rightarrow i+j} &= \sigma_{in}^{m,i \rightarrow i+j}, \quad j=2, 3, \dots, 11, \\ \bar{\sigma}_{s,k}^{m,i \rightarrow i+j} &= 0, \quad i+j > 25.\end{aligned}$$

Macroscopic cross sections D_k^i , $\Sigma_{a,k}^i$, $\Sigma_{s,k}^i$, $\Sigma_{T,k}^i$, $(\nu \Sigma_f)_k^i$ and $\Sigma_{s,k}^{i \rightarrow i+j}$ are obtained using above microscopic cross sections and effective densities of individual nuclides in the mixture $k(N_k^m)$.

We obtained these cross sections in homogeneous model. In fact, heterogeneity effect due to the hexagonal arrangement of fuel pins can be neglected as having been confirmed by Suzuki and Katsuragi^(5),6) for JOYO fuel and blanket assemblies. In control rod assemblies, however, heterogeneity effect can not be neglected because only seven rods of B_4C are arranged in each of them, rather in the neighbourhood of the center of the hexagonal region. Thus, collision probability method is applied to estimate the effective macroscopic cross sections for these control rod assemblies.

2.2.3 Weighting Spectra for Collapsing Group Constants

For obtaining the 25-group spectrum for each mixture, 25-group diffusion equations are solved with a fairly coarse mesh structure for a 2-dimensional r - z geometry simulating the reactor (Fig. 2.1.1-2). Numerical method is almost the same as in §2.4.1, where a few-group model with fine mesh structure is used. From the resulting flux, obtained is the 25-group weighting spectrum for each mixture region V_k as

$$\Phi_k^i = \int_{V_k} \phi^i(r, z) dV,$$

for use in collapsing the 25-group cross sections into a few group (≤ 6) structure.

Adjoint flux distribution $\phi^{*i}(r, z)$ is also obtained if kinetics parameters are necessary to be evaluated.

2.2.4 Few-group Cross Sections and Kinetics Parameters

From the 25-group cross sections and spectrum for each mixture k , few-group cross sections can now be calculated. In the following equations, the indices i and j are for fine groups, and n and l for coarse groups. With the notation $i \in n$, for instance, we mean that i -th groups are collapsed into one coarse group that becomes the n -th group in the few-group structure.

$$\begin{aligned}\chi^n &= \sum_{i \in n} \chi^i, \\ \Phi_k^n &= \sum_{i \in n} \Phi_k^i, \\ D_k^n &= \sum_{i \in n} D_k^i \Phi_k^i / \Phi_k^n, \\ \Sigma_{a,k}^n &= \sum_{i \in n} \Sigma_{a,k}^i \Phi_k^i / \Phi_k^n, \\ \Sigma_{s,k}^n &= \sum_{i \in n} \Sigma_{s,k}^i \Phi_k^i / \Phi_k^n, \\ (\nu \Sigma_f)_k^n &= \sum_{i \in n} (\nu \Sigma_f)_k^i \Phi_k^i / \Phi_k^n, \\ \Sigma_{s,k}^{n \rightarrow l} &= \sum_{i \in n} \left(\sum_{j \in l} \Sigma_{s,k}^{i \rightarrow j} \right) \Phi_k^i / \Phi_k^n,\end{aligned}$$

where $l = n, n+1, \dots, \text{NMAX}$ and NMAX is the total number of coarse groups ($\text{NMAX} \leq 6$), and

$$\Sigma_{T,n}^k = \Sigma_{a,k}^n + \Sigma_{s,k}^n - \Sigma_{s,k}^{n \rightarrow n}.$$

For burn up calculation, $\sigma_{f,k}^{mn}$, $\sigma_{c,k}^{mn}$ and $\sigma_{a,k}^{mn}$ are also obtained. In addition, the γ -ray production constants

$$S_k^{i \rightarrow g} = \sum_m \sum_x S_x^{m, i \rightarrow g} \bar{\sigma}_{x,k}^{mi} N_k^m$$

(where the product $S_x^{m, i \rightarrow g} \bar{\sigma}_{x,k}^{mi}$ is given in §2.2.5) are collapsed to $S_k^{n \rightarrow g}$.

When the kinetics parameters are needed, they are directly obtained from 25-group cross sections, and regular and adjoint flux distributions. In what follows, m denotes six fissionable nuclides (^{235}U , ^{238}U , ^{239}Pu , ^{240}Pu , ^{241}Pu and ^{242}Pu) and l means the six families of precursors. Delayed neutron fraction for material m is $\beta^m = \sum_l \beta_l^m$. Then, we have

$$\begin{aligned}\beta_{\text{eff},l} &= \frac{\sum_m \beta_l^m \int_V [\sum_i (\nu \Sigma_f)_i^{mi} \phi^i] [\sum_i \chi_d^{mi} \phi^{*i}] dV}{\sum_m \int_V [\sum_i (\nu \Sigma_f)_i^{mi} \phi^i] [\beta^m \sum_i \chi_d^{mi} \phi^{*i} + (1 - \beta^m) \sum_i \chi_p^{mi} \phi^{*i}] dV}, \\ \beta_{\text{eff}}^m &= \frac{\beta^m \int_V [\sum_i (\nu \Sigma_f)_i^{mi} \phi^i] [\sum_i \chi_d^{mi} \phi^{*i}] dV}{\sum_m \int_V [\sum_i (\nu \Sigma_f)_i^{mi} \phi^i] [\beta^m \sum_i \chi_d^{mi} \phi^{*i} + (1 - \beta^m) \sum_i \chi_p^{mi} \phi^{*i}] dV}, \\ \beta_{\text{eff}} &= \sum_l \beta_{\text{eff},l} = \sum_m \beta_{\text{eff}}^m \text{ (effective delayed neutron fraction)}, \\ l_p &= \frac{\int_V \sum_i (\phi^i \phi^{*i} / \bar{v}^i) dV}{\sum_m \int_V [\sum_i (\nu \Sigma_f)_i^{mi} \phi^i] [\sum_i \chi_p^{mi} \phi^{*i}] dV} \text{ (prompt neutron life time)}, \\ F^m &= \frac{\int_V \sum_i \Sigma_f^{mi} \phi^i dV}{\sum_m \int_V \sum_i \Sigma_f^{mi} \phi^i dV}, \\ W_d^m &= \frac{\int_V [\sum_i (\nu \Sigma_f)_i^{mi} \phi^i] [\sum_i \chi_d^{mi} \phi^{*i}] dV}{\int_V \sum_i (\nu \Sigma_f)_i^{mi} \phi^i dV},\end{aligned}$$

$$W_p^m = \frac{\int_V [\sum_i (\nu \Sigma_i)^m \phi^i] [\sum_i \chi_p^i \phi^{*i}] dV}{\int_V \sum_i (\nu \Sigma_i)^m \phi^i dV}$$

2.2.5 Three-group Constants for γ -ray Production and Transport

For the class of fast experimental reactors, for example "JOYO", it is recognized that the heat produced by γ -ray is about 10% of the total heat generated in the reactor and its contribution in the blanket exceeds 30% of the total heat generated in that region⁷⁾. Therefore, in this HONEYCOMB system more detailed and more accurate heat production calculation is requested in order to estimate detailed coolant flow distribution. As the neutron flux distribution is calculated in 3-dimensional geometry, it is desirable to calculate the γ -ray flux in the same geometrical condition for consistency with the neutronic calculation. In this occasion, however, the computer core memory and computer running time force us to employ a few-group γ -ray flux calculation inevitably. In the γ -ray flux calculation, the results depend on the accuracy of the γ -ray source intensity. Therefore, first of all, we concentrated our attempt on the preparation of secondary γ -ray production constants and the related code preparation.

The available data files for the photon production cross section are POPOP4⁸⁾ and ENDF/B⁹⁾ data library. In the ENDF/B-III file, there are only a few nuclides that have the γ -ray production data and these nuclides are not important for fast reactor design. Therefore, POPOP4 has been mainly used for the shielding calculation. Recently distributed ENDF/B-IV contains photon production cross section data for almost all of the important nuclides for FBR. It is expected

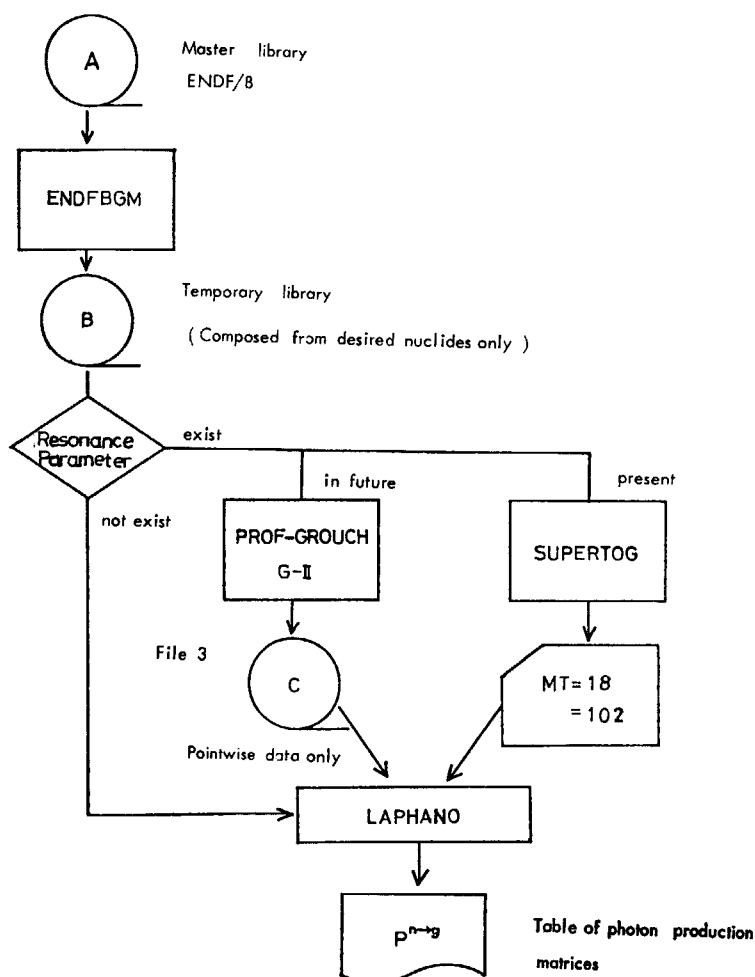


Fig. 2.2.5-1 Process flow for photon production matrices calculation.

TABLE 2.2.5-1 Neutron and photon energy group structure

Photon energy group structure

Group	Upper energy	Lower energy	DELU*
1	10.0 MeV	3.0 MeV	1.204
2	3.0 MeV	500 KeV	1.790
3	500 keV	10 KeV	3.912

Neutron energy group structure

GROUP	UP-ENERGY	LOW-ENERGY	DELU*
1	1.0500 E 07	6.5000 E 06	0.4796
2	6.5000 E 06	4.0000 E 06	0.4855
3	4.0000 E 06	2.5000 E 06	0.4700
4	2.5000 E 06	1.4000 E 06	0.5798
5	1.4000 E 06	8.0000 E 05	0.5596
6	8.0000 E 05	4.0000 E 05	0.6931
7	4.0000 E 05	2.0000 E 05	0.6931
8	2.0000 E 05	1.0000 E 05	0.6931
9	1.0000 E 05	4.6500 E 04	0.7657
10	4.6500 E 04	2.1500 E 04	0.7714
11	2.1500 E 04	1.0000 E 04	0.7655
12	1.0000 E 04	4.6500 E 03	0.7657
13	4.6500 E 03	2.1500 E 03	0.7714
14	2.1500 E 03	1.0000 E 03	0.7655
15	1.0000 E 03	4.6500 E 02	0.7657
16	4.6500 E 02	2.1500 E 02	0.7714
17	2.1500 E 02	1.0000 E 02	0.7655
18	1.0000 E 02	4.6500 E 01	0.7657
19	4.6500 E 01	2.1500 E 01	0.7714
20	2.1500 E 01	1.0000 E 01	0.7655
21	1.0000 E 01	4.6500 E 00	0.7657
22	4.6500 E 00	2.1500 E 00	0.7714
23	2.1500 E 00	1.0000 E 00	0.7655
24	1.0000 E 00	4.6500 E -01	0.7657
25	4.6500 E -01	2.1500 E -01	0.7714

* lethargy width

TABLE 2.2.5-2 An example of photon production matrix for ^{238}U

PHOTON PRODUCTION MATRIX			
NUCLIDE = U-238 MAT= 1262			
NEUTRON GROUP	GAMMA GROUP		
	1	2	3
1	5.14330E-01	6.00135E+00	4.15686E+00
2	4.16598E-01	6.35625E+00	2.31081E+00
3	1.40276E-01	4.58160E+00	3.62481E+00
4	1.17361E-01	2.88253E+00	5.11716E+00
5	8.15715E-02	8.48005E-01	4.09877E+00
6	6.67120E-02	4.28066E-01	2.32699E+00
7	3.18166E-02	2.78788E-01	1.65454E+00
8	4.21918E-02	3.69674E-01	1.22655E+00
9	6.66785E-02	5.84225E-01	7.14660E-01
10	1.12921E-01	9.89470E-01	1.78750E-01
11	1.90646E-01	1.67057E+00	2.99885E-01
12	2.46112E-01	2.17392E+00	3.90054E-01
13	3.40032E-01	2.97928E+00	5.34530E-01
14	4.85771E-01	4.25632E+00	7.63750E-01
15	8.94955E-01	7.84170E+00	1.40720E+00
16	1.23190E+00	1.07936E+01	1.93655E+00
17	5.52945E+00	4.84476E+01	8.69230E+00
18	4.60592E+00	4.03560E+01	7.24055E+00
19	1.61004E+01	1.41068E+02	2.53099E+01
20	2.13731E+01	1.87265E+02	3.35985E+01
21	4.60347E+01	4.03345E+02	7.23670E+01
22	2.00314E+01	1.75510E+00	3.14893E-01
23	1.40831E-01	1.23393E+00	2.21387E-01
24	1.49128E-01	1.30667E+00	2.34430E-01
25	2.03165E-01	1.78008E+00	3.19376E-01

that the photon production cross section data in ENDF/B file will be supplemented further, and it is desirable to have γ -ray production constants consistent with neutron data. From the reasons stated above, we decided to produce the few-group γ -ray production group constants from ENDF/B-IV file.

For the processing we used the code system coupling the following two codes; PROF-GROUCH-G-II¹⁰⁾: a system of fully automated multigroup cross section set production routine, and LAPHANO¹¹⁾: a P_0 multigroup photon production matrix and source code for ENDF. The process flow is shown in Fig. 2.2.5-1.

For γ -ray energy groups, a fairly coarse group structure was chosen, i.e. 3 groups. The group structure is given in TABLE 2.2.5-1. For neutrons, we adopted JAERI-Fast 25 group structure¹⁾, and hence the produced photon production matrix was 25 (neutron energy group) \times 3 (photon energy group) matrix. We processed the photon production matrix for the 11 nuclides, ^{235}U , ^{238}U , ^{239}Pu , ^{10}B , Na, Al, Fe, Cr, Ni, C and O. These nuclides cover almost all the important nuclides for the typical fast reactor composition. We used ENDF/B-IV only for processing the matrices. For further details of the process method and numerical calculation, the manual of the code LAPHANO¹¹⁾ and the specification manual of the ENDF/B γ -ray file⁹⁾ should be consulted. In this processing by the code LAPHANO, the original code gave many troubles in logics, and hence we had to correct and to modify it in use.

As an example, produced secondary γ -ray production matrices for ^{238}U nuclide is shown in TABLE 2.2.5-2. In this table, the photon production cross sections are given in the units of barns-photons ($10^{-24}\text{cm}^2\text{-photons}$). In this example, you may read as 2.88253 b -photons for photon production cross section from neutron energy group 4 to photon energy group 2.

Other γ -ray transport group constants are prepared using GAMLEGJ¹²⁾ code.

2.3 Two-dimensional Triangular Diffusion Code TRI-2D

In the earliest stage of developing this HONEYCOMB system for 2-dimensional diffusion calculation, a uniform hexagonal mesh configuration code was intended to be programed for simulating a real core configuration. In this geometry, however, fairly large mesh spacing is taken. The calculational accuracy is, therefore, feared poor to some extent. By the reason stated

above, we have decided to develop a 2-dimensional diffusion code in uniform triangular mesh geometry, which allows more fine mesh spacing than hexagonal mesh.

In this section, a 2-dimensional calculation routine in uniform triangular mesh configuration will be described together with the calculation methods and their results.

2.3.1 Subroutine TRI2D: A 2-dimensional Diffusion Calculation Code in Uniform Triangular Mesh Configuration

Described in this section are the procedure to obtain a finite difference equation of neutron balance over discrete element of volume.

Any triangular element in the hexagonal lattice is denoted by "S" and its adjacent elements are denoted by "L", "R" and "T", where L, R and T mean "Left", "Right" and "Top" position of the specified element S, respectively. A schematic layout of the mesh configuration is given in Fig. 2.3.1-1. The mesh (nodal) point is defined in the center of gravity in each triangle, so the finite difference element S has the uniform nuclear properties.

A basic equation in the diffusion approximation is written as

$$DV^2\phi - \Sigma_T\phi + \hat{S} = 0. \quad (2.3.1-1)$$

Integrating Eq. (2.3.1-1) over a finite difference volume element S, we get

$$\int_{S_i} D^i \nabla^2 \phi^i dS - \int_{V_i} \Sigma_T^i \phi^i dV + \int_{V_i} \hat{S}^i dV = 0, \quad (2.3.1-2)$$

where

D = diffusion constant,

Σ_T = macroscopic total cross section,

\hat{S} = source,

ϕ = real flux,

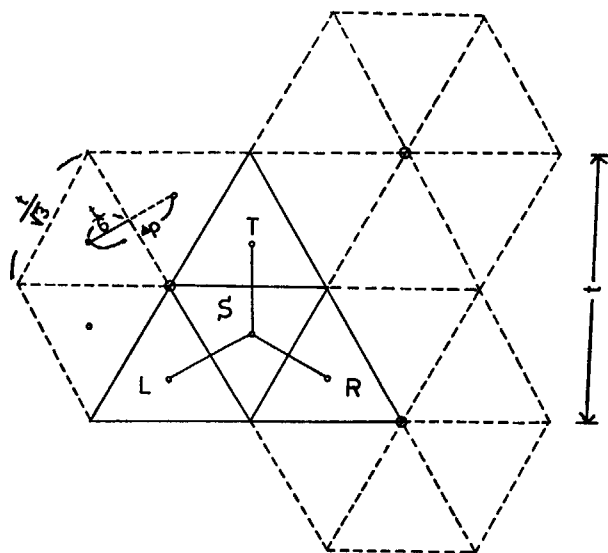
S_i = surface area of element S,

V_i = volume of element S,

suffix i refers energy group.

We define effective diffusion constant along the direction of adjacent mesh point as follows:

$$\bar{D}_m^i = \frac{\left(\frac{4p}{2} + \frac{4p}{2}\right)}{\left(\frac{4p}{2} \frac{1}{D_m^i} + \frac{4p}{2} \frac{1}{D_s^i}\right)} = \frac{2}{D_m^{-1} + D_s^{-1}}, \quad (2.3.1-3)$$



t: Pitch in hexagonal lattice

Fig. 2.3.1-1 Schematic layout of the mesh configuration for TRI-2D code.

$m=L, R \text{ or } T$ (adjacent element index),

where $\Delta p=t/3$ stands for the distance between adjacent mesh points in triangular mesh configuration and t is the pitch of the hexagonal mesh configuration.

Approximating $\nabla\phi$ term in the following way,

$$\nabla\phi_m = \frac{\phi_m - \phi_s}{\Delta p} = \frac{\phi_m - \phi_s}{\frac{t}{3}}, \quad (2.3.1-4)$$

$m=L, R \text{ or } T$

leakage in the z direction is written as

$$L_z^i = \int D_s^i(B_{z,s}^2) \phi_s^i dV, \quad (2.3.1-5)$$

where $(B_{z,s}^2)$ was taken from the value of the preceding 2-dimensional r - z calculation and \hat{S}^i is the sum of slowing down source and fission source:

$$\hat{S}^i = \lambda \left[\sum_j (\nu^j \Sigma_{f,s}^j) \phi_s^j \right] \chi^i + \sum_{j=1}^N \phi^j \Sigma_{s,s}^{j \rightarrow i}, \quad (2.3.1-6)$$

in which

λ =eigenvalue,

$\nu \Sigma_f$ =macroscopic fission source,

χ =fission spectrum,

$\Sigma^{i \rightarrow j}$ =macroscopic transfer cross section.

Equation (2.3.1-3) will be rewritten in the following form:

$$\begin{aligned} & \frac{2}{(D_L^{-1} + D_s^{-1})} (\phi_L - \phi_s) \sqrt{3} h + \frac{2}{(D_R^{-1} + D_s^{-1})} (\phi_R - \phi_s) \sqrt{3} h \\ & + \frac{2}{(D_T^{-1} + D_s^{-1})} (\phi_T - \phi_s) \sqrt{3} h - D_s(B_{z,s}^2) \frac{t^2}{4\sqrt{3}} h \phi_s \\ & - \Sigma_{T,s} \phi_s \frac{t^2}{4\sqrt{3}} h + \lambda \left(\sum_j (\nu^j \Sigma_{f,s}^j) \phi_s^j \right) \chi^i \frac{t^2}{4\sqrt{3}} h \\ & + \left(\sum_{j=1}^N \phi^j \Sigma_{s,s}^{j \rightarrow i} \right) \frac{t^2}{4\sqrt{3}} h = 0, \end{aligned} \quad (2.3.1-7)$$

where h is thickness of the element S .

Now, we obtain the final equation for the flux in the finite difference element S .

$$\phi_s^n = (F_L^n + F_R^n + F_T^n + L_s^n)^{-1} (F_L^n \phi_L^n + F_R^n \phi_R^n + F_T^n \phi_T^n + Q_s^n + R_s^n), \quad (2.3.1-8)$$

where

$$F_m^n = \frac{\bar{D}_m^n A_r}{\Delta p} = \sqrt{3} \bar{D}_m^n = \left(\frac{2}{D_m^{-1} + D_s^{-1}} \right) \sqrt{3} h,$$

$A_r = \int_{S_1} n dS$ = surface area perpendicular to the adjacent direction,

$$L_s^n = \{ \Sigma_{T,s}^n + D_s^n(B_{z,s}^2)^n \} V_s,$$

$$Q_s^n = \chi^n \lambda \sum_{j=1}^N (\nu^j \Sigma_{f,s}^j \phi_s^j) V_s,$$

$$R_s^n = \sum_{n' > i} \Sigma_{s,s}^{i \rightarrow n'} \phi_s^{n'} V_s,$$

$$V_s = \frac{t^2}{4\sqrt{3}} h.$$

In this code, we use conventional successive over-relaxation (S.O.R.) method to solve the system of equations given above.

In Eq. (2.3.1-8), on the reactor boundary, \bar{F}_m ($m=L, R \text{ or } T$) is not defined, because \bar{D}_m is not given there. Following paragraphs will be devoted to the description of the treatment of the boundary condition.

We use vacuum boundary condition. Flux profiles around the physical boundary is illustrated in Fig. 2.3.1-2. The flux at the physical boundary is denoted by ϕ_0 and, from the vacuum

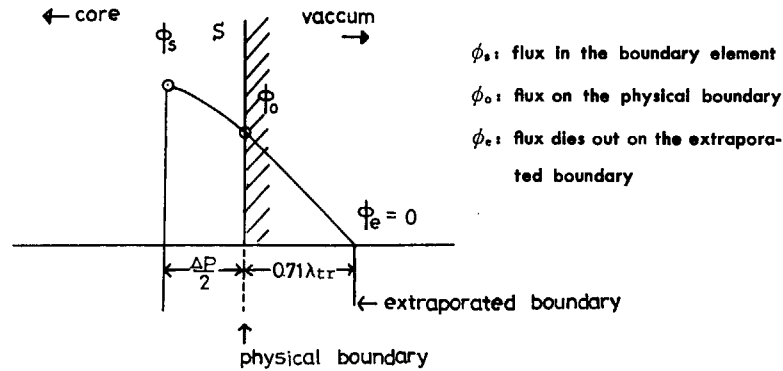


Fig. 2.3.1-2 Flux profiles around the physical boundary.

boundary condition, on the extrapolated boundary extended from the physical boundary by $0.71\lambda_{tr}$, the flux ϕ_e should die out.

For the leakage from the physical boundary, we write

$$\int D \nabla \phi n dS \doteq D \phi_0' \Delta S,$$

where $\Delta S = \int_{S_{\perp}} n dS,$

$$\phi_0' \doteq \frac{-\phi_0}{0.71\lambda_{tr}} = \frac{-\phi_0}{2.1313D_s},$$

$$\lambda_{tr} = \frac{1}{\Sigma_{tr}} = 3D_s,$$

D_s = diffusion constant in element S ,

$$\phi_0 \doteq \phi_s + \phi_0' \frac{\Delta p}{2} = \phi_s - \frac{\phi_0}{2.1313D_s} \frac{\Delta p}{2},$$

$$\phi_0 = \left(1 + \frac{\Delta p}{2 \times 2.1313D_s}\right)^{-1} \phi_s,$$

$$\int D \nabla \phi n dS = D_s \phi_0' \Delta S = D_s \frac{(-\phi_0)}{2.1313D_s} \Delta S = \frac{1}{\sqrt{3}} \frac{(-1)}{\left(\frac{2.1313}{t} + \frac{1}{2 \times 3D_s}\right)} \phi_s h.$$

Therefore we use the following F_{Lb}^n , F_{Rb}^n and F_{Tb}^n instead of F_L^n , F_R^n and F_T^n in Eq. (2.3.1-8) on the boundary elements.

$$*F_{l,b}^n = \frac{1}{\sqrt{3}} \frac{1}{\left(\frac{2.1313}{t} + \frac{1}{2 \times 3D_s}\right)} h,$$

$$F_{l,b}^n = \frac{\sqrt{3}}{2} *F_{l,b}^n, \quad (2.3.1-9)$$

where l takes L, R or T.

The last expression of Eq. (2.3.1-9) represents the edge correction. Because the edge of the reactor boundary is not always perpendicular from the overall point of view for the reactor, the boundary leakage value is corrected by a factor of $\cos(\pi/6)$.

The expressions defined by Eq. (2.3.1-9) are adopted only in the first factor on the right hand side of Eq. (2.3.1-8). It should be noted that $F_{l,b}^n \phi_l = 0$ ($l = L, R$ or T) by the definition.

In the S.O.R. method, the iteration is made in the order of energy groups and triangular element. The convergence criteria are as follows:

a. Eigenvalue convergence;

$$\left| \frac{\lambda_{j-1}}{\lambda_j} - 1 \right| \leq \varepsilon_\lambda = 10^{-5},$$

where

$$\lambda_J = \frac{\text{LOSS} + \text{LEAK}}{\text{PRODUCTION}}$$

$$= \frac{\sum_i \left(\int_{\text{Reactor}} L_{s,i} dV - \sum_{j \neq i} \int_{\text{Reactor}} \Sigma_{s,s}^{i \rightarrow j} \phi_s^j dV \right) + \sum_i \int_{\text{Reactor Surface}} F_{L,b}^i \phi_s^i n dS}{\sum_j \int_{\text{Reactor}} \chi^j \sum_i (\nu \Sigma_{f,i}^i) \phi_s^i dV}$$

$$k_{\text{eff}} = \frac{1}{\lambda_J}$$

J = iteration index.

b. Flux convergence;

$$\left| \frac{\phi_J}{\phi_{J-1}} - 1.0 \right| \leq \epsilon_\phi = 10^{-3}.$$

c. Residue;

$$\text{Residue} = \frac{\sqrt{\sum_{n,s} \{ |\phi_s^n (F_L^n + F_R^n + F_T^n + L_s^n) - (F_L^n \phi_L^n + F_R^n \phi_R^n + F_T^n \phi_T^n + Q_s^n + R_s^n) | \}^2}}{\lambda \sum_{n,s} (\nu \Sigma_{f,i}^i) \phi_s^n}$$

$$\leq \epsilon_R = 10^{-4}.$$

Convergence check prints are made at each ten iterations. When a negative flux appeared or iteration exceeded prefixed maximum iteration number (=300), the calculation is stopped. If convergence criteria are fulfilled, the following outputs are given:

- (i) Neutron balance table,
- (ii) Composition maps,
- (iii) Flux prints in triangular mesh configuration,
- (iv) Flux contour map,
- (v) Flux prints in hexagonal mesh configuration.

2.3.2 Subroutine TRI2DA: A 2-dimensional Diffusion Calculation Code for Adjoint Flux in Uniform Triangular Mesh Configuration

It is desirable to develop an adjoint flux calculation routine in the same core configuration as TRI2D for the use of the reactivity worth calculation.

The basic equation for adjoint flux is written as

$$\int_{S_i} D_{s,i} \nabla \phi_s^{*i} n_{\perp} dS_i - \int_{V_i} \Sigma_{T,i} \phi_s^{*i} dV_i + \int_{V_i} \hat{S}_s^{*i} dV_i = 0, \quad (2.3.2-1)$$

where

ϕ_s^{*i} = adjoint flux,

\hat{S}_s^{*i} = source,

$$\hat{S}_s^{*i} = \lambda (\nu \Sigma_{f,i}^i) \sum_j \chi^j \phi_s^{*j} + \sum_{j=1}^N \phi_s^{*j} \Sigma_{s,s}^{i \rightarrow j}, \quad (2.3.2-2)$$

i, j = energy suffixes,

N = maximum energy number.

Other notations are the same as those in § 2.3.1. Final equations to be solved are

$$\phi_s^{*n} = (F_L^n + F_R^n + F_T^n + L_s^{*n})^{-1} (F_L^n \phi_L^{*n} + F_R^n \phi_R^{*n} + F_T^n \phi_T^{*n} + Q_s^{*n} + R_s^{*n}), \quad (2.3.2-3)$$

where

$$L_s^{*n} = \{ \Sigma_{T,s}^n + D_{s,i}^n (B_{z,s}^2)^n \} V_s \phi_s^{*n},$$

$$Q_s^{*n} = \nu \Sigma_{f,i}^n \lambda \sum_{j=1}^N (\chi^j \phi_s^{*j}) V_s,$$

$$R_s^{*n} = \sum_{n \neq l} \Sigma_{s,s}^{n \rightarrow l} \phi_s^{*l} V_s.$$

Other terms are the same as Eq. (2.3.1-8) in the case of real flux calculation. In addition, the treatment of the boundary conditions are the same as those for previous real flux case. Ordinary S.O.R. method was adopted to solve the systems of Eqs. (2.3.2-3). That is, the iteration was made in the order of energy groups and triangular elements. Convergence criteria and outputs are the similar to those used for the real flux calculation code TRI2D.

2.3.3 Subroutine TRIPOW: A Power Distribution Calculation Routine

For the 2-dimensional detailed power distribution calculation in triangular mesh configuration, we prepared the routine TRIPOW. In this routine, power is usually used as the information of relative value because the results are obtained from 2-dimensional calculation. Therefore the following normalization is adopted to have unit total power:

$$\int_{\text{energy}} \int_{\text{reactor}} \phi \Sigma_i dV dE = 1.0$$

$$\text{i.e.: } \sum_s (\sum_j \phi_s^j \Sigma_{i,s}^j) = 1.0,$$

where macroscopic fission cross sections are transferred from the logical unit F03.

The output form is similar to those in TRI2D real flux case.

2.3.4 Inclusion of TRI-2D into HONEYCOMB System

TRI2D and TRI2DA had been originally developed for the standalone code in order to check the accuracy of the hexagonal mesh configuration code. So as to increase the generality of the HONEYCOMB, inclusion of these codes was requested. By this time, besides the original HONEYCOMB flow, RZ-HEXA-HEXAZ, new flow RZ-TRI2D-HEXAZ was added. Selection of the flow is made by user's choice.

In the inclusion of TRI2D and TRI2DA, we combined these two codes to make a new package of 2-dimensional calculation module TRI2DP. This TRI2DP calculation module has been constructed from following subroutines: TRI2D, TRIH, TRI2DA, TRIPOW, XREFH, CDEFH, EDDEFH, TRIEDT, TRIADT, TEDITH, TRPRTH, TRCNTH, TRPNTH, REACTB, HEXPRT, HXPR and HXPRA.

Due to the inclusion of above routines, modified subroutines in the original HONEYCOMB system are MAIN, HEXA, COLLAP, MICRO and HXADJ.

For the choice of the calculational flow of TRI2D or HEXA, one more data card becomes necessary from the above modification. Other input cards are the same as the original HONEYCOMB system. A new HONEYCOMB system including TRI2DP requires the computer core memory of 512K bytes in the standard overlay structure. The items of the core memory are shown in TABLE 2.3.4-1. Typical running time for a 2-group problem with one through flow of TRI2D-TRI2DA-TRIPOW, is about 60sec on the IBM-360/K195 machine. On the occasion of running, one more logical unit (F51) is necessary in order to keep the data of ϕ , ϕ^* , macroscopic Σ , core specification data etc.

TABLE 2.3.4-1 The items of the computer core memory

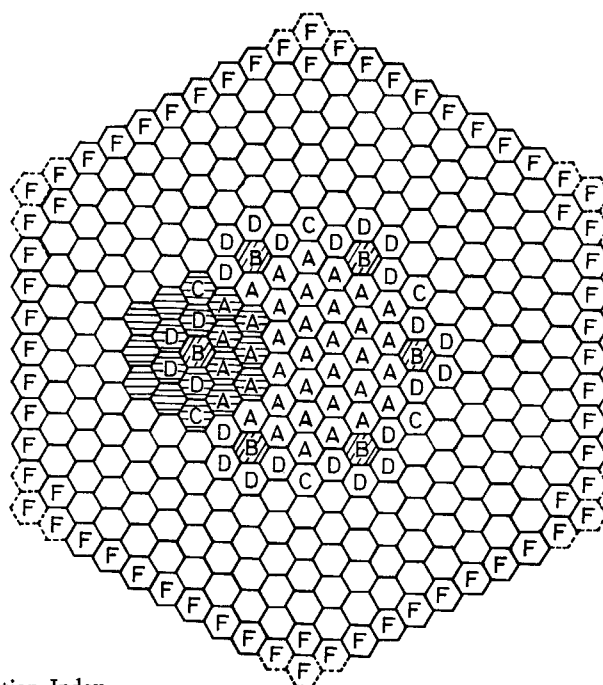
PROGRAM AREA	424 K Bytes
WORK AREA FOR MULTI-JOB	12 K Bytes
AREA for DD STATEMENT	6 K Bytes
I/O BUFFER AREA	70 K Bytes
TOTAL	512 K Bytes

2.3.5 Comparison between Calculational Results of TRI2D and HEXA

In this section, we discuss about the intercomparison of the nuclear characteristics obtained

by TRI2D and HEXA. Detailed description of the 2-dimensional hexagonal diffusion code HEXA is given in § 2.4.2. The main point of the discussion is that the influence of the mesh size on the nuclear characteristics such as the effective multiplication factor, control rod worth and flux distribution.

For the calculational model, we adopted a similar matrix to Mark I core configuration of "JOYO", but not an exact one. The calculational conditions are the same for both codes. For example, macroscopic cross sections including B_z^2 are the same as those values prepared by r - z calculation routines in the HONEYCOMB system. And we adopted the same convergence criteria.



Position Index

- A Fuel Element
- B Control Rod
- C Na-Channel
- D Fuel Element
- E Radial Blanket
- F SUS Reflector


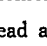
The elements that have no index refer element of type E, i.e.  should be read as .

Fig. 2.3.5-1 Standard core configuration for the calculational model of Case 1 and Case 2.

TABLE 2.3.5-1 Composition index for each sample case

Position index Case #	A	B	C	D	E	F	Note
1	#1	#1	#1	#1	#1	#1	1 Region problem
2-1	#1	#1	#1	#4	#5	#7	2 Region problem
2-2	#1	#3	#3	#4	#5	#7	Standard core rod-out case
2-3	#1	#2	#3	#4	#5	#7	Standard core rod-in case

Dictionary of composition index

#1, #4	Fuel element
#2	^{10}B control rod
#3	Na-channel
#5	Radial blanket
#7	SUS. reflector

(#1 and #4 are the same composition.)

TABLE 2.3.5-2 Calculated k_{eff} for Case 1
(one region problem)

Code	k_{eff}
HEXA	1.32584
TRI2D	1.32389
Difference (TRI2D-HEXA)	-0.00195

TABLE 2.3.5-3 Neutron balance for Case 1 with the production rate
=100

Code	Absorption rate	Leakage rate
HEXA	65.737	9.688
TRI2D	65.737	9.800

$$k_{eff} = \frac{\text{Production}}{\text{Leak} + \text{Absorption}}$$

Case 1. Cross check of the TRI2D and HEXA

For the cross check of these codes, we tried the calculation in the simplest core configuration with only one region. All reactor elements (core and blanket elements) are composed of type 1 (#1) fuel elements only. For details, Fig. 2.3.5-1 and TABLE 2.3.5-1 should be consulted. The multiplication factors obtained from these codes and the difference between the values are shown in TABLE 2.3.5-2, and the components in neutron balance are given in TABLE 2.3.5-3.

In this check calculation, disagreement of these codes is relatively small. It is seen from TABLE 2.3.5-3 that the difference of 0.2% in k_{eff} is caused by the leakage term. This would be the consequence of a minor difference in treatment of the boundary conditions in these two codes, that is, correction factors in $F_{l,b}$ are different in a few boundary elements. In this case, because of the lack of reflector or blanket elements, fairly large leakage (~9.7%) occurred at the vacuum boundary. But in the usual core configuration such as JOYO, LEAKAGE RATE/ PRODUCTION RATE is nearly equal to 3%, therefore the difference in k_{eff} 's obtained with HEXA and TRI2D will be less than 0.1%. So there is no problem for these two codes to deal with reactor systems with homogenized non-isolated compositions.

Case 2. The difference in k_{eff} 's produced by the inclusion of singular elements

The standard core configuration is already illustrated in Fig. 2.3.5-1, the composition of which is given in TABLE 2.3.5-1. The composition index #2 is the ^{10}B control rod (fully inserted) and #3 is the Na-channel left after the withdrawal of ^{10}B rod out of the core.

The following three cases of calculation were performed by both the codes under the same calculational conditions. Case 2-1 where B and C elements are replaced by #1 fuel elements simulates a simple 2-region problem. Case 2-2 where B and C elements are replaced by #3 elements simulates the system in which all control rods are out of the core, and Case 2-3 where B and C elements in the standard core configuration exist in the core simulates the state of six control rods are fully inserted. It is clear from the above description that in the order of Cases 1, 2-1, 2-2 and 2-3, a singularity of nuclear property is gradually introduced into the system.

The difference between these two codes are evident from TABLE 2.3.5-4. As the singularity, the difference in the k_{eff} is enlarged from 0.2% for Case 1 to 2.2% for Case 2-3. This difference is much serious for the calculation of control rod worth.

As for the control rod worth, from the results of Cases 2-2 and 2-3, we obtained the values

TABLE 2.3.5-4 Calculated k_{eff} 's from HEXA and TRI2D
codes for Cases 2-1~2-3

Case #	HEXA	TRI2D	Difference (TRI2D-HEXA)
2-1	1.1485	1.1429	-0.0056
2-2	1.07448	1.06593	-0.00855
2-3	0.97669	0.95475	-0.02194

TABLE 2.3.5-5 Calculated control rod worths
obtained by HEXA and TRI2D
codes

Code	$\Delta\rho$ (rod worth)
HEXA	9.41%
TRI2D	10.92%
Difference (TRI2D-HEXA)	*1.51%

$$\Delta\rho = \frac{k(\text{Rod Out}) - k(\text{Rod In})}{k(\text{Rod Out}) \cdot k(\text{Rod In})}$$

shown in TABLE 2.3.5-5. There is about 1.5% difference in the absolute total rod worths of these two codes. This value is recognized as extremely large for the rod worth calculation, because the total worth is about 10% with 6 control rods, and the difference of 1.5% amounts to about 1/6 of its value say one rod worth value. This difference is too large to be allowed for the reactor design calculation. Also this affects the neutron economy and other nuclear characteristics.

For the flux distribution, very large differences are also found between these two codes. Flux ratios of TRI2D and HEXA normalized at the flux peak position (at the core center) in the energy group 1 are shown in Figs. 2.3.5-2 and 2.3.5-3. The former figure shows Rod-Out Case and the latter Rod-In Case. In these figures, the ratios are shown only for three zones around the control rod position. These area in the standard core configuration is shown in Fig. 2.3.5-1 with horizontal hatched lines.

Fairly large differences are seen in Figs. 2.3.5-2 and 2.3.5-3. In Rod-Out Case of Fig. 2.3.5-2, disagreements of the group 1 fluxes around the Na-channel (#3) is within 1.5%, but in the blanket element, about 4% disagreements are seen for almost all elements. For the group 2 flux, as contrast to the group 1, the difference around Na-channel is remarkable. The differences are 14% in Na-channel and 9% in fuel elements of type #4.

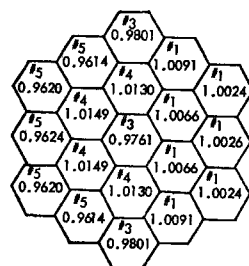
In Rod-In Case of Fig. 2.3.5-3, at the control rod position there is about 10% disagreement of the group 1 flux and 5% in the second zone around the control rod, but beyond these regions, the disagreement is not so large. For the group 2 flux, a marked 30% difference is found at the control rod position and a fairly large deviation is seen around the control rod. Also disagreements of 5~10% are still found in the third layer, particularly in the blanket elements.

It is seen from above results, that in the lower energy region the HEXA code considerably overestimates the flux depression in the control rods, and in turn it fairly underestimates the control rod worth.

From these results and discussions, the following conclusions can be drawn; (1) When a locally isolated strong absorber such as ^{10}B control rod is introduced in the system, the difference in the fluxes in that position is very large, about 30%, between these two codes. (2) When a locally isolated strong scatterer such as Na-channel is introduced in the system, the difference in the fluxes is still found between these two codes but the extent is not so large. (3) For the

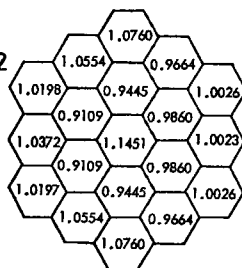
ROD-OUT CASE (CASE 2-2)

GROUP=1



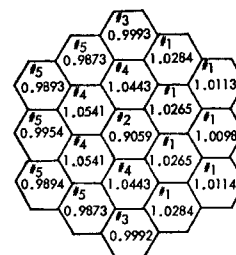
Material Index
 #1 Fuel Element
 #3 Na-Channel
 #4 Fuel Element
 #5 Radial Blanket

GROUP=2



ROD-IN CASE (CASE 2-3)

GROUP=1



Material Index
 #1 Fuel Element
 #2 Control Rod
 #3 Na-Channel
 #4 Fuel Element
 #5 Radial Blanket

GROUP=2

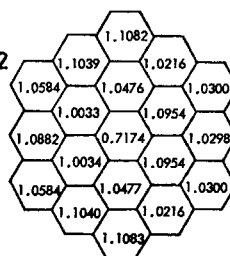


Fig. 2.3.5-2 Flux ratios $\phi(\text{HEXA})/\phi(\text{TRI-2D})$ for Case 2-2 (values are shown only for three zones around the control rod position).

Fig. 2.3.5-3 Flux ratios $\phi(\text{HEXA})/\phi(\text{TRI-2D})$ for Case 2-3 (values are shown only for three zones around the control rod position).

system without singularity, the agreement is quite well between these two codes

Summarizing these, the introduction of the singularity in the system brings about substantial deviations between HEXA and TRI2D codes in the nuclear characteristics such as the flux and k_{eff} , that is, the mesh configuration or mesh spacing leads to a considerable effects to the nuclear characteristics. So it is very important for the calculation of the accurate nuclear characteristics in multi-dimensional problem to find a preferable mesh configuration and appropriate mesh sizes, or some correction methods for the approximation.

2.4 Three-dimensional Criticality Calculation

In this section, the few-group constants prepared in §2.2 are utilized in 2- and 3-dimensional criticality calculations based on the diffusion model. Consequently, obtained are 3-dimensional neutron flux distribution, critical insertion depth of control rods and 3-dimensional adjoint neutron flux distribution. One nodal point is taken at the center of each hexagon illustrated in Fig. 2.1.1-1. On the axial coordinate (see Fig. 2.1.1-2), mesh intervals are taken rather freely and a nodal point is fixed at the middle point of each interval.

As described in Chap. 1, the neutron flux in outer radial zones are approximated by 2-dimensional r - z (§2.4.1) and 2-dimensional hexagonal (§2.4.2) fluxes.

From the conclusion obtained in §2.3.5, a correction method is applied so as to enhance the accuracy of the predicted neutron flux in and around the control rod assemblies (§2.4.4). The section 2.4.5 describes the method of criticality adjustment by varying the insertion depth of some control rods. Calculational method of adjoint flux is shown in §2.4.6.

2.4.1 Two-dimensional r - z Diffusion Code RZ

Here, the few-group diffusion equations are solved in r - z geometry shown in Fig. 2.1.1-2 with more detailed meshes than in the code RZ25 described in §2.2.3. The r - z space is divided into rectangular mesh regions (area of each mesh region is $\Delta r_j \times \Delta z_k$), and a nodal point is fixed at the center of each mesh region. The flux value obtained at the nodal point is assumed to be the spatial average over the mesh region. As to energy variable, the regular flux ϕ_{jk}^n is, as well known, the integrated value over the n -th energy (or lethargy) interval, while the adjoint flux ϕ_{jk}^{*n} is the average value in that interval. This is clear because the scattering matrix $\sigma_{s,i \rightarrow j}$ is defined as an averaged value about group i but integrated value about group j , and is used in the NMAX-group diffusion equations as follows:

$$\begin{cases} -D^n \nabla^2 \phi^n + \Sigma_T^n \phi^n = \lambda \chi^n \sum_l (\nu \Sigma_f)^l \phi^l + \sum_{l=1}^{n-1} \Sigma_s^{l \rightarrow n} \phi^l, \\ -D^n \nabla^2 \phi^{*n} + \Sigma_T^n \phi^{*n} = \lambda (\nu \Sigma_f)^n \sum_l \chi^l \phi^{*l} + \sum_{l=n+1}^{\text{NMAX}} \Sigma_s^{n \rightarrow l} \phi^{*l}, \end{cases}$$

where λ is the reciprocal of the effective multiplication factor k_{eff} .

The difference equations for numerical solution is obtained by integrating the equations over the (j, k) -th mesh region (V_{jk}), that is, the j -th annular zone from the cylinder axis and the k -th layer from the top.

We describe here only the equations for the regular flux:

$$\begin{aligned} & \int_{\Delta r_j} 2\pi r dr \int_{\Delta z_k} dz \left[D^n \nabla^2 \phi^n - \Sigma_T^n \phi^n + \lambda \chi^n \sum_l (\nu \Sigma_f)^l \phi^l + \sum_{l=1}^{n-1} \Sigma_s^{l \rightarrow n} \phi^l \right] \\ & = \int_{S_{jk}} [D^n \nabla_{\perp} \phi^n] dS + \int_{V_{jk}} \left[-\Sigma_T^n \phi^n + \lambda \chi^n \sum_l (\nu \Sigma_f)^l \phi^l + \sum_{l=1}^{n-1} \Sigma_s^{l \rightarrow n} \phi^l \right] dV = 0. \end{aligned}$$

The net current through a unit area of an interface S_{jk} is assumed, for example, at the bound-

ary between V_{jk} and $V_{j+1,k}$, to be written as

$$\begin{aligned} D^n \nabla_{\perp} \phi^n &= \frac{\frac{\Delta r_j}{2} + \frac{\Delta r_{j+1}}{2}}{\frac{1}{D_{jk}^n} \cdot \frac{\Delta r_j}{2} + \frac{1}{D_{j+1,k}^n} \cdot \frac{\Delta r_{j+1}}{2}} \cdot \frac{\phi_{j+1,k}^n - \phi_{jk}^n}{\frac{\Delta r_j}{2} + \frac{\Delta r_{j+1}}{2}} \\ &= \left(\frac{1}{D_{jk}^n} \cdot \frac{\Delta r_j}{2} + \frac{1}{D_{j+1,k}^n} \cdot \frac{\Delta r_{j+1}}{2} \right)^{-1} (\phi_{j+1,k}^n - \phi_{jk}^n). \end{aligned}$$

Then the difference equation becomes

$$\phi_{jk}^n = \frac{\left(a_{1,jk}^n \phi_{j-1,k}^n + a_{1,j+1,k}^n \phi_{j+1,k}^n + a_{2,jk}^n \phi_{j,k-1}^n + a_{2,j,k+1}^n \phi_{j,k+1}^n + \lambda \chi^n \sum_l a_{4,jk}^l \phi_{jk}^l + \sum_{l=1}^{n-1} a_{5,jk}^{l \rightarrow n} \phi_{jk}^l \right)}{(a_{1,jk}^n + a_{1,j+1,k}^n + a_{2,jk}^n + a_{2,j,k+1}^n + a_{3,jk}^n)}, \quad (2.4.1-1)$$

where

$$(1) \quad a_{1,jk}^n = 2\pi r_{Lj} \Delta z_k \left(\frac{1}{D_{jk}^n} \cdot \frac{\Delta r_j}{2} + \frac{1}{D_{j-1,k}^n} \cdot \frac{\Delta r_{j-1}}{2} \right)^{-1} = \frac{4\pi r_{Lj}}{\Delta r_{j-1}} \Delta z_k \left(\frac{\Delta r_j}{\Delta r_{j-1}} \cdot \frac{1}{D_{jk}^n} + \frac{1}{D_{j-1,k}^n} \right)^{-1}$$

(suffix L means the left side of the region V_{jk}).

By the symmetry condition at cylinder axis, we can put $a_{11k}^n = 0$.

$$(2) \quad a_{1,j+1,k}^n = \frac{4\pi r_{Rj}}{\Delta r_j} \Delta z_k \left(\frac{\Delta r_{j+1}}{\Delta r_j} \cdot \frac{1}{D_{j+1,k}^n} + \frac{1}{D_{jk}^n} \right)^{-1}$$

($r_{Rj} = r_{L,j+1}$ where R means the right side).

At the outermost boundary ($j=N$), $a_{1,N+1,k}^n$ is determined from the relation:

$$a_{1,N+1,k}^n \phi_{Nk}^n = 2\pi r_{RN} \Delta z_k [-D_{Nk}^n \nabla_r \phi^n(r_{RN}, z_k)].$$

Using the vacuum boundary condition (r_{RN} being sufficiently large),

$$-\nabla_r \phi^n(r_{RN}, z_k) = \frac{\phi^n(r_{RN}, z_k)}{0.71044 \lambda_{tr,N,k}^n} = \frac{\phi^n(r_{RN}, z_k)}{2.1313 D_{Nk}^n},$$

we can write

$$a_{1,N+1,k}^n = 2\pi r_{RN} \Delta z_k \frac{\phi^n(r_{RN}, z_k)}{2.1313} \cdot \frac{1}{\phi_{Nk}^n}.$$

Now, by using the following form:

$$\begin{aligned} \phi_{Nk}^n &= \phi^n \left(r_{RN} - \frac{1}{2} \Delta r_N, \Delta z_k \right) \doteq \phi^n(r_{RN}, z_k) - \frac{\Delta r_N}{2} \nabla_r \phi^n(r_{RN}, z_k) \\ &= \phi^n(r_{RN}, z_k) + \frac{\Delta r_N}{2} \cdot \frac{\phi^n(r_{RN}, z_k)}{2.1313 D_{Nk}^n}, \end{aligned}$$

we obtain

$$\phi^n(r_{RN}, z_k) / \phi_{Nk}^n = \left(1 + \frac{\Delta r_N}{2} \cdot \frac{1}{2.1313 D_{Nk}^n} \right)^{-1}.$$

Then finally we have

$$a_{1,N+1,k}^n = 2\pi r_{RN} \Delta z_k \left(2.1313 + \frac{\Delta r_N}{2} \cdot \frac{1}{D_{Nk}^n} \right)^{-1} = \frac{4\pi r_{RN}}{\Delta r_N} \Delta z_k \left(\frac{4.2626}{\Delta r_N} + \frac{1}{D_{Nk}^n} \right)^{-1}.$$

When $j=N$, this $a_{1,N+1,k}^n$ is used only in the denominator of Eq. (2.4.1-1). In the numerator, the term of $\phi_{N+1,k}^n$ should be zero. The same are the cases of the following $a_{2,j1}^n$ and $a_{2,j,M+1}^n$.

$$(3) \quad a_{2,jk}^n = \pi(r_{Rj}^2 - r_{Lj}^2) \left(\frac{1}{D_{jk}^n} \cdot \frac{\Delta z_k}{2} + \frac{1}{D_{j,k-1}^n} \cdot \frac{\Delta z_{k-1}}{2} \right)^{-1} = 2\pi(r_{Rj}^2 - r_{Lj}^2) \left(\frac{\Delta z_k}{D_{jk}^n} + \frac{\Delta z_{k-1}}{D_{j,k-1}^n} \right)^{-1}.$$

At the uppermost boundary ($k=1$),

$$a_{2,j1}^n = 2\pi(r_{Rj}^2 - r_{Lj}^2) \left(4.2626 + \frac{\Delta z_1}{D_{j1}^n} \right)^{-1}.$$

$$(4) \quad a_{2,j,k+1}^n = 2\pi(r_{Rj}^2 - r_{Lj}^2) \left(\frac{\Delta z_{k+1}}{D_{j,k+1}^n} + \frac{\Delta z_k}{D_{jk}^n} \right)^{-1}.$$

At the lowest boundary ($k=M$),

$$a_{2,j,M+1}^n = 2\pi(r_{Rj}^2 - r_{Lj}^2) \left(4.2626 + \frac{\Delta z_M}{D_{jM}^n} \right)^{-1}.$$

$$(5) \quad a_{3jk}^n = \pi(r_{Rj}^2 - r_{Lj}^2) \Delta z_k \Sigma_{Tjk}^n \equiv V_{jk} \Sigma_{Tjk}^n.$$

$$(6) \quad a_{4jk}^n = V_{jk} (\nu \Sigma_f)_{jk}^n.$$

$$(7) \quad a_{5jk}^{l \rightarrow n} = V_{jk} \Sigma_{s,jk}^{l \rightarrow n}.$$

The equation (2.4.1-1) is solved by a simple iterative sweeping method (EQUIPOISE method). The ϕ_{jk}^n is calculated using new values of $\phi_{j-1,k}^n$, $\phi_{j,k-1}^n$ and ϕ_{jk}^l ($l < n$), and old values of $\phi_{j+1,k}^n$, $\phi_{j,k+1}^n$ and ϕ_{jk}^l ($l \geq n$). To accelerate the convergence, the ordinary over-relaxation method is applied in the same way as in the EQUIPOISE code¹³⁾. After each iteration, eigenvalue λ is renewed by

$$\begin{aligned} \lambda = & \sum_n \left\{ \sum_j (a_{2j1}^n \phi_{j1}^n + a_{2,j,M+1}^n \phi_{jM}^n) + \sum_k a_{1,N+1,k}^n \phi_{Nk}^n \right. \\ & \left. + \sum_j \sum_k \left(a_{3jk}^n - \sum_{l=n+1}^{NMAX} a_{5^{n \rightarrow l}}^n \right) \phi_{jk}^n \right\} / \sum_n \sum_j \sum_k a_{4jk}^n \phi_{jk}^n \\ = & [\{ \text{Total Leakage} \} (L) + \{ \text{Total Absorption} - \text{Net Gain by} \\ & (n, 2n) \text{ or } (n, 3n) \text{ Reaction} \} (A)] / \{ \text{Total Production} \} (P). \end{aligned}$$

It is clear that λ becomes k_{eff}^{-1} when convergence is attained. Criteria for convergence¹³⁾ are 10^{-5} , 10^{-4} and 10^{-3} for the eigenvalue, residual and flux ϕ_{jk}^n , respectively.

When ϕ_{jk}^n is obtained, two kinds of the following data are prepared for use in § 2.4.2 and § 2.4.3.

(i) Buckling in z -direction for each group is obtained for use in the mid-plane hexagonal (§ 2.4.2) or triangular (§ 2.3) calculation. Letting l' be the zone index, the buckling is given by

$$\begin{aligned} (B_z^2)_{l'}^n = & \sum_{j \in l'} \{ a_{2,j,KBZ1}^n (\phi_{j,KBZ1}^n - \phi_{j,KBZ1-1}^n) + a_{2,j,KBZ2+1}^n (\phi_{j,KBZ2}^n - \phi_{j,KBZ2+1}^n) \} / \\ & \sum_{j \in l'} \sum_{k=KBZ1}^{KBZ2} \pi(r_{Rj}^2 - r_{Lj}^2) \Delta z_k \phi_{jk}^n D_{jk}^n, \end{aligned}$$

where KBZ1 and KBZ2 are respectively the first and last mesh interval contained in the fuel region in the z -direction. This equation is derived from the following reasoning:

$$\begin{aligned} B_z^2 \phi &= -\nabla^2 \phi, \\ D(B_z^2 + B_r^2) \phi &= -D \nabla^2 \phi, \\ (B_z^2 + B_r^2) \int_V D \phi dV &= \int_{S_z} J_z dS + \int_{S_r} J_r dS, \\ B_z^2 &= \int_{S_z} J_z dS / \int_V D \phi dV. \end{aligned}$$

(ii) For synthesizing the 3-dimensional approximate flux $\hat{\phi}_{ijk}^n$, a normalized distribution function ϕ_{lk}^n is defined for each hexagonal zone l :

$$\begin{aligned} \phi_{lk}^n = & \sum_{j \in l} \pi(r_{Rj}^2 - r_{Lj}^2) \phi_{jk}^n / \sum_{k=1}^M \sum_{j \in l} \pi(r_{Rj}^2 - r_{Lj}^2) \Delta z_k \phi_{jk}^n \\ (\sum_k \phi_{lk}^n \Delta z_k &= 1 \text{ for each } n \text{ and } l). \end{aligned}$$

2.4.2 Two-dimensional Hexagonal Diffusion Code HEXA

In x - y mid-plane, 2-dimensional flux distribution is obtained at the central height of fuel part. The x and y axes are fixed to cross with angle of $\pi/3$, and the coordinates are taken so as to contain the 331 assemblies of pitch t shown in Fig. 2.1.1-1. Then each assembly is numbered like (j, i) as illustrated in Figs. 2.4.2-1 and 2.4.2-2, where $h = j + i - 11$.

By integrating the diffusion equation over one hexagonal assembly, we obtain the difference

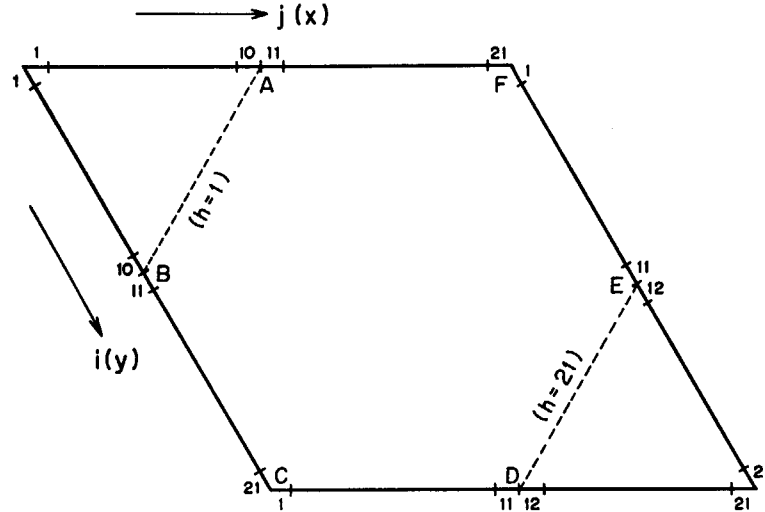


Fig. 2.4.2-1 Coordinates for the 2-dimensional hexagonal lattice.

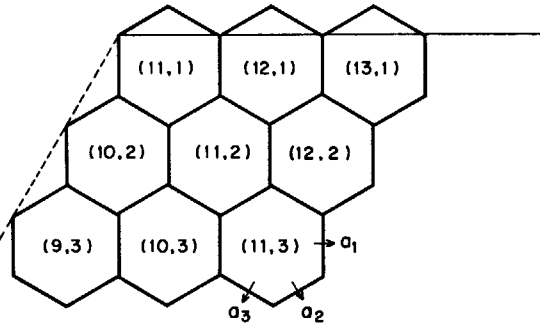


Fig. 2.4.2-2 Arrangement of the hexagonal assemblies in the upper-left corner A shown in Fig. 2.4.2-1.

equation in the same way as in §2.4.1:

$$\phi_{ji}^n = \left(b_{ji}^n + \lambda \chi^n \sum_l a_{5ji}^l \phi_{ji}^l + \sum_{l=1}^{n-1} a_{6ji}^{l \rightarrow n} \phi_{ji}^l \right) / c_{ji}^n, \quad (2.4.2-1)$$

where

$$\begin{aligned} b_{ji}^n &= a_{1ji}^n \phi_{j-1,i}^n + a_{1,j+1,i}^n \phi_{j+1,i}^n + a_{2ji}^n \phi_{j,i-1}^n + a_{2,j,i+1}^n \phi_{j,i+1}^n \\ &\quad + a_{3,j+1,i}^n \phi_{j+1,i-1}^n + a_{3,j,i+1}^n \phi_{j-1,i+1}^n, \\ c_{ji}^n &= a_{1ji}^n + a_{1,j+1,i}^n + a_{2ji}^n + a_{2,j,i+1}^n + a_{3,j+1,i}^n + a_{3,j,i+1}^n + a_{4ji}^n, \\ \lambda &= (L+A)/P, \\ L &= \sum_n \left\{ \sum_{i=1}^{21} (a_{1ji}^n \phi_{ji}^n + a_{1,j+1,i}^n \phi_{j+1,i}^n) \right. \\ &\quad + \sum_{j=1}^{21} (a_{2ji}^n \phi_{ji}^n + a_{2,j,i+1}^n \phi_{j,i+1}^n) \\ &\quad \left. + \sum_{h=1}^{21} (a_{3,j+1,i}^n \phi_{j+1,i}^n + a_{3,j,i+1}^n \phi_{j,i+1}^n) \right\}, \end{aligned}$$

in which (j_1, i) means the coordinates of 21 assemblies along the side of (AB+BC) in Fig. 2.4.2-1, and

$$\begin{aligned} (j_2, i) &: (FE+ED), \\ (j, i_1) &: (BA+AF), \\ (j, i_2) &: (CD+DE), \\ (j_3, i_3) &: (AF+FE), \\ (j_4, i_4) &: (BC+CD), \end{aligned}$$

$$A = \sum_n \sum_j \sum_i \left(a_{4ji}^n - \sum_{l=n+1}^{\text{NMAX}} a_{6ji}^{n \rightarrow l} \right) \phi_{ji}^n,$$

$$P = \sum_n \sum_j \sum_i a_{5ji}^n \phi_{ji}^n.$$

The directions of vectors a_k ($k=1, 2, 3$) are shown in Fig. 2.4.2-2, whose components are defined as follows:

$$(1) \quad a_{1ji}^n = \frac{t}{\sqrt{3}} \left(\frac{1}{D_{ji}^n} \cdot \frac{t}{2} + \frac{1}{D_{j-1,i}^n} \cdot \frac{t}{2} \right)^{-1} = \frac{2}{\sqrt{3}} \left(\frac{1}{D_{ji}^n} + \frac{1}{D_{j-1,i}^n} \right)^{-1}.$$

When $i=1$ (AF) or $i=21$ (CD), a_{1ji}^n is multiplied by 1.25 because a_{1ji}^n is the coefficient of the current in the j -direction, and the jagged part (see Fig. 2.4.2-2) must be flattened.

When $j=j_1$ (AB+BC), the vacuum boundary condition is used like in the previous section,

$$a_{1ji}^n = \frac{2}{\sqrt{3}} \left(\frac{4.2626}{t} + \frac{1}{D_{ji}^n} \right)^{-1}.$$

However, when $i \neq 11$, a_{1ji}^n is multiplied by $\sqrt{3}/2$ in order to convert the leakage to the direction perpendicular to the macroscopic side of reactor (AB or BC). Then,

$$a_{1ji}^n = \begin{cases} \frac{2}{\sqrt{3}} \left(\frac{1}{D_{ji}^n} + \frac{1}{D_{j-1,i}^n} \right)^{-1} & (j \neq j_1, i \neq 1, i \neq 21), \\ \frac{5}{2\sqrt{3}} \left(\frac{1}{D_{ji}^n} + \frac{1}{D_{j-1,i}^n} \right)^{-1} & (j \neq j_1, i = 1 \text{ or } i = 21), \\ \left(\frac{4.2626}{t} + \frac{1}{D_{ji}^n} \right)^{-1} & (j = j_1, i \neq 11), \\ \frac{2}{\sqrt{3}} \left(\frac{4.2626}{t} + \frac{1}{D_{ji}^n} \right)^{-1} & (j = j_1, i = 11). \end{cases}$$

$$(2) \quad a_{1,j+1,i}^n = \frac{2}{\sqrt{3}} \left(\frac{1}{D_{j+1,i}^n} + \frac{1}{D_{ji}^n} \right)^{-1}.$$

The treatment at the outer sides is the same as in Item (1).

$$(3) \quad a_{2ji}^n = \frac{2}{\sqrt{3}} \left(\frac{1}{D_{ji}^n} + \frac{1}{D_{j,i-1}^n} \right)^{-1}.$$

$$(4) \quad a_{2,i,i+1}^n = \frac{2}{\sqrt{3}} \left(\frac{1}{D_{j,i+1}^n} + \frac{1}{D_{ji}^n} \right)^{-1}.$$

$$(5) \quad a_{3,j+1,i}^n = \frac{2}{\sqrt{3}} \left(\frac{1}{D_{ji}^n} + \frac{1}{D_{j+1,i-1}^n} \right)^{-1}.$$

$$(6) \quad a_{3,j,i+1}^n = \frac{2}{\sqrt{3}} \left(\frac{1}{D_{j-1,i+1}^n} + \frac{1}{D_{ji}^n} \right)^{-1}.$$

$$(7) \quad a_{4ji}^n = \frac{\sqrt{3}}{2} t^2 \{ \Sigma_{Tji}^n + (B_z^2)_{ji}^n D_{ji}^n \}.$$

$$(8) \quad a_{5ji}^n = \frac{\sqrt{3}}{2} t^2 (\nu \Sigma_f)_{ji}^n.$$

$$(9) \quad a_{6ji}^{l \rightarrow n} = \frac{\sqrt{3}}{2} t^2 \Sigma_{aji}^{l \rightarrow n}.$$

Using the hexagonal flux ϕ_{ji}^n obtained by solving the Eq. (2.4.2-1), 3-dimensional approximate flux ϕ_{jik}^n is synthesized as the product of ϕ_{ji}^n and ϕ_{lk}^n of §2.4.1.

$$\phi_{jik}^n = \phi_{ji}^n \phi_{lk}^n \left| \sum_n \sum_k \sum_i \sum_j \frac{\sqrt{3}}{2} t^2 \Delta z_k (\nu \Sigma_f)_{jik}^n \phi_{ji}^n \phi_{lk}^n \right|,$$

where $(j, i) \in l$, that is, the lattice (j, i) belongs to the l -th ring. (When $j=i=11$, then $l=1$.)

For the outer 3 zones ($l=9, 10, 11$), this ϕ_{jik}^n is applied as the final result ϕ_{jik}^n .

In the next section 2.4.3, 3-dimensional diffusion equations are solved in the central radial zones including up to the 8-th ring and in all range in the z -direction. It is necessary to pre-

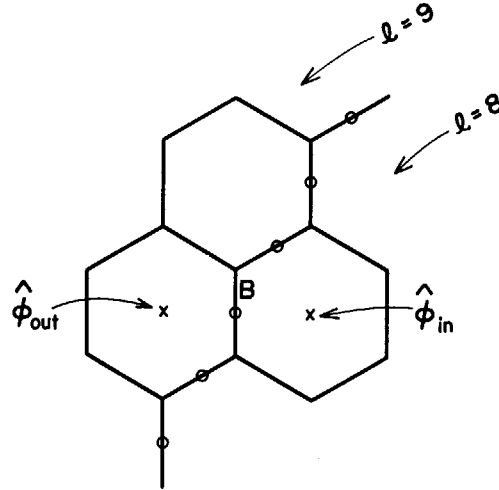


Fig. 2.4.2-3 The boundary surface between the 8-th and 9-th zones (—○—).

pare the following two data :

(i) Normalization factor for ϕ_{jik}^n :

$$TS = \sum_n \sum_k \sum_{l=1}^8 \sum_{(j,i) \in l} \frac{\sqrt{3}}{2} t^2 \Delta z_k (\nu \Sigma_t)_{jik} \phi_{jik}^n.$$

(ii) For each surface element between the 8-th and 9-th zones shown in Fig. 2.4.2-3, and for each group, a homogeneous boundary condition is determined as a_B below :

$$a_B \phi_{in} = \Delta S J_B,$$

where

$$\Delta S = \frac{t}{\sqrt{3}} \Delta z_k,$$

$$J_B = -D(\phi_{out} - \phi_{in})/t,$$

then we obtain $a_B = \frac{1}{\sqrt{3}} \Delta z_k D(\phi_{in} - \phi_{out})/\phi_{in}$.

2.4.3 Three-dimensional Hexagonal-z Diffusion Code HEXAZ

By using the normalization factor TS and the boundary condition a_B prepared in §2.4.2, criticality calculation is executed in the 3-dimensional hexagonal-z diffusion model, only for the inner 8 zones consisting of 169 assemblies of fuels, control rods and inner half of the blanket. A parallelogram like in Fig. 2.4.1-1 is drawn so as to contain the 169 assemblies. At this time, coordinates (j, i) are up to $(15, 15)$ and $h = j + i - 8$. The axial mesh structure is made common to that in §2.4.1. Integrating the diffusion equations over a volume segment (hexagonal column of height Δz and width t), the difference equations are obtained as

$$\phi_{jik}^n = \left(b_{jik}^n + \lambda \chi^n \sum_l a_{6jik}^l \phi_{jik}^l + \sum_{l=1}^{n-1} a_{7jik}^{l \rightarrow n} \phi_{jik}^l \right) / c_{jik}^n, \quad (2.4.3-1)$$

where

$$\begin{aligned} b_{jik}^n = & a_{1jik}^n \phi_{j-1,i,k}^n + a_{1,j+1,i,k}^n \phi_{j+1,i,k}^n + a_{2jik}^n \phi_{j,i-1,k}^n + a_{2,j,i+1,k}^n \phi_{j,i+1,k}^n \\ & + a_{3,j+1,i,k}^n \phi_{j+1,i-1,k}^n + a_{3,j,i+1,k}^n \phi_{j-1,i+1,k}^n \\ & + a_{4jik}^n \phi_{j,i,k-1}^n + a_{4,j,i,k+1}^n \phi_{j,i,k+1}^n, \end{aligned}$$

$$\begin{aligned} c_{jik}^n = & a_{1jik}^n + a_{1,j+1,i,k}^n + a_{2jik}^n + a_{2,j,i+1,k}^n + a_{3,j+1,i,k}^n + a_{3,j,i+1,k}^n \\ & + a_{4jik}^n + a_{4,j,i,k+1}^n + a_{5jik}^n, \end{aligned}$$

$$\lambda = (L + A)/P,$$

$$\begin{aligned} L = & \sum_n \left\{ \sum_{k=1}^{15} (a_{1jik}^n \phi_{j,i,k}^n + a_{1,j+1,i,k}^n \phi_{j+1,i,k}^n) + \sum_{k=1}^{15} (a_{2jik}^n \phi_{j,i,k}^n + a_{2,j,i+1,k}^n \phi_{j,i+1,k}^n) \right. \\ & \left. + \sum_{k=1}^{15} (a_{3,j+1,i,k}^n \phi_{j+1,i,k}^n + a_{3,j,i+1,k}^n \phi_{j,i+1,k}^n) \right\} \end{aligned}$$

$$+ \sum_i \sum_j (a_{4ji1}^n \phi_{ji1}^n + a_{4,j,i,M+1}^n \phi_{jiM}^n) \Big\}$$

((j_1, i, k), (j_2+1, i, k), ..., ($j, i, M+1$) mean the volume segments outermost of the region dealt with this 3-dimensional calculation),

$$A = \sum_n \sum_j \sum_i \sum_k \left(a_{5jik}^n - \sum_{l=n+1}^{NMAX} a_{7jik}^{n-l} \right) \phi_{jik}^n,$$

$$P = \sum_n \sum_j \sum_i \sum_k a_{6jik}^n \phi_{jik}^n.$$

The coefficients a are defined as follows:

$$(1) \quad a_{1jik}^n = \frac{2}{\sqrt{3}} \Delta z_k \left(\frac{1}{D_{jik}^n} + \frac{1}{D_{j-1,i,k}^n} \right)^{-1},$$

$$a_{1j,i,k}^n = a_{B1j,i,k}^n.$$

($a_{B1j,i,k}^n$ has been obtained in §2.4.2. At the boundary in radial direction, treatment is similar also to Items (2)~(6) below.)

$$(2) \quad a_{1,j+1,i,k}^n = \frac{2}{\sqrt{3}} \Delta z_k \left(\frac{1}{D_{j+1,i,k}^n} + \frac{1}{D_{jik}^n} \right)^{-1}.$$

$$(3) \quad a_{2jik}^n = \frac{2}{\sqrt{3}} \Delta z_k \left(\frac{1}{D_{jik}^n} + \frac{1}{D_{j,i-1,k}^n} \right)^{-1}.$$

$$(4) \quad a_{2,j,i+1,k}^n = \frac{2}{\sqrt{3}} \Delta z_k \left(\frac{1}{D_{j,i+1,k}^n} + \frac{1}{D_{jik}^n} \right)^{-1}.$$

$$(5) \quad a_{3,j+1,i,k}^n = \frac{2}{\sqrt{3}} \Delta z_k \left(\frac{1}{D_{jik}^n} + \frac{1}{D_{j+1,i-1,k}^n} \right)^{-1}.$$

$$(6) \quad a_{3,j,i+1,k}^n = \frac{2}{\sqrt{3}} \Delta z_k \left(\frac{1}{D_{j-1,i+1,k}^n} + \frac{1}{D_{jik}^n} \right)^{-1}.$$

$$(7) \quad a_{4jik}^n = \frac{\sqrt{3} t^2}{\Delta z_{k-1}} \left(\frac{\Delta z_k}{\Delta z_{k-1}} \cdot \frac{1}{D_{jik}^n} + \frac{1}{D_{j,i,k-1}^n} \right)^{-1}, \quad \text{for } k \neq 1,$$

$$a_{4ji1}^n = \frac{\sqrt{3} t^2}{\Delta z_1} \left(\frac{4.2626}{\Delta z_1} + \frac{1}{D_{ji1}^n} \right)^{-1}, \quad \text{for } k=1.$$

$$(8) \quad a_{4,j,i,k+1}^n = \frac{\sqrt{3} t^2}{\Delta z_k} \left(\frac{\Delta z_{k+1}}{\Delta z_k} \cdot \frac{1}{D_{j,i,k+1}^n} + \frac{1}{D_{jik}^n} \right)^{-1}, \quad \text{for } k \neq M,$$

$$a_{4,j,i,M+1}^n = \frac{\sqrt{3} t^2}{\Delta z_M} \left(\frac{4.2626}{\Delta z_M} + \frac{1}{D_{jiM}^n} \right)^{-1}, \quad \text{for } k=M.$$

$$(9) \quad a_{5jik}^n = \frac{\sqrt{3}}{2} t^2 \Delta z_k \Sigma_{T,jik}^n.$$

$$(10) \quad a_{6jik}^n = \frac{\sqrt{3}}{2} t^2 \Delta z_k (\nu \Sigma_f)_{jik}^n.$$

$$(11) \quad a_{7jik}^{l \rightarrow n} = \frac{\sqrt{3}}{2} t^2 \Delta z_k \Sigma_{s,jik}^{l \rightarrow n}.$$

After the iterative procedure is completed for Eq. (2.4.3-1), the 3-dimensional neutron fluxes ϕ_{jik}^n are normalized to yield neutron source of the amount of TS , that is, ϕ_{jik}^n 's are multiplied by a factor of

$$TS / \sum_n \sum_j \sum_i \sum_k a_{6jik}^n \phi_{jik}^n.$$

Then $\hat{\phi}_{jik}^n$'s obtained in the last section 2.4.2 are substituted by these normalized ϕ_{jik}^n 's except the outer three zones, and finally the flux distribution for 21×21 matrix (see Fig. 2.4.2-1) is determined:

$$\hat{\phi}_{jik}^n = \begin{cases} \phi_{j-3,i-3,k}^n, & (1 \leq l \leq 8), \\ \phi_{jik}^n, & (9 \leq l \leq 11), \end{cases}$$

where $\phi_{j-3,i-3,k}^n$ means that the normalized flux as the solution of Eq. (2.4.3-1) in the 15×15

matrix is adjusted to the 21×21 matrix about their coordinates.

2.4.4 Improvement of Accuracy of Predicted Neutron Flux Values in and Around Control Rods¹⁴⁾

From the conclusion given in §2.3.5, it is desirable that some correction method is devised to enhance the accuracy of the predicted neutron flux inside and in the vicinity of control rods. It is, however, difficult to increase the number of nodal points because the 3-dimensional calculation needs much computation time even in hexagonal- z mesh structure. Thus, the need is felt for a means to determine accurate flux values in the regions of interest without increasing the computing time, that is, without making mesh sizes fine.

We consider a hexagonal lattice of pitch t shown in Fig. 2.4.4-1, one hexagon of which is a homogeneous control rod. In §2.4.3, the net current through a unit area on S was expressed by

$$J = \left(\frac{D_1^{-1} + D_2^{-1}}{2} \right)^{-1} \frac{\bar{\phi}_2 - \bar{\phi}_1}{t}, \quad (2.4.4-1)$$

from which the difference equation for $\bar{\phi}_n$, Eq. (2.4.3-1), was derived. The $\bar{\phi}_n$ means the average flux in the hexagonal lattice n . However, when the lattice 1 is an absorber stronger than the neighbors and the lattice 2 is a fuel producing neutrons, the curvature of the spatial flux distribution changes its sign at the interface S , so that the expression (2.4.4-1) becomes a very poor approximation. It is noted that the solution obtained with the hexagonal mesh diffusion scheme gives a too small value of $\bar{\phi}_1$ compared with the triangular mesh diffusion, while, on the other hand, $\bar{\phi}_2$ is overestimated.

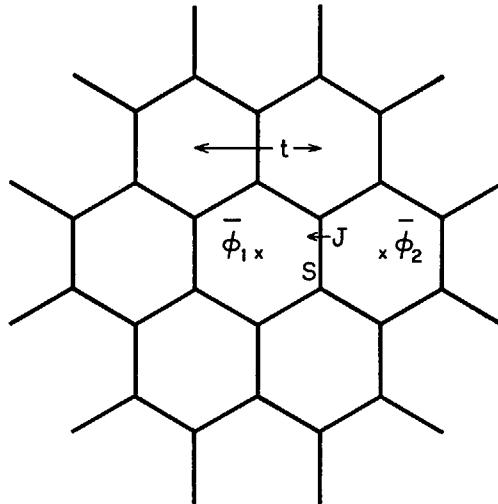


Fig. 2.4.4-1 Hexagonal lattice of pitch t .

TABLE 2.4.4-1 Group constants used in test calculations

		Control rod	Fuel
Group 1 (10.5 MeV ~ 465 eV)	χ	—	1
	D (cm)	1.826	1.689
	Σ_a (cm ⁻¹)	0.02911	0.007385
	Σ_s (cm ⁻¹)	0.2075	0.2451
	$\nu \Sigma_f$ (cm ⁻¹)	0	0.01031
	$\Sigma_s^{1 \rightarrow 1}$ (cm ⁻¹)	0.2065	0.2443
	$\Sigma_s^{1 \rightarrow 2}$ (cm ⁻¹)	0.001009	0.0007792
Group 2 (465 eV ~ 0.215 eV)	D (cm)	0.4744	0.6735
	Σ_a (cm ⁻¹)	0.2362	0.02631
	$\Sigma_s^{2 \rightarrow 2}$ (cm ⁻¹)	0.5933	0.5728
	$\nu \Sigma_f$ (cm ⁻¹)	0	0.02294

TABLE 2.4.4-2 Cylindrical geometry for test calculations

Region	Outer radius (cm)
Control rod	4
Fuel	44
Blanket	76
Reflector	85

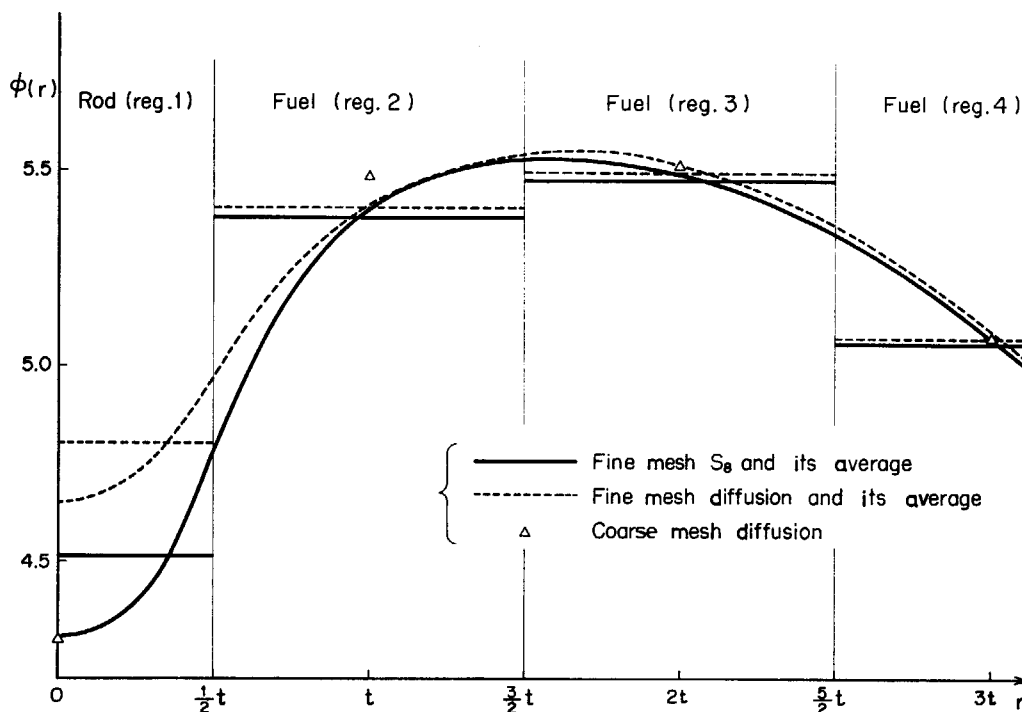


Fig. 2.4.4-2 Behavior of group 1 fluxes by various conventional schemes.

TABLE 2.4.4-3 Mean flux for each region normalized as $\int_{\text{Reactor}} \sum_n (\nu \Sigma_f)^n \phi^n dV = 1$

		$\bar{\phi}_1$	$\bar{\phi}_2$
Group 1	S_8 (fine mesh)	4.512	5.380
	Conventional diffusion (coarse mesh)	4.301	5.482
	Conventional diffusion (fine mesh)	4.802	5.404
	Corrected diffusion (coarse mesh)	4.480	5.450
Group 2	S_8 (fine mesh)	0.05044	0.1335
	Conventional diffusion (coarse mesh)	0.03507	0.1484
	Conventional diffusion (fine mesh)	0.05280	0.1337
	Corrected diffusion (coarse mesh)	0.04917	0.1377

Some trial calculations to examine this circumstance more in detail were made in cylindrical geometry (see TABLES 2.4.4-1 and 2.4.4-2), with an absorber set in the central zone. Figure 2.4.4-2 and TABLE 2.4.4-3 show that the value of $\bar{\phi}_1$ turns out to be excessively small when derived by coarse mesh diffusion, while the corresponding value by fine mesh diffusion is somewhat larger than obtained from the fine mesh transport S_8 calculation¹⁵⁾. As for $\bar{\phi}_2$, the estimate by coarse mesh diffusion is rather large, while an acceptable close approximation is obtained with the fine mesh diffusion equation by using the volume weight $2\pi r$ to integrate $\phi(r)$ to obtain $\bar{\phi}_2$.

From the discussions given above, it may be concluded that the errors in the coarse mesh diffusion scheme originates from two causes:

- (1) In the control rod, the value of ϕ at the center differs from the average $\bar{\phi}_1$.
- (2) It is not adequate to use $\text{grad } \phi = (\bar{\phi}_2 - \bar{\phi}_1)/t$ at S where the curvature of the spatial flux distribution changes its sign in the direction normal to S.

The above difficulty can be resolved if the accurate values of the flux $\rho(x)$ and the current in a reference cell can be obtained by some means, and if the relation between the net current and the average flux to be used in the coarse mesh diffusion scheme can be derived. This would be implemented by improving the expression of J as

$$J = \tau(\bar{\phi}_2 - \bar{\phi}_1),$$

$$\tau = \hat{J} / (\bar{\rho}_2 - \bar{\rho}_1),$$

where \hat{J} means the accurate net current through the unit area of the interface of control rod and fuel in the reference cell, and $\bar{\rho}_n$ means the average of $\rho(x)$ in each region of thickness t .

The factor τ would be given numerically for each group and for individual surfaces of the rod. Moreover, τ could be incorporated into the data before the 3-dimensional criticality calculation based on the coarse mesh diffusion model, so that the accuracy of flux would be easily improved without increasing the computer time.

2.4.4.1 Calculation of Correction Factor

(1) Functional of $\rho(x)$

In the case of hexagonal geometry, each side of the lattice is plane and it is considered that the value of τ is not very much influenced by the flux distribution far from this plane. Hence an appropriate value of τ can be calculated for every group in a simple slab lattice consisting of two regions arranged periodically and having the same compositions on both sides of S. Let us consider an infinite periodical lattice of slabs as illustrated in Fig. 2.4.4-3, where $x=0$ and $x=b$ are planes of symmetry, so that only the region $(0, b)$ needs to be considered. We let $a=t/2$, $b=2t$. While there is no inherent necessity to let $b=2t$, it has been found that the variation of b exceeding $2t$ does not influence the resulting value of τ to any significant extent. The values of the transport solution $\rho_1(x)$ and $\rho_2(x)$ are assumed for the regions 1 $(0, a)$ and 2 (a, b) , respectively, with the boundary conditions:

$$\begin{aligned} \rho_1(x) &= 1, \quad \frac{d}{dx}\rho_1(x) = 0 && \text{at } x=0, \\ \rho_1(x) &= \rho_2(x) && \text{at } x=a, \\ \frac{d}{dx}\rho_2(x) &= 0 && \text{at } x=b. \end{aligned}$$

When the source distribution is given, $\rho_1(x)$ and $\rho_2(x)$ must be renormalized so as to preserve the neutron balance, which requires the total source to be equal to the total absorption plus removal in the interval $(0, b)$. For the normalization factor we introduce the value f^{-1} (f being given in §2.4.4.1 (3) later). Letting κ be the infinite multiplication factor for this cell $(0, b)$, the source term for the i -th group is given by

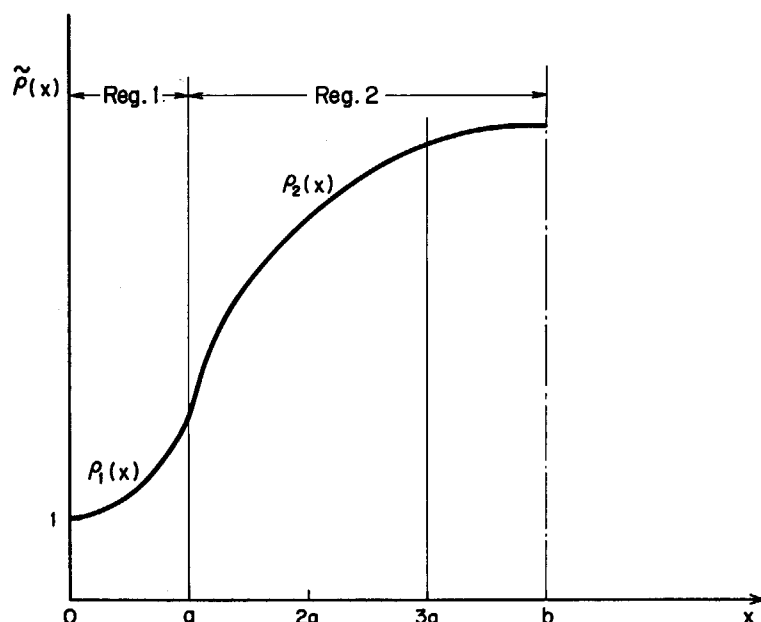


Fig. 2.4.4-3 Infinite slab lattice of periodical two regions and trial function for the neutron flux.

$$S^i(x) = \chi^i \kappa^{-1} \sum_j (\nu \Sigma_t)^j(x) \rho^j(x) / f^i + \sum_{j=1}^{i-1} \Sigma_s^{j \rightarrow i}(x) \rho^j(x) / f^i,$$

where the cross sections $(\nu \Sigma_t)^j$ and $\Sigma_s^{j \rightarrow i}$ are constant in each region. In what follows, we will denote the cross section for scattering into the self group by the abbreviation Σ_s^i or Σ_s instead of $\Sigma_s^{i \rightarrow i}$.

The integral transport equation for a slab system is written as

$$\rho(x) = 1/2 \int_{-\infty}^{\infty} E_1(|\lambda - \lambda'|) [\Sigma_s(x') \rho(x') + f S(x')] dx', \quad (2.4.4-2)$$

where $\lambda = \lambda(x) = \int_0^x \Sigma_t(y) dy$, $\lambda' = \lambda(x')$ and $\lambda_0 = a \Sigma_{t1} + (b-a) \Sigma_{t2}$ is the optical thickness of $(0, b)$, and the group index i has been omitted. Noting the periodicity and symmetry of the functions contained in the brackets, Eq. (2.4.4-2) becomes¹⁶⁾

$$\rho(x) = \int_0^b T(x' \rightarrow x) [\Sigma_s(x') \rho(x') + f S(x')] dx', \quad (2.4.4-3)$$

where $T(x' \rightarrow x) = 1/2 \sum_{n=0}^{\infty} \{E_1[2n\lambda_0 + |\lambda - \lambda'|] + E_1[2(n+1)\lambda_0 - \lambda - \lambda'] + E_1[2n\lambda_0 + \lambda + \lambda'] + E_1[2(n+1)\lambda_0 - |\lambda - \lambda'|]\}$.

Equation (2.4.4-3) is solved by using a source iteration technique. Since $S(x')$ is a known function in each iteration step,

$$q(x) = f \int_0^b T(x' \rightarrow x) S(x') dx',$$

so that Eq. (2.4.4-3) can be written as

$$\rho(x) = \int_0^b T(x' \rightarrow x) \Sigma_s(x') \rho(x') dx' + q(x).$$

The homogeneous equation without the term $q(x)$ is

$$\rho(x) = \gamma_0 \int_0^b T(x' \rightarrow x) \Sigma_s(x') \rho(x') dx',$$

where γ_0 is the lowest eigenvalue and $\gamma_0 > 1$. From the adjoint equation

$$\rho^+(x) = \gamma_0 \int_0^b T(x \rightarrow x') \Sigma_s(x) \rho^+(x') dx',$$

$\rho^+(x) = \Sigma_s(x) \rho(x)$ is easily obtained since $T(x \rightarrow x') = T(x' \rightarrow x)$.

When $\rho(x)$ is replaced by a trial function $\tilde{\rho}(x)$, a functional of $\tilde{\rho}(x)$ is defined by

$$I(\tilde{\rho}) = \int_0^b \tilde{\rho}^+(x) \left[\int_0^b T(x' \rightarrow x) \Sigma_s(x') \tilde{\rho}(x') dx' - \tilde{\rho}(x) + 2q(x) \right] dx. \quad (2.4.4-4)$$

If $\tilde{\rho}(x) \equiv \rho(x)$, the functional has a stationary value $\int_0^b \tilde{\rho}^+(x) q(x) dx$, and this is the maximum of $I(\tilde{\rho})$ when $\gamma_0 > 1$. It is proved¹⁷⁾ that

$$\begin{aligned} I(\tilde{\rho}) &\leq \int_0^b \rho^+(x) q(x) dx + (1/\gamma_0 - 1) \int_0^b \Sigma_s(x) [\tilde{\rho}(x) - \rho(x)]^2 dx \\ &\leq \int_0^b \rho^+(x) q(x) dx = I(\rho), \end{aligned}$$

and $I(\tilde{\rho})$ gives a good approximation to $I(\rho)$ even for relatively poor trial functions.

Equation (2.4.4-4) is rewritten, again using the $S(x)$:

$$I(\tilde{\rho}) = \int_0^b \Sigma_s(x) \tilde{\rho}(x) \left[\int_0^b T(x' \rightarrow x) \{ \Sigma_s(x') \tilde{\rho}(x') + 2f S(x') \} dx' - \tilde{\rho}(x) \right] dx,$$

For numerical calculation, the region $(0, a)$ is divided into N_1 intervals of equal width, and the region (a, b) into N_2 intervals of equal width ($N_1 + N_2 = N$). The mesh intervals are numbered 1, 2, ..., N from the side of $x=0$. The value of x at the middle point of the n -th mesh

interval is denoted by x_n , and the value $\bar{\rho}_n = \bar{\rho}(x_n)$ is treated as the mean value of $\bar{\rho}(x)$ in the n -th interval. Defining

$$T_{nk} = \langle T(x_k \rightarrow x_n) \rangle = \frac{1}{\Delta x_n} \int_{\Delta x_n} dx \cdot \frac{1}{\Delta x_k} \int_{\Delta x_k} dx' T(x' \rightarrow x),$$

we obtain the equation for the numerical calculation as follows:

$$I(\bar{\rho}) \cong \sum_{n=1}^N \Delta x_n \Sigma_{sn} \bar{\rho}_n \left[\sum_{k=1}^N \Delta x_k T_{nk} \{ \Sigma_{sk} \bar{\rho}_k + 2fS_k \} - \bar{\rho}_n \right]. \quad (2.4.4-5)$$

(2) Trial function

A simple trial function written as

$$\bar{\rho}(x) = \begin{cases} \rho_1(x) = 1 + A_1 x^2 + A_2 x^4 & (0 \leq x \leq a) \\ \rho_2(x) = C - B_1(b-x)^2 - B_2(b-x)^4 & (a \leq x \leq b), \end{cases}$$

is used. From the boundary condition at $x=a$, we have

$$C = 1 + \alpha A_1 + \beta A_2 + \gamma B_1 + \delta B_2$$

where $\alpha = a^2$, $\beta = a^4$, $\gamma = (b-a)^2$ and $\delta = (b-a)^4$. Hence, if only four coefficients are determined, $\bar{\rho}(x)$ is given by

$$\begin{cases} \rho_1(x) = 1 + A_1 x^2 + A_2 x^4 \\ \rho_2(x) = (1 + \alpha A_1 + \beta A_2 + \gamma B_1 + \delta B_2) - B_1(b-x)^2 - B_2(b-x)^4. \end{cases}$$

In what follows, the notations Σ_{sn} are replaced by Σ_{s1} or Σ_{s2} , with the numeral suffix representing the region number, and the symbols $n \in I$ or $k \in II$ are used to mean that mesh intervals n or k belong to region 1 or 2, respectively. From Eq. (2.4.4-5), we can write

$$\begin{aligned} I(\bar{\rho}) = & \Sigma_{s1} \sum_{n \in I} \Delta x_n \rho_1(x_n) \left[\sum_{k \in I} \Delta x_k T_{nk} \{ \Sigma_{s1} \rho_1(x_k) + 2fS_k \} \right. \\ & \left. + \sum_{k \in II} \Delta x_k T_{nk} \{ \Sigma_{s2} \rho_2(x_k) + 2fS_k \} - \rho_1(x_n) \right] \\ & + \Sigma_{s2} \sum_{n \in II} \Delta x_n \rho_2(x_n) \left[\sum_{k \in I} \Delta x_k T_{nk} \{ \Sigma_{s1} \rho_1(x_k) + 2fS_k \} \right. \\ & \left. + \sum_{k \in II} \Delta x_k T_{nk} \{ \Sigma_{s2} \rho_2(x_k) + 2fS_k \} - \rho_2(x_n) \right]. \end{aligned} \quad (2.4.4-6)$$

The defining

$$\left. \begin{aligned} k_{1n} &= \sum_{k \in I} \Delta x_k T_{nk}, & k_{2n} &= \sum_{k \in II} \Delta x_k T_{nk} \\ l_{1n} &= \sum_{k \in I} \Delta x_k T_{nk} x_k^2, & l_{2n} &= \sum_{k \in II} \Delta x_k T_{nk} (b-x)^2 \\ m_{1n} &= \sum_{k \in I} \Delta x_k T_{nk} x_k^4, & m_{2n} &= \sum_{k \in II} \Delta x_k T_{nk} (b-x)^4 \\ n_{1n} &= \sum_{k \in I} \Delta x_k T_{nk} S_k, & n_{2n} &= \sum_{k \in II} \Delta x_k T_{nk} S_k \end{aligned} \right\}, \quad (2.4.4-7)$$

Eq. (2.4.4-6) becomes

$$\begin{aligned} I(\bar{\rho}) = & \Sigma_{s1} \sum_{n \in I} \Delta x_n \{ 1 + A_1 x_n^2 + A_2 x_n^4 \} [\Sigma_{s1} \{ k_{1n} + A_1 l_{1n} + A_2 m_{1n} \} + 2f n_{1n} \\ & + \Sigma_{s2} \{ (1 + \alpha A_1 + \beta A_2 + \gamma B_1 + \delta B_2) k_{2n} - B_1 l_{2n} - B_2 m_{2n} \} \\ & + 2f n_{2n} - \{ 1 + A_1 x_n^2 + A_2 x_n^4 \}] \\ & + \Sigma_{s2} \sum_{n \in II} \Delta x_n \{ (1 + \alpha A_1 + \beta A_2 + \gamma B_1 + \delta B_2) - B_1(b-x_n)^2 - B_2(b-x_n)^4 \} \\ & \cdot [\Sigma_{s1} \{ k_{1n} + A_1 l_{1n} + A_2 m_{1n} \} + 2f n_{1n} \\ & + \Sigma_{s2} \{ (1 + \alpha A_1 + \beta A_2 + \gamma B_1 + \delta B_2) k_{2n} - B_1 l_{2n} - B_2 m_{2n} \} \\ & + 2f n_{2n} - \{ (1 + \alpha A_1 + \beta A_2 + \gamma B_1 + \delta B_2) - B_1(b-x_n)^2 - B_2(b-x_n)^4 \}]. \end{aligned}$$

The coefficients, A_1 , A_2 , B_1 and B_2 are determined by solving the simultaneous linear equations

$$\frac{\partial}{\partial A_1} I(\bar{\rho}) = 0, \quad \frac{\partial}{\partial A_2} I(\bar{\rho}) = 0, \quad \frac{\partial}{\partial B_1} I(\bar{\rho}) = 0 \quad \text{and} \quad \frac{\partial}{\partial B_2} I(\bar{\rho}) = 0,$$

but the coefficients obtained thereby are expressed in linear functions of f , and so is C .

(3) Neutron balance

Neutron balance is preserved in each group i , so that

$$\int_0^b \{\Sigma_i^i(x) - \Sigma_{s \rightarrow i}^i(x)\} \bar{\rho}^i(x) dx = f^i \int_0^b S^i(x) dx.$$

Since the coefficients obtained in §2.4.4.1 (2) are expressed in linear functions of f , $\bar{\rho}^i(x)$ also is in a form like $\xi_1^i(x) + f^i \xi_2^i(x)$. Then, the above neutron balance equation is reduced to

$$Q_1^i + Q_2^i f^i = f^i S^i,$$

from which f^i is determined as $Q_1^i / (S^i - Q_2^i)$.

(4) Source iteration

The initial flux guess may be $\phi^i(x) \equiv 1$, and in the succeeding iterations, $\phi^i(x)$ is given by

$$\phi^i(x) = \bar{\rho}^i(x) / f^i,$$

and

$$G(x) = \sum_j (\nu \Sigma_f)^j(x) \phi^j(x),$$

$$\kappa = \int_0^b G(x) dx,$$

$$S^i(x) = \chi^i \kappa^{-1} G(x) + \sum_{j=1}^{i-1} \Sigma_{s1}^{j \rightarrow i}(x) \phi^j(x).$$

On each iteration step, only the values of n_{1n} and n_{2n} are altered in Eq. (2.4.4-7), from which A , B and C are recalculated. The criterion for convergence is that the relative error of κ reduces to a value below 10^{-4} between two successive iterations, this being attained generally after a few iterations.

(5) τ calculation

Considering again the neutron balance in the region of absorber $(0, a)$, the value of τ^i is now obtained as follows:

$$\bar{\rho}_1^i = 1/a \int_0^a \rho_1^i(x) dx,$$

$$\bar{\rho}_2^i = 1/2a \int_a^{3a} \rho_2^i(x) dx,$$

$$\bar{f}^i = (\Sigma_{t1}^i - \Sigma_{s1}^{i \rightarrow i}) \int_0^a \rho_1^i(x) dx - f^i \sum_{j=1}^{i-1} \Sigma_{s1}^{j \rightarrow i} \int_0^a \rho_1^j(x) dx / f^j,$$

$$\tau^i = \bar{f}^i / (\bar{\rho}_2^i - \bar{\rho}_1^i).$$

2.4.4.2 Test Calculation in Cylindrical Geometry

As a simple test on the effect produced by the adoption of τ in the coarse mesh diffusion scheme, axially infinite cylindrical systems were utilized in the same way as in the test calculation shown in Fig. 2.4.4-2. There it was confirmed that, by incorporating τ in the coarse mesh diffusion scheme, $\bar{\phi}_1$ and $\bar{\phi}_2$ acquire values giving a better approximation in each region of thickness t . For this test calculation, Δx_n in the procedure of §2.4.4.1 was replaced by $2\pi r_n \Delta r_n$, and $\int dx$ by $\int 2\pi r dr$. Then, T_{nk} was calculated by the second order Bickley function $K_{i2}(\lambda) = \int_0^{\pi/2} e^{-\lambda \sec \theta} \cos \theta d\theta$ in an annular cell consisting of N concentric regions with the reflective boundary condition at $r=b$, similarly to the treatment by THERMOS code¹⁶⁾. The results are given in TABLE 2.4.4-3 together with those of the calculations described in the former part of §2.4.4. The errors of the mean fluxes corrected by the present method are about 1% in the group 1 and about 3% in the group 2. This means that the error is reduced by a factor of 12 or more in the control rod through this method of correction for the coarse mesh diffusion scheme which will be the most practical approach to three dimensional problems.

Figures 2.4.4-4 and 2.4.4-5 show the results of similar examination for the cases with

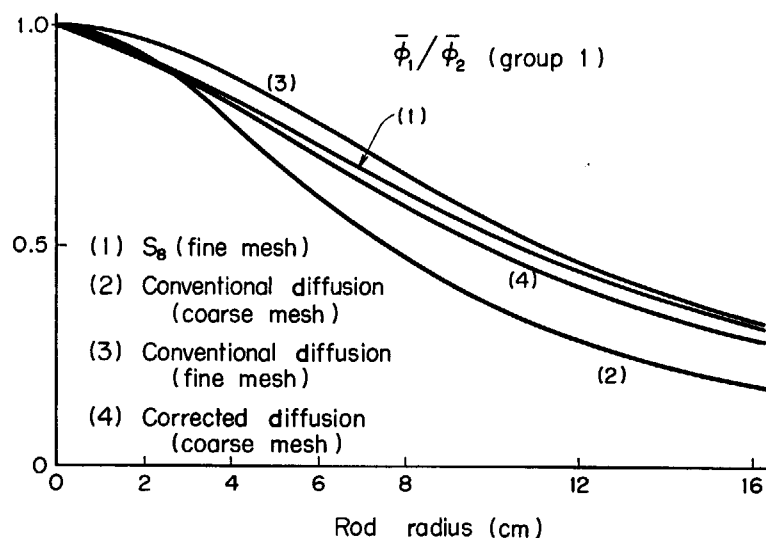


Fig. 2.4.4-4 The flux ratio $\bar{\phi}_1/\bar{\phi}_2$ vs. control rod radius for group 1 (coarse mesh size=rod radius \times 2).

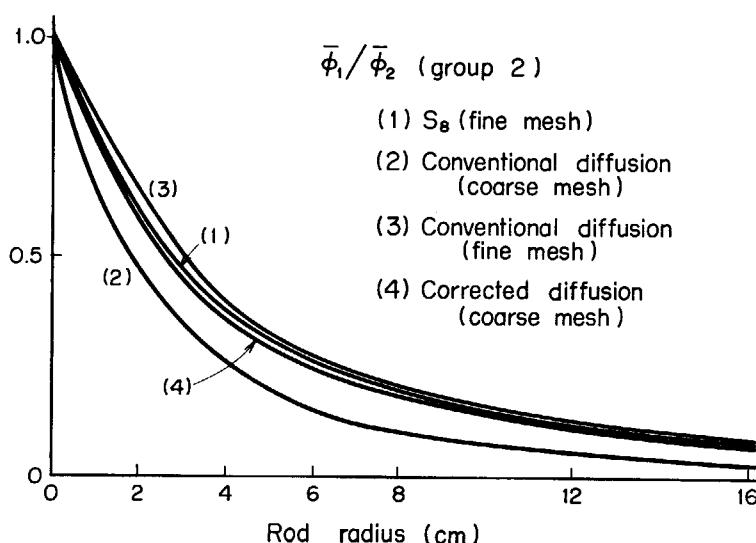


Fig. 2.4.4-5 The flux ratio $\bar{\phi}_1/\bar{\phi}_2$ vs. control rod radius for group 2 (coarse mesh size=rod radius \times 2).

different values of t , the rod radius and the mesh size being varied simultaneously. The applicability of this method is thus confirmed over a wide range of t .

The method has now been incorporated into the HONEYCOMB code. The value of k_{eff} is reduced by about 0.74% through the adoption of τ for an experimental fast reactor with four control rods fully inserted and two partially in depth. It is thus concluded that use of this correction method provides appreciably better accuracy in the predicted value of k_{eff} or of the critical insertion depth of the control rods, as well as of the control rod worth. Further examinations are made in §2.7.2, for 2-dimensional hexagonal and triangular geometries, about the effect of mesh sizes on the accuracy of criticality calculation. It is confirmed there that this correction method is very useful for more general situations where several parameters are varied over their practical ranges.

2.4.5 Criticality Adjustment by Insertion Depth of Control Rods

In HONEYCOMB, it is able to search the critical insertion depth of control rods so that the value of k_{eff} can always have the value equal to K_c (which is ordinarily 1) as a result of the criticality calculation described in §2.4.3. The rods, which are controlled their insertion depths,

are assumed to have a common insertion depth Z_c in the z -coordinate (see Fig. 2.1.1-2). First, the criticality calculation is made by using the depth $z^{(1)}$, the initial guess of the value Z_c . Let l be the index of trial times of the search, then, $k_{\text{eff}} = k^{(l)}$ is obtained for the depth $z^{(l)}$.

Test for attainment of the criticality is made by

$$|k^{(l)} - K_c| < 10^{-5}.$$

When this condition is not fulfilled, the next guess for insertion depth is obtained as follows:

(1) in case of $l=2$,

$$z^{(2)} = z^{(1)} \{1 - 10(K_c - k^{(1)})\},$$

(2) in case of $l=3$,

$$z^{(3)} = z^{(2)} + (z^{(2)} - z^{(1)})(K_c - k^{(2)})/(k^{(2)} - k^{(1)}),$$

(3) in case of $l \geq 4$, parameters a , b and c is determined by solving bilinear equations:

$$\begin{cases} (z^{(l-3)} - a)(k^{(l-3)} - b) = c, \\ (z^{(l-2)} - a)(k^{(l-2)} - b) = c, \\ (z^{(l-1)} - a)(k^{(l-1)} - b) = c, \end{cases}$$

and

$$z^{(l)} = a + c/(K_c - b).$$

For $l \geq 2$, the guess $z^{(l)}$ usually does not coincide with any interface of z -mesh intervals, because z -mesh structure has been fixed from the beginning. So, we set one more temporary mesh point in the z -interval in which $z^{(l)}$ happens to fall, and the interval is divided into two intervals at $z^{(l)}$. The actual 3-dimensional calculation is thus performed by using $(M+1)$ mesh intervals in z -direction. The resulting value of ϕ_{jik}^n is obtained by averaging the two values for the intervals on both sides of $z^{(l)}$, with weights of the mesh sizes. In addition, the technique for saving the computation time is engaged in the same way as in FURNACE code.¹⁸⁾

2.4.6 Three-dimensional Distribution of Adjoint Neutron Flux

HONEYCOMB is possible to prepare the adjoint neutron flux for use in perturbation theory codes. The adjoint equation written as

$$-D^n \nabla^2 \phi^{*n} + \Sigma_T^n \phi^{*n} = \lambda^* (\nu \Sigma_f)^n \sum_l \chi^l \phi^{*l} + \sum_{l=n+1}^{\text{NMAX}} \Sigma_s^{n \rightarrow l} \phi^{*l}$$

is solved in the same way as described through §2.4.1 to §2.4.3. The $(B_z^2)_l^n$ in §2.4.1 and τ^n in §2.4.4 are used commonly. The eigenvalue λ^* is defined as

$$\lambda^* = \frac{\int dV \sum_n \left[-D^n \nabla^2 \phi^{*n} + \left(\Sigma_T^n - \sum_{l=1}^{n-1} \Sigma_s^{l \rightarrow n} \right) \phi^{*n} \right]}{\int dV \left[\sum_n (\nu \Sigma_f)^n \right] \left[\sum_l \chi^l \phi^{*l} \right]}.$$

When convergence criteria are fulfilled as a result of the iterative treatment, λ^* becomes equal to λ , in due courses of r - z , hexagonal and hexagonal- z calculations. Three-dimensional approximate distribution is also defined as

$$\hat{\phi}_{jik}^{*n} = \phi_{ji}^{*n} \phi_{lk}^{*n} / \sum_n \sum_{jik} \Delta V_{jik} \chi^n \phi_{ji}^{*n} \phi_{lk}^{*n},$$

where $(j, i) \in l$, $\Delta V_{jik} = (\sqrt{3}/2) t^2 \Delta z_k$, and

$$\sum_n \sum_{jik} \Delta V_{jik} \chi^n \hat{\phi}_{jik}^{*n} = 1.$$

The normalization factor for the 3-dimensional hexagonal- z adjoint flux in the inner regions up to the 8-th ring is

$$TS^* = \sum_n \sum_k \sum_{l=1}^8 \sum_{(j,i) \in l} \Delta V_{jik} \chi^n \hat{\phi}_{jik}^{*n},$$

and the boundary condition at each radial surface element for each group is given by

$$a_B^* = \frac{1}{\sqrt{3}} \Delta z_k D_{l=8} (\hat{\phi}_{l=8}^* - \hat{\phi}_{l=9}^*) / \hat{\phi}_{l=8}^*.$$

As described previously in §2.4.3, the 3-dimensional distribution of adjoint neutron flux is made up by ϕ_{jik}^{*n} for the inner 8 zones with supplement of $\hat{\phi}_{jik}^{*n}$ for the outer 3 zones.

2.5 Three-dimensional Power Distribution

It has been estimated^{7),12)} that the heat deposition by secondary gamma rays produced by reactions between neutrons and nuclei will occupy about 10% of the total heat generation for experimental FBR, and for blanket region more than 30% of the integrated heat generation rate in the region. In the present code system, the predicted distribution of the heat generation rate is to be evaluated accurately, since the distribution is the fundamental input information to the subsystems FDCAL-3 and SMART. By these reasons, HONEYCOMB has been made capable of taking account of the γ -ray heating though it is designed only for the core region of Figs. 2.1.1-1 and 2.1.1-2.

In §2.5.1, the 3-dimensional distributions of γ -ray flux and the heat generation rate are calculated using the source distribution due to $(n, \text{fission } \gamma)$, (n, γ) and $(n, n'\gamma)$ reactions. Next, in §2.5.2, the total heat generation rate, containing fission energy yield, is obtained as 3-dimensional distribution and is normalized to the total power generation rate of the reactor.

The detailed power distribution in each fuel and blanket assembly is required by FATEC and SMART. Therefore it is necessary to estimate the power generation rate for the individual fuel pins in every axial mesh interval. The section 2.5.3 is devoted to this purpose. The 1-group 2-dimensional flux distribution is obtained in a hexagonal region by engaging a method of boundary value problem based on the potential theory. The coarse mesh fluxes in §2.4 provide the boundary condition, and the coarse mesh power is used as the normalization factor to the fine distribution in each volume segment. This new method has made it practical to obtain the extremely fine distribution of power generation rate in a short computation time, which was a difficult problem in the past.

2.5.1 Three-dimensional Distribution of Heat Deposition by Neutron-induced γ -ray

The HONEYCOMB subsystem deals with only the regions of hexagonal assemblies where the heat generation by fission is dominant. This is the reason why it is not necessary to demand so much accuracy as in the shielding calculation. We adopt here a 3-group 3-dimensional diffusion model for determining γ -ray flux distribution. In the 1-dimensional cylindrical geometry, a comparison was made between diffusion and S_n transport solutions for the γ -ray flux. A satisfactory agreement was observed between the solutions in the above two models for the fuel and blanket regions. In the reflector or sleeve regions, the amount of γ -ray flux becomes 10^{-3} or 10^{-4} times of that in the core center. In the calculation of heat generation rate by γ -rays, the resulting power distribution is added to the dominant fission power distribution, and after that, the total power distribution is normalized to the thermal power output (P) of the reactor. So, the error due to the γ -ray calculation is expected to be reduced.

2.5.1.1 Source Distribution of Photons

Here, we consider only three kinds of reactions to be important as the source of γ -ray, namely, $(n, \text{fission } \gamma)$, (n, γ) and $(n, n'\gamma)$ reactions. Since the 3-dimensional distributions of 6-group neutron fluxes are already known at the step described in the previous section (§2.4), the source distribution is easily obtained as

$$S_{ijk}^g = \sum_n \sum_x S_x^{n \rightarrow g} \Sigma_{xjik}^n \phi_{jik}^n = \sum_n S_{jik}^{n \rightarrow g} \phi_{jik}^n,$$

where x , n and g stand for the kind of reaction, groups of neutron energy and of photon energy, respectively, and $S_x^{n \rightarrow g}$ or $S^{n \rightarrow g}$ has already been given in §2.2.4 or §2.2.5. As to the reaction

x, fission has the most dominant contribution to the resulting γ -ray dose as compared with other two reactions of absorption and inelastic scattering. The γ -ray energy range is divided into three groups of 10~3 MeV, 3~0.5 MeV and 500~10 keV.

2.5.1.2 Cross Sections for Photon Transport Calculations

By the use of the code GAMLEG¹⁹⁾, the following 15-group cross sections are calculated for each nuclide m :

$$\begin{aligned}\sigma_t^{mi} &: \text{total cross section,} \\ \sigma_{s1}^{m,i \rightarrow i} &: P_1 \text{ component of scattering cross section into self group,} \\ \sigma_{s0}^{m,i \rightarrow j} &: P_0 \text{ component of scattering cross section from } i\text{-th group into } j\text{-th group} \\ &\quad (j=i, i+1, \dots, 15),\end{aligned}$$

and for each mixture, the following macroscopic cross sections are obtained:

$$\begin{aligned}\Sigma_{tr}^i &= \sum_m N^m (\sigma_t^{mi} - \sigma_{s1}^{m,i \rightarrow i}), \\ \Sigma_t^i &= \sum_m N^m \sigma_t^{mi}, \\ \Sigma_s^{i \rightarrow j} &= \sum_m N^m \sigma_{s0}^{m,i \rightarrow j}, \\ H^i &= \bar{E}^i \Sigma_t^i - \sum_{j=i}^{15} \bar{E}^j \Sigma_s^{i \rightarrow j},\end{aligned}$$

where H^i is the heat generation constant. We assume that all energy of a photon is converted to heat at the place where the photon is absorbed by an atom. The \bar{E}^i is the mean energy of the i -th group in units of MW·sec (1 MeV = 1.60206×10^{-19} MW·sec). Therefore, the dimension of H^i is MW·sec/cm.

Next, the 15-group structure (i, j) is collapsed into 3-group structure (g, h). Using the photon number spectrum S_t^i given in TABLE 2.5.1-1, the weighting spectrum is assumed as

$$\varphi^i = \left(S_t^i + \sum_{j=1}^{i-1} \Sigma_s^{j \rightarrow i} \varphi^j \right) / (\Sigma_t^i - \Sigma_s^{i \rightarrow i}),$$

where S_c^i and S_{in}^i are neglected because S_t^i is much larger than them. The φ^i is derived from the transport equation with the source emitted by one fission,

$$\mu \nabla \varphi^i + (\Sigma_t^i - \Sigma_s^{i \rightarrow i}) \varphi^i = S_t^i + \sum_{j=1}^{i-1} \Sigma_s^{j \rightarrow i} \varphi^j$$

neglecting the first term on the left hand side. The Σ_t^i is very large in case of photon-atom reaction as compared with neutron-nucleus reaction. In the same way as in §2.2.4, we have

TABLE 2.5.1-1 Fifteen group structure for photon transport cross sections

Group		E_U (MeV)	E_L (MeV)	S_t^{235}
1	1	10	9	0.00018
	2	9	8	0.00020
	3	8	7	0.00023
	4	7	6	0.00493
	5	6	5	0.03067
	6	5	4	0.1144
	7	4	3.5	0.1383
	8	3.5	3	0.2089
2	9	3	2.5	0.3905
	10	2.5	2	0.7053
	11	2	1.5	1.2159
	12	1.5	1	2.2415
	13	1	0.75	1.9588
	14	0.75	0.5	3.0120
	15	0.5	0.01	8.9037
Total				18.9255

$$\begin{aligned}
\varphi^g &= \sum_{i \in g} \varphi^i, \\
D^g &= \sum_{i \in g} (\varphi^i / 3 \Sigma_{tr}^i) / \varphi^g, \\
\Sigma_{t^g} &= \sum_{i \in g} \Sigma_t^i \varphi^i / \varphi^g, \\
\Sigma_{s^g \rightarrow h} &= \sum_{i \in g} \left(\sum_{j \in h} \Sigma_s^{i \rightarrow j} \right) \varphi^i / \varphi^g, \\
H^g &= \sum_{i \in g} H^i \varphi^i / \varphi^g, \\
\Sigma_{T^g} &= \Sigma_{t^g} - \Sigma_{s^g \rightarrow g} \quad (\text{total removal}).
\end{aligned}$$

2.5.1.3 Three-dimensional Distribution of γ -ray Flux

As mentioned above, the term $\mu V \varphi$ has a smaller value than $\Sigma_t \varphi$ (at most 10%), so it does not cause errors to a considerable extent even if the term is substituted by $-D \nabla^2 \varphi$ (diffusion model). This fact is confirmed by a comparison between the diffusion and S_8 transport models in a 15-group calculation for 1-dimensional cylindrical geometry. This is valid, however, only in the core matrix region where photon source distribution almost determines the flux distribution. Now use is made of the 3-group 3-dimensional diffusion equation :

$$-D^g \nabla^2 \psi^g + \Sigma_{T^g} \psi^g = S^g + \sum_{h=1}^{g-1} \Sigma_{s^h \rightarrow g} \psi^h,$$

for obtaining γ -ray flux ψ^g . In each group g , the problem is of fixed source distribution, if the equation is solved from the group 1 ($g=1$). So, it is easy to treat the whole region (up to eleventh zone) in 3-dimensional hexagonal-z mesh. For saving computation time, initial flux guess written as

$$\psi^g = \left(S^g + \sum_{h=1}^{g-1} \Sigma_{s^h \rightarrow g} \psi^h \right) / \Sigma_{T^g}$$

is used, and after each iteration step (a sweep about 3-dimensional mesh (j, i, k)), the renormalization is performed to ψ^g so that the amount of photons suffering absorption plus leakage becomes equal to the amount of source in the group g when they are integrated over the whole region.

2.5.1.4 Heat Generation Distribution by γ -rays

In each volume element, 3-dimensional distribution of heat generation rate by γ -rays is given by

$$\hat{P}_{\gamma jik} = \sum_g H_{jik}^g \psi_{jik}^g \quad (\text{MW/cm}^3).$$

The $\hat{P}_{\gamma jik}$ is, however, not yet normalized to the reactor total power P , in the same meaning that the flux ϕ^n used to obtain the photon source is not yet normalized to P (see the next section).

2.5.2 Total Power Generation in Each of 3-dimensional Volume Segments

The 3-dimensional power distribution can now be obtained by summing up the γ -ray power distribution $\hat{P}_{\gamma jik}$ in §2.5.1 and the fission power distribution, and by normalizing the total power to the reactor total power P given in input data. Let the word "fission power" mean the fission energy without including fission γ energy. Energy yield of 195.1 MeV by one fission²⁰⁾ contains the fission γ (prompt and delayed) energy of 14.3 MeV. So the "fission power" means an energy of 180.8 MeV in what follows. We neglect here the effect of accumulation of the delayed γ -rays, that is, the treatment is under the stationary condition. The conversion factor from fissions to energy, $C = 3.1 \times 10^{16}$ fissions/MW·sec, had been previously used without taking account of γ -ray transport like in §2.5.1. In our calculation, however, this factor is modified as

$$C_t = 3.1 \times 10^{16} \times \frac{195.1}{180.8} = 3.345 \times 10^{16} \text{ fissions/MW} \cdot \text{sec}.$$

Then, the factor for obtaining power normalized flux is defined by

$$F = P \left[\left(\sum_{jik} \sum_n \Sigma_{tjik}^n \phi_{jik}^n \Delta V_{jik} / C_t \right) + \sum_{jik} \hat{P}_{\gamma jik} \Delta V_{jik} \right]^{-1},$$

TABLE 2.5.2-1 Power generation rate from each region (MW)

	Fuel	Blanket	Control rods & reflectors	Total	Fuel (%)
Neutron	61.20	4.58	—	65.78	93.0
γ -ray	6.85	2.22	0.15	9.22	74.3
Total	68.05	6.80	0.15	75.00	90.7
γ -ray (%)	10.1	32.6	—	12.3	—

and the normalized γ -ray and fission power distributions are obtained like

$$P_{\gamma jik} = F \cdot \hat{P}_{\gamma jik} \times 10^6 \quad (\text{W/cm}^3),$$

$$P_{tjik} = F \cdot C_t^{-1} \sum_n \Sigma_{tjik}^n \phi_{jik}^n \times 10^6 \quad (\text{W/cm}^3).$$

The final result is then given by

$$P_{jik} = P_{tjik} + P_{\gamma jik} \quad (\text{W/cm}^3).$$

An example of output is given in TABLE 2.5.2-1, which shows the power generation rates (integrated over some regions) obtained for the problem given in §2.7.1, later.

2.5.3 Detailed Power Distribution for Each Fuel Pin²¹⁾

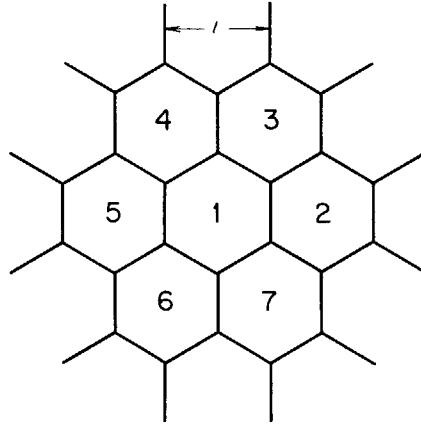
The detailed power distribution in the fuel assemblies, namely, the power generation rate for each fuel pin, is particularly important for predicting the temperature distribution in coolant channels as well as in fuel pins by the use of the FDCAL-3 code. On the other hand, the detailed power distribution is also required by the SMART subsystem for preparing the power peaking factor in each assembly.

The method for efficiently obtaining this detailed power distribution has been derived for HONEYCOMB without sacrificing accuracy obtainable by the conventional fine mesh difference scheme, which spends so much computation time even for one assembly that it is impractical to solve the problem for every assembly in the core. When the effective fission cross section averaged over the whole energy range does not vary in a coarse volume element to any significant extent, the power distribution in the volume segment is directly obtained by solving a 1-group diffusion equation with appropriate constants. Moreover, the total power in the segment (P_{jik}) is already given in the last section so that the present problem is 2-dimensional for finding the relative power distribution at each pin in the segment.

Thus the problem is reduced to a 1-group 2-dimensional boundary value problem for the hexagonal region of homogeneous medium. This problem can be solved using the 2-dimensional Green's function of infinite medium with superposing an image source distribution on the boundary.²²⁾ The present treatment is to obtain an integral representation as the solution of the Helmholtz equation in a 2-dimensional domain under any arbitrary boundary condition on a contour boundary, by using the 2-dimensional infinite medium Green's function, or its derivative on the boundary in the outward normal direction. This is so called the method of using the potential due to a single or a double layer. The density of the image source distribution is determined with the boundary condition by solving an integral equation, in which the kernel is expressed by the Green's function connecting the two points on the boundary. The discontinuity of the potential (or its derivative) on the boundary is taken into account in the integral equation. Then the neutron flux at any point inside the region is obtained from this density of the image source distribution on the boundary and by the kernel connecting the inside point to the boundary point.

2.5.3.1 Coefficients of 1-group Equation to be Solved

For each volume segment, the 6-group constants and neutron fluxes have already been ob-

Fig. 2.5.3-1 Hexagonal regions of pitch t .

tained in the previous sections (§2.2.4 and §2.4.3). The total power of the segment is also known (§2.5.2). Now, we use the 1-group diffusion model because the collapsing scheme usually conserves reaction rates, and so, also released power rate. In a hexagonal geometry of pitch t illustrated in Fig. 2.5.3-1, the group constants are collapsed into 1-group in region 1, and the fluxes in the regions 1~7 are summed up over groups. Then we obtain D , Σ_t , $\nu\Sigma_f$, Σ_s , Φ_n ($n=1, \dots, 7$) and DB_z^2 as 1-group data. The Σ_s may contain the effect of increase of neutrons by $(n, 2n)$ or $(n, 3n)$ reactions, and Φ_n means the 1-group flux averaged over the region n . The 1-group diffusion equation in the region 1 is now written as

$$\nabla^2\phi + B^2\phi = 0,$$

$$B^2 = (\nu\Sigma_f + \Sigma_s - \Sigma_t - DB_z^2)/D.$$

2.5.3.2 Boundary Condition

The boundary condition is approximately given around the region 1 as follows:

- (1) The flux value at each vertex of the hexagon is assumed to be equal to the arithmetic mean of the three Φ_n values around the vertex.
- (2) The flux value at the middle point of each side is assumed to be equal to the arithmetic mean of the two Φ_n values on both sides of the boundary.
- (3) From the flux values thus determined at the twelve points on the hexagonal contour, the boundary value of the flux is set up on this closed line as a linear interpolation of the two flux values on the end points of each half side, and is denoted as $b(s)$ where s is the distance measured along the contour from an origin on it.

Thus the problem has been reduced to a Dirichlet problem that the homogeneous equation $\nabla^2\phi + B^2\phi = 0$ should be solved with the inhomogeneous boundary condition $\phi(s) = b(s)$ on the hexagonal boundary.

2.5.3.3 Green's Function

The Green's function for the Helmholtz equation is given²³⁾ as the solution of

$$\nabla^2 G(\mathbf{r}, \mathbf{r}') + B^2 G(\mathbf{r}, \mathbf{r}') = -4\pi\delta(\mathbf{r} - \mathbf{r}').$$

The solution for 2-dimensional case is written as

$$G(\mathbf{r}, \mathbf{r}') = -\pi Y_0(BR),$$

where $Y_0(x)$ is the Bessel function of the second kind and $R = \|\mathbf{r} - \mathbf{r}'\|$ is the distance between the two points \mathbf{r} and \mathbf{r}' . In case of $B^2 < 0$, $G(\mathbf{r}, \mathbf{r}')$ should be written as

$$G(\mathbf{r}, \mathbf{r}') = 2K_0(\kappa R),$$

where $K_0(x)$ is the modified Bessel function of the second kind and $\kappa^2 = -B^2$.

2.5.3.4 General Solution

Generally the inhomogeneous equation:

$$\nabla^2 \phi(\mathbf{r}) + B^2 \phi(\mathbf{r}) = -4\pi \rho(\mathbf{r})$$

has the solution expressed as

$$\phi(\mathbf{r}) = \phi_\rho(\mathbf{r}) + \phi_g(\mathbf{r}) + \phi_f(\mathbf{r}),$$

where

$$\phi_\rho(\mathbf{r}) = \int_S \rho(\mathbf{r}') G(\mathbf{r}, \mathbf{r}') d\mathbf{r}',$$

$$\phi_g(\mathbf{r}) = -\frac{1}{4\pi} \int_C g(s) G(\mathbf{r}, \mathbf{s}) ds,$$

and

$$\phi_f(\mathbf{r}) = \frac{1}{4\pi} \int_C f(s) \nabla_\nu G(\mathbf{r}, \mathbf{s}) ds.$$

The ϕ_ρ is the potential due to a mass distribution with the density ρ on S . The ϕ_g is the potential due to a single layer distribution with density g on C , and the ϕ_f is the potential due to a double layer distribution of density f on C . The contour C , the boundary of the region S , must be composed of a finite number of arcs or straight line segments, each of which is congruent to a curve or line represented by continuous and continuously differentiable function, that is, C is a piecewise smooth contour.

2.5.3.5 Properties of Solution

Properties of ϕ_ρ , ϕ_g and ϕ_f are described in Ref. 22 (§IV. 1) in cases of the Laplace or Poisson equations. These properties are analogous to the case of Helmholtz equation because only the kernel $\log R$ is substituted by $Y_0(BR)$ or $K_0(\kappa R)$, which is represented by a sum of $\log R$ and regular function of R . We show here only conclusions. When ρ is a function satisfying the Hölder condition in S , ϕ_ρ is continuous and has uniformly continuous first derivatives and continuous second derivatives, and ϕ_ρ satisfies $\nabla^2 \phi_\rho + B^2 \phi_\rho = -4\pi \rho$ in S . When g is a function satisfying the Hölder condition on each smooth line segment of C , ϕ_g is continuous and its tangential derivative varies continuously as crossing over C . However, the normal derivative has a jump of magnitude g and its second derivatives are continuous in S , and ϕ_g satisfies $\nabla^2 \phi_g + B^2 \phi_g = 0$ in S . When f is a function satisfying the Hölder condition on each smooth line segment of C , ϕ_f has a jump of magnitude f across the contour C , and the derivative of ϕ_f in the direction normal to the contour varies continuously when \mathbf{r} crosses over C along the normal at \mathbf{s}_0 (Fig. 2.5.3-2).

However, the tangential derivative varies discontinuously in accordance with the jump of $\frac{\partial f}{\partial s_0}$, and its second order derivatives are continuous in S . In addition ϕ_f satisfies $\nabla^2 \phi_f + B^2 \phi_f = 0$ in S .

In our case of the homogeneous Helmholtz equation with $\rho=0$, the general solution is given by $\phi_g + \phi_f$. But ϕ_g or ϕ_f can be the solution by itself. Now, we show some properties of ϕ_g or

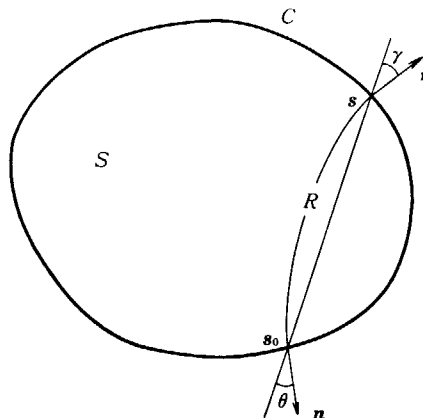


Fig. 2.5.3-2 The normals (\mathbf{n} and $\boldsymbol{\nu}$) and the chord ($\mathbf{s}-\mathbf{s}_0$) of the contour C .

ϕ_f when they approach to the boundary C from the inside. Notations are taken as shown in Fig. 2.5.3-2. As C is composed of "convex and smooth" or "linear" segments, that is, C is the piecewise smooth contour having no reentrant cavities, the angles between the normals and the chord:

$$\theta = \mathbf{n} \wedge (\mathbf{s}_0 - \mathbf{s}),$$

$$\gamma = \mathbf{v} \wedge (\mathbf{s} - \mathbf{s}_0)$$

always satisfy $\cos\theta \geq 0$ and $\cos\gamma \geq 0$.

For instance, in case of $B^2 > 0$ and $G(\mathbf{r}, \mathbf{s}) = -\pi Y_0(BR)$, we obtain

$$\lim_{\mathbf{r} \rightarrow \mathbf{s}_0} \phi_\theta(\mathbf{r}) = -\frac{1}{4} P \int_C g(s) Y_0(BR) ds, \quad (2.5.3-1)$$

$$\lim_{\mathbf{r} \rightarrow \mathbf{s}_0} \nabla_n \phi_\theta(\mathbf{r}) = \frac{1}{2} g(s_0) + \frac{B}{4} P \int_C g(s) \cos\theta Y_1(BR) ds, \quad (2.5.3-2)$$

$$\lim_{\mathbf{r} \rightarrow \mathbf{s}_0} \phi_f(\mathbf{r}) = -\frac{1}{2} f(s_0) + \frac{B}{4} P \int_C f(s) \cos\gamma Y_1(BR) ds, \quad (2.5.3-3)$$

where P means the Cauchy's principal value.

Equation (2.5.3-1) is evident because $Y_0(BR)$ has only logarithmic singularity. Equation (2.5.3-2) is proved using symbols shown in Figs. 2.5.3-3 and 2.5.3-4 as follows:

$$\begin{aligned} \lim_{\mathbf{r} \rightarrow \mathbf{s}_0} \nabla_n \phi_\theta(\mathbf{r}) &= \lim_{\varepsilon \rightarrow 0} \lim_{\mathbf{r} \rightarrow \mathbf{s}_0} \left[-\frac{1}{4} \int_{C_\varepsilon} g(s) \nabla_n Y_0(BR) ds - \frac{1}{4} \int_{C-C_\varepsilon} g(s) \nabla_n Y_0(BR) ds \right] \\ &= \lim_{\varepsilon \rightarrow 0} \lim_{\mathbf{r} \rightarrow \mathbf{s}_0} \left[-\frac{1}{4} g(s_0) \int_{C_\varepsilon} (-B \cos\theta) Y_1(BR) ds \right] - \frac{1}{4} P \int_C g(s) (-B \cos\theta) Y_1(BR) ds, \end{aligned}$$

where $\theta = \mathbf{n} \wedge (\mathbf{r} - \mathbf{s})$ and $\cos\theta < 0$ in the first term. So, it is now sufficient to show that the first term

$$\frac{B}{4} g(s_0) \lim_{\varepsilon \rightarrow 0} \lim_{\mathbf{r} \rightarrow \mathbf{s}_0} \int_{C_\varepsilon} \cos\theta Y_1(BR) ds$$

becomes $\frac{1}{2} g(s_0)$. The coordinates are taken as

$$\mathbf{n} \parallel \mathbf{x}, \mathbf{r} = (x, y), \mathbf{s}_0 = (\xi_0, \eta_0) \text{ and } \mathbf{s} = (\xi, \eta)$$

and when $R \rightarrow 0$, $Y_1(BR) \rightarrow -\frac{2}{\pi} \cdot \frac{1}{BR}$ and C_ε is regarded as a straight line. Then,

$$\begin{aligned} &\frac{B}{4} g(s_0) \lim_{\varepsilon \rightarrow 0} \lim_{\mathbf{r} \rightarrow \mathbf{s}_0} \int_{\eta_0 - \varepsilon}^{\eta_0 + \varepsilon} \left(-\frac{R_0}{R} \right) \left(-\frac{2}{\pi} \cdot \frac{1}{BR} \right) d\eta \\ &= \frac{1}{\pi} g(s_0) \lim_{\varepsilon \rightarrow 0} \lim_{R_0 \rightarrow 0} \int_0^\varepsilon \frac{R_0}{R_0^2 + s^2} ds \\ &= \frac{1}{\pi} g(s_0) \lim_{\varepsilon \rightarrow 0} \lim_{R_0 \rightarrow 0} \int_0^{\varepsilon/R_0} \frac{dt}{1+t^2} = \frac{1}{\pi} g(s_0) \int_0^\infty \frac{dt}{1+t^2} = \frac{1}{2} g(s_0) \end{aligned}$$

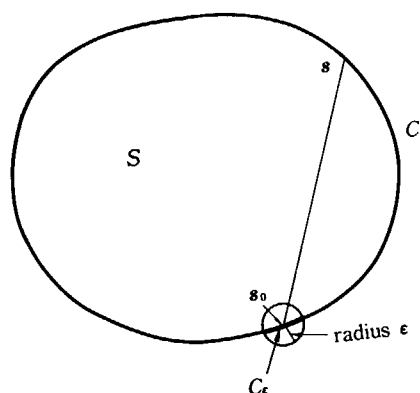


Fig. 2.5.3-3 Path of the principal value integration along the contour.

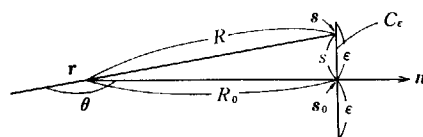


Fig. 2.5.3-4 Path of integration for the singular part.

by taking the limit $R_0 \rightarrow 0$ preceding $\varepsilon \rightarrow 0$. Equation (2.5.3-3) is also proved by

$$\begin{aligned} & \lim_{\varepsilon \rightarrow 0} \lim_{r \rightarrow s_0} \frac{B}{4} \int_{C_i} f(s) \cos \gamma Y_1(BR) ds \\ &= \frac{B}{4} f(s_0) \lim_{\varepsilon \rightarrow 0} \lim_{x \rightarrow \xi_0} \int_{\eta_0 - \varepsilon}^{\eta_0 + \varepsilon} \frac{R_0}{R} \left(-\frac{2}{\pi} \cdot \frac{1}{BR} \right) d\eta \\ &= -\frac{1}{\pi} f(s_0) \lim_{\varepsilon \rightarrow 0} \lim_{R_0 \rightarrow 0} \int_0^\varepsilon \frac{R_0}{R_0^2 + s^2} ds = -\frac{1}{2} \delta(s_0). \end{aligned}$$

Though there are some vertex points or connection points of two line segments on the contour C , and the coefficient of $g(s_0)$ or $f(s_0)$ in the above derivation differs from $1/2$ or $-1/2$ on those points, the measure of line integrals in ϕ_g and ϕ_f is zero on those points. When $\phi(s)$ is given on C , that is, the problem is of Dirichlet type, Eq. (2.5.3-1) or (2.5.3-3) can be used to determine $g(s)$ or $f(s)$, respectively. Equation (2.5.3-3) seems more convenient than Eq. (2.5.3-1) as $\cos \gamma = 0$ if s and s_0 are on the same straight line segment. When $\nabla_n \phi(s)$ is given on C (Neumann problem), Eq. (2.5.3-2) is available and convenient because $\cos \theta = 0$ if s and s_0 are on the same straight line segment.

2.5.3.6 Numerical Solution in a Hexagonal Lattice

We apply Eq. (2.5.3-3) to the Dirichlet problem given in §2.5.3.1 and §2.5.3.2:

$$\nabla^2 \phi + B^2 \phi = 0, \quad B^2 > 0,$$

$$\phi(s) = b(s) \text{ on a hexagonal contour } C.$$

If we assume $g(s) \equiv 0$, $\phi(r)$ for an inner point r is given by

$$\begin{aligned} \phi(r) &= \phi_f(r) = \frac{1}{4\pi} \int_C f(s) \nabla_s [-\pi Y_0(BR)] ds \\ &= \frac{B}{4} \int_C f(s) \cos \gamma Y_1(BR) ds, \end{aligned}$$

then $f(s)$ is determined by the Fredholm's integral equation of the second kind:

$$\phi(s_0) = -\frac{1}{2} f(s_0) + \frac{B}{4} P \int_C f(s) \cos \gamma Y_1(BR) ds = b(s_0).$$

For numerical calculation, the contour is divided into N line segments C_j (for example, each side of a hexagon is divided into ten segments of equal length, giving $N=60$), then $f(s)$ is assumed to be constant f_j on each C_j , the value f_j being assumed to be defined on the middle point of C_j . The value of $b(s_0)$ at the middle point of C_i is also taken as the representative value on C_i . Consequently both f and b are assumed to have piecewise discrete values on C , and

$$-\frac{1}{2} f_i + \frac{B}{4} \sum_{j=1}^N f_j P \int_{C_j} \cos \gamma Y_1(B\|s-s_0\|) ds = b_i. \quad (2.5.3-4)$$

We assume s_0 to be fixed at s_i , the middle point of C_i , and define

$$I_{1ij} = \frac{B}{4} P \int_{C_j} \cos \gamma Y_1(B\|s-s_i\|) ds.$$

The value of I_{1ij} is numerically calculated by using three values of s at both the end points and the middle point of C_j , and integrating them using Simpson's 1/3 rule. It is found by the numerical integration that

$$2 \left| \sum_{j=1}^N I_{1ij} \right| > 1 \quad \text{for each } i,$$

so that the Neumann series expansion is not convergent for solving this integral equation about

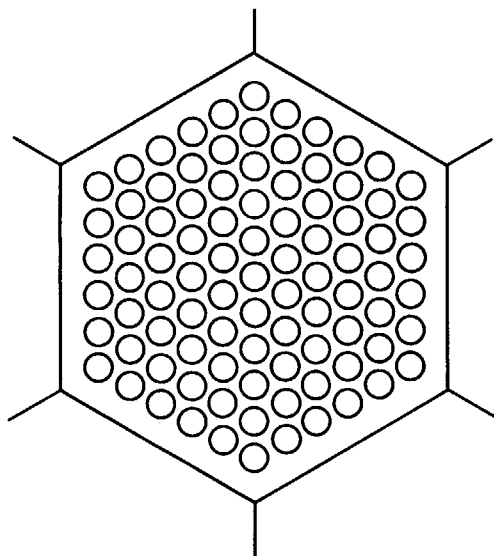


Fig. 2.5.3-5 Arrangement of the fuel pins in the assembly.

$f(s)$. Therefore, we adopt the direct matrix inversion method using a library subroutine in the computer system in double precision mode. We define a matrix A whose element a_{ij} is given by

$$a_{ij} = \begin{cases} I_{1ij} & (i \neq j), \\ I_{1ij} - \frac{1}{2} & (i = j). \end{cases}$$

Equation (2.5.3-4) is now written simply as

$$A\mathbf{f} = \mathbf{b},$$

and \mathbf{f} is determined as $\mathbf{f} = A^{-1}\mathbf{b}$. Even when $N=60$, it takes only about 3 seconds on the FACOM-230/60 to invert A , and the results are sufficiently accurate, as A is a diagonal dominant matrix. The A^{-1} is necessary to be calculated only once for the regions of the same value of B (or κ). This is an advantage of the present method because, once A^{-1} is obtained, \mathbf{f} is directly determined for any boundary condition \mathbf{b} .

Defining
$$I_{2ki} = \frac{B}{4} \int_{C_i} \cos \gamma Y_1(B\|\mathbf{s} - \mathbf{r}_k\|) d\mathbf{s},$$

and using its numerical value prepared once for the value of B (or κ) in the same way as for I_{1ij} , the flux value is given for each fuel pin placed at \mathbf{r}_k inside the region S (see Fig. 2.5.3-5) as follows:

$$\phi_k = \phi(\mathbf{r}_k) = \sum_{i=1}^N I_{2ki} f_i.$$

As the total power has been given for the coarse volume segment, the pin power is simply obtained by $P_k = \text{const} \cdot \phi_k$.

By repeating this procedure for all the coarse volume segments arranged axially, we can obtain the 3-dimensional detailed power distribution about fuel pins and the power peaking factor in the fuel assembly.

2.5.3.7 Example of Application

Two examples of results are given in TABLES 2.5.3-1 and 2.5.3-3, which were obtained by applying the present method to volume segments in fuel assemblies. TABLES 2.5.3-2 and 2.5.3-4 show the deviation of each pin power generation rate from that obtained by the conventional difference scheme. TABLES 2.5.3-1 and 2.5.3-2 are for the segment placed just at the center of the core, whereas TABLES 2.5.3-3 and 2.5.3-4 are for the segment placed between a control rod and a blanket assembly, which is expected to have a rather complicated distribution. The error

TABLE 2.5.3-1 The detailed power distribution for each pin (W/cm) in the
assembly placed at the center of the core (100 MW)

				517.8						
				519.0	518.7					
			519.7	520.0	519.2					
	519.3	519.8	520.9	520.7	519.2					
		521.3	521.8	520.9	518.7					
518.3	521.1	522.4	522.3	522.2	520.7	517.8				
	520.4	522.0	523.3	523.0	522.2	520.0				
519.3	521.1	523.1	523.7	523.2	521.8	519.0				
	522.4	523.7	523.7	523.0	520.9					
519.8	521.3	523.3	523.9	523.3	522.3	519.7				
	522.3	523.7	523.7	523.3	522.4	519.8				
519.7	520.9	523.0	523.7	523.1	521.1					
	521.8	523.2	523.0	523.3	522.0	519.3				
519.0	520.0	522.2	523.0	522.4	520.4					
	520.7	522.2	521.8	522.3	521.1	518.3				
517.8	518.7	520.9	521.8	520.9	519.3					
		519.2	520.7	520.9	519.8					
		519.2	520.0	519.7						
			518.7	519.0						
				517.8						

TABLE 2.5.3-2 Deviations of the detailed power distribution obtained by the
present method (Table 2.5.3-1) from the 2-group conventional
difference scheme $([P(\text{present}) - P(\text{conventional})]/P(\text{conventional}))$
(%)

				0.058						
				0.069	0.035					
			0.112	0.065	0.037					
		0.112	0.079	0.038	0.037					
	0.108	0.111	0.090	0.069	0.044	0.035				
0.139	0.115	0.109	0.096	0.071	0.056	0.038	0.058			
	0.111	0.090	0.090	0.075	0.069	0.069	0.069			
0.108	0.111	0.090	0.082	0.076	0.071	0.079	0.069			
	0.096	0.090	0.082	0.076	0.082	0.092	0.092			
0.112	0.090	0.082	0.076	0.084	0.090	0.090	0.112			
	0.079	0.071	0.076	0.082	0.090	0.096	0.111			
0.069	0.069	0.069	0.075	0.090	0.090	0.111	0.108			
	0.065	0.056	0.071	0.096	0.096	0.115	0.139			
0.058	0.058	0.044	0.056	0.082	0.111	0.108				
	0.035	0.037	0.058	0.079	0.112					
		0.037	0.065	0.092						
			0.035	0.069						
				0.058						

TABLE 2.5.3-3 The detailed power distribution for each pin (W/cm) in the
assembly placed between the control rod and the blanket
assembly in the core (75 MW)

				169.9						
				171.9	170.4					
			173.8	172.5	171.0					
		175.3	174.4	173.1	171.6					
	176.8	176.0	174.9	173.7	172.3					
178.1	177.4	177.9	176.5	175.5	174.3	173.1				
	178.7	177.9	177.1	176.2	175.0	173.1				
179.9	179.1	178.5	177.7	176.8	175.7					
	180.2	179.6	179.0	178.4	177.5	176.1				
181.3	180.5	180.1	179.7	179.1	178.1					
	181.3	180.9	180.7	180.4	179.7	180.4				
182.1	181.5	181.4	181.4	181.1	180.4					
	181.9	181.8	182.0	182.1	181.8	182.4				
182.0	181.9	182.3	183.1	182.9	183.7	182.4				
	181.8	182.3	183.1	183.7	184.7	184.4				
181.5	181.9	182.9	184.0	185.2	185.7					
	181.2	182.3	183.9	185.1	186.5					
		181.2	183.2	185.1	186.6					
		181.9	184.4	185.9						
			183.2	184.8						

TABLE 2.5.3-4 Deviations of the detailed power distribution obtained by the present method (Table 2.5.3-3) from the 6-group conventional difference scheme $([P(\text{present}) - P(\text{conventional})]/P(\text{conventional}))$ (%)

					-0.967				
				-0.555	-0.559	-0.965			
		0.309	-0.144	-0.200	-0.580	-0.956	-0.941		
	0.718		0.205	0.074	-0.211	-0.584	-0.914		
1.239		0.550	0.401	0.001	-0.267	-0.548	-0.500	-0.831	
	0.932		0.253		0.011	-0.214	-0.180	-0.527	
1.346		0.686	0.487	0.241	0.039	0.084	0.184		
	0.964		0.373	0.311	0.201	0.306	0.256	-0.157	
1.358		0.675	0.428	0.371	0.360	0.377	0.553		
	0.845		0.320	0.231	0.336	0.508	0.684		
1.088		0.532	0.038	0.011	0.495	0.682	0.956		
	0.531		0.037		0.312	0.718	1.039	1.224	
0.519		0.182	-0.377	0.256	0.568	0.921	1.393		
	0.017	-0.285	-0.229	0.592	1.403				
-0.143		-0.967	-0.937	0.119	1.188				
	-0.641		-0.554	0.611					
				-0.005					

is less than about 1.5% at each pin even in severe cases such as the latter. This error also contains the contribution due to the 1-group model. The accuracy seems sufficient in these examples. Moreover, the time required in computation is estimated virtually about 1/50~1/100 of the conventional fine mesh scheme because the resolvent kernels are necessary to be prepared only once for one value of B or κ , and the geometrical symmetry can be fully utilized in calculation of the kernels. Number of the values of B or κ can be limited to the number of mixtures which contain fissile elements, that is, the inner fuel, outer fuel, radial blanket, upper axial blanket and lower axial blanket.

This method seems promising not only for 1-group problems but also for multigroup problems involving ϕ_p .

2.6 Burn up Calculation¹⁸⁾

Burn up is calculated under the assumption that neutron flux does not vary in the time interval of Δt days. Four kinds of isotope chains:

- (1) $^{235}\text{U} \rightarrow ^{236}\text{U}$
- (2) $^{238}\text{U} \rightarrow ^{239}\text{Pu} \rightarrow ^{240}\text{Pu} \rightarrow ^{241}\text{Pu} \rightarrow ^{242}\text{Pu}$
- (3) (Fissile + Fertile nuclides) \rightarrow Lumped Fission Product (LFP)
- (4) ^{10}B

are dealt with in HONEYCOMB. The problem is to solve the first order ordinary differential equations for densities of nuclides as initial value problems, and to obtain 3-dimensional distribution of each nuclide after Δt days. From the new densities thus obtained, the new macroscopic cross sections (Σ and D) are determined as average values of the mixture region, and the calculational control is turned back to the few-group r - z calculation (Fig. 2.1.3). In §2.6.1, the equations are solved in each of 3-dimensional volume segments. In §2.6.2, the equations are solved at each fuel pin and at individual axial mesh interval in some specified assemblies. This is for preparing the data required by fuel behavior analysis and fuel inspection.

2.6.1 Burn up Calculation in Each 3-dimensional Volume Segment

(a) Burn up coefficients

In the volume segment (j, i, k) , the burn up coefficient Z for nuclide m and reaction x (x

means fission, capture or absorption) is defined as

$$Z_{xjik}^m = F \sum_n (\sigma_{xjik}^{mn} \times 10^{-24}) \phi_{jik}^n,$$

where n is the group index in a few-group structure and 10^{-24} is the conversion factor of the unit of σ from barns to cm^2 . The factor F has been defined in §2.5.2, and σ in §2.2.4, and ϕ in §2.4. It must be noticed that Z multiplied by the density gives the reaction rate, that is, $NZ = \Sigma\phi$.

(b) Burn up equations

Burn up equations are represented using the Z defined above for each nuclide appearing in the burn up chains. In what follows, the suffixes of the volume element (j, i, k) will be deleted for simplicity. The unit of time t is second. But the unit of densities N^m is still 10^{24} cm^{-3} .

$$(1) \quad \frac{d}{dt} N^{235} + Z_a^{235} N^{235} = 0,$$

$$(2) \quad \frac{d}{dt} N^{236} + Z_a^{236} N^{236} = Z_c^{235} N^{235},$$

$$(3) \quad \frac{d}{dt} N^{238} + Z_a^{238} N^{238} = 0,$$

$$(4) \quad \frac{d}{dt} N^{239} + Z_a^{239} N^{239} = Z_c^{238} N^{238},$$

$$(5) \quad \frac{d}{dt} N^{240} + Z_a^{240} N^{240} = Z_c^{239} N^{239},$$

$$(6) \quad \frac{d}{dt} N^{241} + Z_a^{241} N^{241} = Z_c^{240} N^{240},$$

$$(7) \quad \frac{d}{dt} N^{242} + Z_a^{242} N^{242} = Z_c^{241} N^{241},$$

$$(8) \quad \frac{d}{dt} N^{LFP} + \lambda^{LFP} N^{LFP} = \gamma^{235} Z_i^{235} N^{235} + \gamma^{236} Z_i^{236} N^{236} + \gamma^{238} Z_i^{238} N^{238} \\ + \gamma^{239} Z_i^{239} N^{239} + \gamma^{240} Z_i^{240} N^{240} + \gamma^{241} Z_i^{241} N^{241} + \gamma^{242} Z_i^{242} N^{242},$$

$$(9) \quad \frac{d}{dt} N^{10} + Z_a^{10} N^{10} = 0.$$

(c) Solution of burn up equations

The above equations are written generally as

$$\frac{d}{dt} f(t) + af(t) = g(t),$$

and the solution is given by

$$f(t) = e^{-at} \int_0^t e^{au} g(u) du + e^{-at} f(0).$$

Equation (8) is, however, approximately solved by using the following average quantity:

$$\bar{g} = [g(t) + g(t+h)]/2,$$

where $h = 86400 \times \Delta t$ sec. Thus we have solutions for Eqs. (1)~(9),

$$(1) \quad N^{235}(t+h) = N^{235}(t) \exp(-Z_a^{235}h),$$

$$(2) \quad N^{236}(t+h) = N^{236}(t) \exp(-Z_a^{236}h) \\ + Z_c^{235} N^{235}(t) \{ \exp(-Z_a^{236}h) - \exp(-Z_a^{235}h) \} / (Z_a^{235} - Z_a^{236}),$$

$$(3) \quad N^{238}(t+h) = N^{238}(t) \exp(-Z_a^{238}h),$$

$$(4) \quad N^{239}(t+h) = N^{239}(t) \exp(-Z_a^{239}h) \\ + C_1 \{ \exp(-Z_a^{239}h) - \exp(-Z_a^{238}h) \}, \\ C_1 = Z_c^{238} N^{238}(t) / (Z_a^{238} - Z_a^{239}),$$

$$\begin{aligned}
(5) \quad N^{240}(t+h) &= N^{240}(t) \exp(-Z_a^{240}h) \\
&\quad - C_2 \{ \exp(-Z_a^{240}h) - \exp(-Z_a^{238}h) \} \\
&\quad + C_3 \{ \exp(-Z_a^{240}h) - \exp(-Z_a^{239}h) \}, \\
C_2 &= Z_c^{239} C_1 / (Z_a^{238} - Z_a^{240}), \\
C_3 &= Z_c^{239} \{ N^{239}(t) + C_1 \} / (Z_a^{239} - Z_a^{240}), \\
(6) \quad N^{241}(t+h) &= N^{241}(t) \exp(-Z_a^{241}h) \\
&\quad + C_4 \{ \exp(-Z_a^{241}h) - \exp(-Z_a^{238}h) \} \\
&\quad - C_5 \{ \exp(-Z_a^{241}h) - \exp(-Z_a^{239}h) \} \\
&\quad + C_6 \{ \exp(-Z_a^{241}h) - \exp(-Z_a^{240}h) \}, \\
C_4 &= Z_c^{240} C_2 / (Z_a^{238} - Z_a^{241}), \\
C_5 &= Z_c^{240} C_3 / (Z_a^{239} - Z_a^{241}), \\
C_6 &= Z_c^{240} \{ N^{240}(t) - C_2 + C_3 \} / (Z_a^{240} - Z_a^{241}), \\
(7) \quad N^{242}(t+h) &= N^{242}(t) \exp(-Z_a^{242}h) \\
&\quad - C_7 \{ \exp(-Z_a^{242}h) - \exp(-Z_a^{238}h) \} \\
&\quad + C_8 \{ \exp(-Z_a^{242}h) - \exp(-Z_a^{239}h) \} \\
&\quad - C_9 \{ \exp(-Z_a^{242}h) - \exp(-Z_a^{240}h) \} \\
&\quad + C_{10} \{ \exp(-Z_a^{242}h) - \exp(-Z_a^{241}h) \}, \\
C_7 &= Z_c^{241} C_4 / (Z_a^{238} - Z_a^{242}), \\
C_8 &= Z_c^{241} C_5 / (Z_a^{239} - Z_a^{242}), \\
C_9 &= Z_c^{241} C_6 / (Z_a^{240} - Z_a^{242}), \\
C_{10} &= Z_c^{241} \{ N^{241}(t) + C_4 - C_5 + C_6 \} / (Z_a^{241} - Z_a^{242}), \\
(8) \quad N^{\text{LFP}}(t+h) &= N^{\text{LFP}}(t) \exp(-\lambda^{\text{LFP}}h) + h(\gamma^{235} Z_t^{235} \bar{N}^{235} \\
&\quad + \gamma^{236} Z_t^{236} \bar{N}^{236} + \gamma^{238} Z_t^{238} \bar{N}^{238} + \gamma^{239} Z_t^{239} \bar{N}^{239} \\
&\quad + \gamma^{240} Z_t^{240} \bar{N}^{240} + \gamma^{241} Z_t^{241} \bar{N}^{241} + \gamma^{242} Z_t^{242} \bar{N}^{242}), \\
\bar{N} &= \{ N(t) + N(t+h) \} / 2, \\
(9) \quad N^{10}(t+h) &= N^{10}(t) \exp(-Z_a^{10}h).
\end{aligned}$$

In the actual calculation of the above solutions, we must be careful to avoid the decrease in the number of significant digits due to cancellation caused by taking the difference between two numbers having almost the same values, that is, in our case,

$$e^{-a} - e^{-b} \quad (0 < a < 0.1, \quad 0 < b < 0.1).$$

We used the Taylor's series expansion for these cases as follows:

$$e^{-a} - e^{-b} \doteq (b-a) \{ 1 - (a+b)/2 + (a^2 + ab + b^2)/6 - (a+b)(a^2 + b^2)/24 \}.$$

The resulting $N^m(t+h)$ of all the volume segments thus obtained are stored in an auxiliary memory, and are used as the initial values at the next time step.

2.6.2 Burn up Calculation for Each Fuel Pin

In a few (up to 10) fuel or blanket assemblies, the 3-dimensional burn up calculation can be carried out within a reasonable computation time. For this purpose, the 3-dimensional fine distribution of neutron flux is calculated in a 6-group model independently in each specified assembly. The axial mesh structure is taken in common with that in §2.4.1, and §2.4.3, whereas radial meshes are made so fine that every small hexagonal mesh region contains a fuel pin in its center. Letting the pin pitch be t_1 , a fine mesh difference diffusion scheme is used for the present calculation where the each coarse volume segment (a hexagonal column of height Δz) is assumed to have homogeneous composition for the flux calculation. Boundary conditions for the radial boundary are given in a homogeneous type $(\nabla_{\perp} \phi / \phi)$ by interpolating the coarse mesh fluxes as obtained previously. As illustrated in Fig. 2.6.2-1, the boundary surface A has an area of $(t_1/\sqrt{3})\Delta z_k$, where the neutron current must be determined by the fine mesh flux ξ in the small

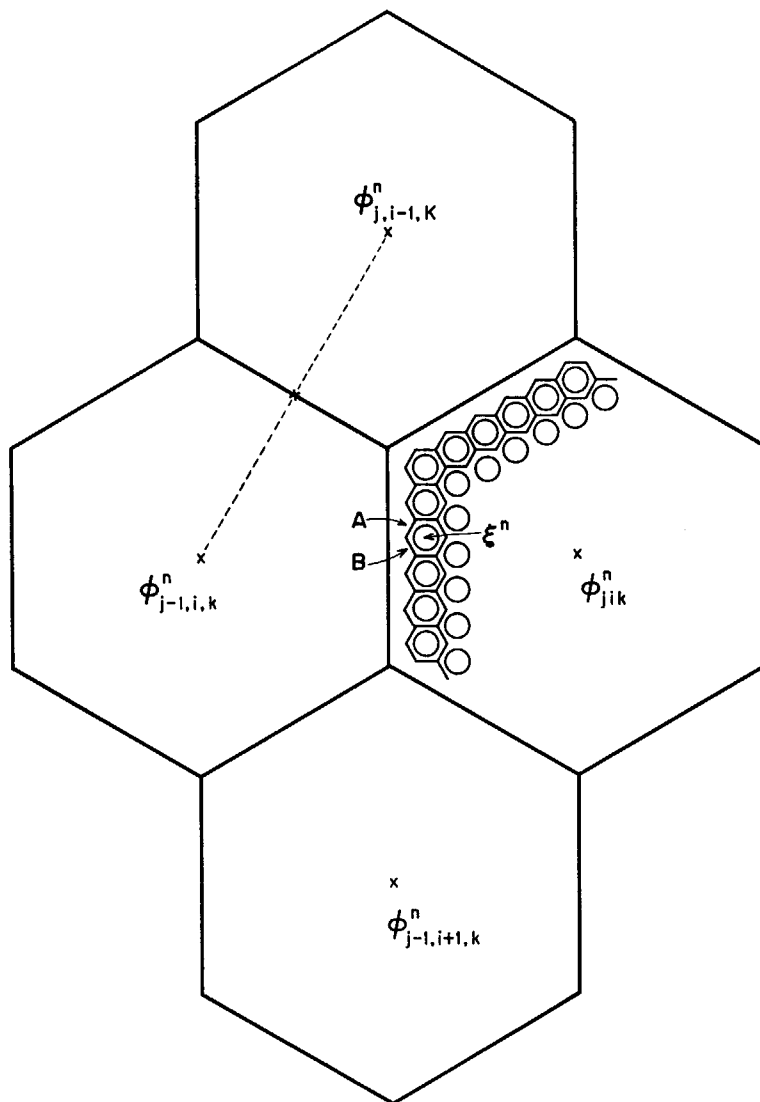


Fig. 2.6.2-1 Radial boundaries (A or B) for "pin-hexagonal-z" criticality calculation.

hexagon, ξ being not yet known. The coefficient of the current term $a_A \xi$ is estimated from

$$a_A^n \frac{\phi_{jik}^n + \phi_{j-1,i,k}^n}{2} = \frac{t_1}{\sqrt{3}} \Delta z_k D_{jik}^n \frac{\phi_{jik}^n - \frac{1}{2}(\phi_{j-1,i,k}^n + \phi_{j,i-1,k}^n)}{\frac{3}{2} \times \frac{t}{\sqrt{3}}},$$

that is,

$$a_A^n = \frac{2}{3} \frac{t_1}{t} \Delta z_k D_{jik}^n \frac{2\phi_{jik}^n - \phi_{j-1,i,k}^n - \phi_{j,i-1,k}^n}{\phi_{jik}^n + \phi_{j-1,i,k}^n}.$$

At the boundary B adjacent to A, a_B^n is obtained with the same formula, where $\phi_{j,i-1,k}^n$ is substituted by $\phi_{j-1,i+1,k}^n$. These coefficients, thus obtained at the radial boundaries, are naturally so roughly approximated that the neutron balance in an assembly cannot be maintained. For the correction of that, a factor Q is multiplied to all the a_A^n or a_B^n to maintain the neutron balance in the assembly. This means that a kind of criticality adjustment by the Q value is needed besides the usual iterations. In the following, a_1, a_2, \dots, a_7 are defined like in §2.4.3 under a fixed (j, i) .

$$(1) \quad a_{1k}^n = a_{2k}^n = a_{3k}^n = \frac{\Delta z_k}{\sqrt{3}} D_{jik}^n \quad (\text{between two pins}),$$

$$(2) \quad a_{4,k+1}^n = \begin{cases} \left(\frac{\sqrt{3} t_1^2}{\Delta z_1} \left(\frac{4.2626}{\Delta z_1} + \frac{1}{D_{ji1}^n} \right) \right)^{-1} & (k=0), \\ \left(\frac{\sqrt{3} t_1^2}{\Delta z_k} \left(\frac{\Delta z_{k+1}}{\Delta z_k} \frac{1}{D_{j,i,k+1}^n} + \frac{1}{D_{jik}^n} \right) \right)^{-1} & (1 \leq k \leq M-1), \\ \left(\frac{\sqrt{3} t_1^2}{\Delta z_M} \left(\frac{4.2626}{\Delta z_M} + \frac{1}{D_{jiM}^n} \right) \right)^{-1} & (k=M), \end{cases}$$

$$(3) \quad a_{5k}^n = \frac{\sqrt{3}}{2} t_1^2 \Delta z_k \Sigma_{Tjik}^n,$$

$$(4) \quad a_{6k}^n = \frac{\sqrt{3}}{2} t_1^2 \Delta z_k (\nu \Sigma_f)_{jik}^n,$$

$$(5) \quad a_{7k}^{l \rightarrow n} = \frac{\sqrt{3}}{2} t_1^2 \Delta z_k \Sigma_{sjik}^{l \rightarrow n}.$$

These coefficients, except for a_A^n and a_B^n , are all independent of the location of pin (j' , i'), whereas they are dependent on only axial mesh k and group n . The fine distribution of neutron flux ξ^n is obtained by solving the diffusion equation:

$$-D^n \nabla^2 \xi^n + \Sigma_T^n \xi^n = \lambda \chi^n \sum_l (\nu \Sigma_f)^l \xi^l + \sum_{l=1}^{n-1} \Sigma_s^{l \rightarrow n} \xi^l,$$

using a difference scheme in the mesh structure (j' , i' , k). The factor Q is searched so as to make $\lambda=1$.

The resulting values of $\xi_{j'i'k}^n$ are used to determine the burn up coefficients for pin burn up calculation:

$$Z_{xj'i'k}^m = \frac{C_f P_{fjik} \Delta V_{jik}}{\sum_n (\Sigma_{fjik}^n \sum_{j'i'} \xi_{j'i'k}^n \Delta V_{j'i'k})} \cdot \sum_n (\sigma_{xjik}^{mn} \times 10^{-24}) \xi_{j'i'k}^n,$$

where the first factor is the power normalization factor to $\xi_{j'i'k}^n$. The C_f and P_f were defined in §2.5.2. The other symbols (m , x etc.) have the same meanings as in §2.6.1 ($\Delta V_{j'i'k} = (\sqrt{3}/2) t_1^2 \Delta z_k$).

The initial compositions of fuel pins are given by input data for the inner fuel, outer fuel, radial blanket and axial blankets, apart from the smeared densities used in the criticality calculations. The burn up equations in §2.6.1 (except that of ^{10}B) are again solved using the coefficients $Z_{xj'i'k}^m$ and the initial density of each nuclide composing the fuel pin. The resulting densities at the time after Δt days are printed out and stored apart from the results of §2.6.1.

2.7 Applicability Tests of the Code HONEYCOMB

In this section, two kinds of test calculations are presented so as to confirm the applicability of this code HONEYCOMB for predicting the nuclear characteristics of fast reactor systems. The section 2.7.1 shows an example of each input item and the computation time (CPU time on IBM-360/K195) required in each calculational part as a typical case of applications. The section 2.7.2 is for a detailed examination of mesh size effects in an x - y mid-plane. There, the 2-dimensional 6-group calculations are performed in hexagonal and triangular mesh structures varying the control rod blackness, the material composition and the size of hexagon, over the ranges used for the most of actual fast reactors. By these test calculations, it has been concluded that HONEYCOMB has a sufficient accuracy and efficiency for the practical use in a wide range of each parameter surveyed.

2.7.1 A Sample Problem

2.7.1.1 Example of Input Data

An example of input data by cards is shown in Figs. 2.7.1-1~2.7.1-9. Figure 2.7.1-1 gives

** JOYO NUCLEAR CHARACTERISTICS AT INITIAL CORE., FINE DISTRI. OF 4A4, 5A5 **

PAGE 1

DATA FOR MULTIGROUP R-Z CALCULATION

```

MIXTURE 1 GROUPS DOWN-SC. COLLAPSE 6 K-PARAM 0 R-BLOCKS 6 Z-BLOCKS 5 J(ROD) 0 J(ROD) 0 EXPECTED KEFF
9 25 11 6 0 0 1.000000E 00

NO. OF ELEMENTS FOR EACH MIXTURE
14 8 4 14 14 14 4 5 5

TEMPERATURE FOR EACH MIXTURE
3.00000E 02 3.00000E 02 3.00000E 02 3.00000E 02 3.00000E 02 3.00000E 02 3.00000E 02 3.00000E 02 3.00000E 02

LAST GROUPS FOR COLLAPSE
4 6 8 11 14 25

INTERFACE POINT NUMBERS FOR RADIAL BLOCKS
3 4 6 10 11 12

RADIAL MESH SIZES
6.76300E 00 2.54800E 00 6.86150E 00 8.27450E 00 6.04600E 00 1.12960E 01

INTERFACE POINT NUMBERS FOR AXIAL BLOCKS
1 5 11 15 16

AXIAL MESH SIZES
2.00000E 01 1.00000E 01 1.00000E 01 1.00000E 01 2.00000E 01

COMPOSITION MAP
1 2 3 4 5 6 7 8 9 10 11 12
1 9 8 8 2 8 8 8 8 8 7 7
2 6 6 6 2 6 6 5 5 5 5 7 7
3 6 6 6 2 6 6 5 5 5 5 7 7
4 6 6 6 2 6 6 5 5 5 5 7 7
5 6 6 6 2 6 6 5 5 5 5 7 7
6 1 1 1 2 4 4 5 5 5 5 7 7
7 1 1 1 2 4 4 5 5 5 5 7 7
8 1 1 1 2 4 4 5 5 5 5 7 7
9 1 1 1 3 4 4 5 5 5 5 7 7
10 1 1 1 3 4 4 5 5 5 5 7 7
11 1 1 1 3 4 4 5 5 5 5 7 7
12 6 6 6 3 6 6 5 5 5 5 7 7
13 6 6 6 3 6 6 5 5 5 5 7 7
14 6 6 6 3 6 6 5 5 5 5 7 7
15 6 6 6 3 6 6 5 5 5 5 7 7
16 9 9 9 3 9 9 9 9 9 9 7 7

```

Fig. 2.7.1-1 Data for 25-group r-z calculation.

** JOYO NUCLEAR CHARACTERISTICS AT INITIAL CORE., FINE DISTRI. OF 4A4, 5A5 **

PAGE 2

ELEMENT CODE NUMBERS

```

MIXTURE 1
949 940 941 942 925 928 926 999 8 11 24 26 28 42

MIXTURE 2
105 115 6 11 24 26 28 42

MIXTURE 3
11 24 26 28

MIXTURE 4
949 940 941 942 925 928 926 999 8 11 24 26 28 42

MIXTURE 5
949 940 941 942 925 928 926 999 8 11 24 26 28 42

MIXTURE 6
949 940 941 942 925 928 926 999 8 11 24 26 28 42

MIXTURE 7
11 24 26 28

MIXTURE 8
11 24 26 28 42

MIXTURE 9
11 24 26 28 42

```

Fig. 2.7.1-2 Nuclides in each mixture.

** JOYO NUCLEAR CHARACTERISTICS AT INITIAL CORE., FINE DISTRI. OF 4A4, 5A5 **

PAGE 3

EFFECTIVE DENSITIES

```

MIXTURE 1
1.13000E-03 2.79000E-04 5.41100E-05 1.01900E-05 1.60500E-03 5.29400E-03 0.0 C.0 1.65800E-02 9.68800E-03
3.27400E-03 1.19300E-02 2.38900E-03 2.61000E-04

MIXTURE 2
2.06600E-02 1.85900E-03 5.63000E-03 1.25300E-02 3.53900E-03 1.28900E-02 2.58200E-03 2.82100E-04

MIXTURE 3
2.08400E-02 1.39200E-02 4.84300E-03 6.48900E-04

MIXTURE 4
1.13000E-03 2.79000E-04 5.41100E-05 1.01900E-05 1.60500E-03 5.29400E-03 0.0 C.0 1.65800E-02 9.68800E-03
3.27400E-03 1.19300E-02 2.38900E-03 2.61000E-04

MIXTURE 5
0.0 0.0 0.0 0.0 2.22900E-05 1.10100E-02 0.0 C.0 2.20600E-02 7.34300E-03
2.84600E-03 1.03700E-02 2.07600E-03 2.26800E-04

MIXTURE 6
0.0 0.0 0.0 0.0 1.68300E-05 8.31200E-03 0.0 C.0 1.66600E-02 9.68800E-03
3.27400E-03 1.19300E-02 2.38900E-03 2.61000E-04

MIXTURE 7
4.41900E-03 1.40500E-02 4.88800E-02 6.55000E-03

MIXTURE 8
9.49300E-03 3.37400E-02 1.22900E-02 2.46100E-03 2.68900E-04

MIXTURE 9
1.40000E-02 5.97700E-03 2.17700E-02 4.36100E-03 4.76400E-04

```

Fig. 2.7.1-3 Smeared densities of nuclides in each mixture (initial values).

```

** JOYO NUCLEAR CHARACTERISTICS AT INITIAL CORE., FINE DISTR. OF 444, 5A5 **

DATA FOR TWO-DIMENSIONAL R-Z CALCULATION

NO. OF RADIAL BLOCKS = 6

INTERFACE POINT NUMBERS FOR RADIAL BLOCKS
  4      5      8      12     13     14

RADIAL MESH SIZES
5.07200E 00 2.54800E 00 4.57400E 00 8.27450E 00 6.04600E 00 1.12960E 01

NO. OF AXIAL BLOCKS = 5

INTERFACE POINT NUMBERS FOR AXIAL BLOCKS
  1      6      18     23     24

AXIAL MESH SIZES
2.00000E 01 8.00000E 00 5.00000E 00 8.00000E 00 2.00000E 01

MESH POINTS FOR EACH RADIAL ZONE
  1      2      3      6      7      8      9      10     11     12     13

MESH POINTS FOR TOP AND BOTTOM OF THE CORE
  7      18

NO. OF RADIAL BLOCKS OF 8SQ-Z = 5

INTERFACE POINT NUMBERS FOR RADIAL BLOCKS OF 8SQ-Z
  4      5      8      12     13

```

PAGE 4

Fig. 2.7.1-4 Radial and axial block data for few-group r - z calculation.

** JOYD NUCLEAR CHARACTERISTICS AT INITIAL CORE., FINE DISTRI. OF 4A4, 5A5 **

PAGE 5

[illegible]

Fig. 2.7.1-5 Composition map for few-group r - z calculation.

** JOYO NUCLEAR CHARACTERISTICS AT INITIAL CORE., FINE DISTRI. OF 4A4. 5A5 **

PAGE 6

DATA FOR TWO-DIMENSIONAL HEXA CALCULATION

PITCH = 8.1499956F CC

COMPOSITION MAP

[illegible]

BS Q-Z MAP

[illegible]

Fig. 2.7.1-6 Composition and BSQ-Z maps for few-group hexagonal calculation.

** JOYO NUCLEAR CHARACTERISTICS AT INITIAL CORE., FINE DISTRI. OF 4A4, 5A5 **

PAGE 7

DATA FOR THREE-DIMENSIONAL HEXA-Z CALCULATION

CRITICALITY IS ADJUSTED BY 2 RODS.

INITIAL GUESS OF INSERTION DEPTH(MESH) FOR THESE RODS = 15

PLACES OF THESE RODS = (10, 5) , (6,11)

COMPOSITION MAP (AXIAL MESH FROM 1 TO 1)

0	0	0	0	0	C	0	8	8	8	8	8	8	8
0	0	0	0	0	C	8	8	8	8	8	8	8	8
0	0	0	0	0	8	8	8	8	8	8	8	8	8
0	0	0	0	8	8	8	8	8	8	8	8	8	8
0	0	0	8	8	8	8	8	8	8	8	8	8	8
0	0	8	8	8	8	2	8	8	8	8	8	8	8
0	8	8	8	8	8	8	8	8	8	2	8	8	8
8	8	8	8	8	8	8	8	8	8	8	8	8	8
8	8	8	8	2	8	8	8	8	8	8	8	8	0
8	8	8	8	8	8	8	8	2	8	8	8	8	0
8	8	8	8	8	2	8	8	8	8	8	8	0	0
8	8	8	8	8	8	8	8	8	8	8	0	0	0
8	8	8	8	8	8	8	8	8	8	0	0	0	0
8	8	8	8	8	8	8	8	8	0	0	0	0	0
8	8	8	8	8	8	8	8	0	0	0	0	0	0

COMPOSITION MAP (AXIAL MESH FROM 2 TO 3)

0	0	0	0	0	C	5	5	5	5	5	5	5	5
0	0	0	0	0	C	5	5	5	5	5	5	5	5
0	0	0	0	0	5	5	5	5	5	5	5	5	5
0	0	0	0	5	5	5	5	5	5	5	5	5	5
0	0	0	5	5	5	5	5	5	5	5	5	5	5
0	0	5	5	5	5	5	5	5	5	5	5	5	5
0	5	5	5	5	5	5	5	5	5	5	5	5	5
5	5	5	5	5	5	5	5	5	5	5	5	5	5
5	5	5	5	5	5	5	5	5	5	5	5	5	5
5	5	5	5	5	5	5	5	5	5	5	5	5	5
5	5	5	5	5	5	5	5	5	5	5	5	5	5
5	5	5	5	5	5	5	5	5	5	5	5	5	5
5	5	5	5	5	5	5	5	5	5	5	5	5	5
5	5	5	5	5	5	5	5	5	5	5	5	5	5
5	5	5	5	5	5	5	5	5	5	5	5	5	5

Fig. 2.7.1-7-1 Data for few-group hexagonal-z calculation and criticality adjustment by control rods.

** JOYO NUCLEAR CHARACTERISTICS AT INITIAL CORE., FINE DISTRI. OF 4A4, 5A5 **

PAGE 8

COMPOSITION MAP (AXIAL MESH FROM 4 TO 6)

0	0	0	0	0	C	5	5	5	5	5	5	5	5
0	0	0	0	0	C	5	5	5	5	5	5	5	5
0	0	0	0	0	5	5	5	5	5	5	5	5	5
0	0	0	0	5	5	5	5	5	5	5	5	5	5
0	0	0	5	5	5	5	5	5	5	5	5	5	5
0	0	5	5	5	5	5	5	5	5	5	5	5	5
0	5	5	5	5	5	5	5	5	5	5	5	5	5
5	5	5	5	5	5	5	5	5	5	5	5	5	5
5	5	5	5	5	5	5	5	5	5	5	5	5	5
5	5	5	5	5	5	5	5	5	5	5	5	5	5
5	5	5	5	5	5	5	5	5	5	5	5	5	5
5	5	5	5	5	5	5	5	5	5	5	5	5	5
5	5	5	5	5	5	5	5	5	5	5	5	5	5
5	5	5	5	5	5	5	5	5	5	5	5	5	5

COMPOSITION MAP (AXIAL MESH FROM 7 TO 18)

0	0	0	0	0	C	5	5	5	5	5	5	5	5
0	0	0	0	0	C	5	5	5	5	5	5	5	5
0	0	0	0	0	5	5	5	5	5	5	5	5	5
0	0	0	0	5	5	5	5	5	5	5	5	5	5
0	0	0	5	5	5	5	5	5	5	5	5	5	5
0	0	5	5	5	5	5	5	5	5	5	5	5	5
0	5	5	5	5	5	5	5	5	5	5	5	5	5
5	5	5	5	5	5	5	5	5	5	5	5	5	5
5	5	5	5	5	5	5	5	5	5	5	5	5	5
5	5	5	5	5	5	5	5	5	5	5	5	5	5
5	5	5	5	5	5	5	5	5	5	5	5	5	5
5	5	5	5	5	5	5	5	5	5	5	5	5	5
5	5	5	5	5	5	5	5	5	5	5	5	5	5
5	5	5	5	5	5	5	5	5	5	5	5	5	5

COMPOSITION MAP (AXIAL MESH FROM 19 TO 23)

0	0	0	0	0	C	5	5	5	5	5	5	5	5
0	0	0	0	0	C	5	5	5	5	5	5	5	5
0	0	0	0	0	5	5	5	5	5	5	5	5	5
0	0	0	0	5	5	5	5	5	5	5	5	5	5
0	0	5	5	5	5	5	5	5	5	5	5	5	5
0	5	5	5	5	5	5	5	5	5	5	5	5	5
5	5	5	5	5	5	5	5	5	5	5	5	5	5
5	5	5	5	5	5	5	5	5	5	5	5	5	5
5	5	5	5	5	5	5	5	5	5	5	5	5	5
5	5	5	5	5	5	5	5	5	5	5	5	5	5
5	5	5	5	5	5	5	5	5	5	5	5	5	5
5	5	5	5	5	5	5	5	5	5	5	5	5	5
5	5	5	5	5	5	5	5	5	5	5	5	5	5
5	5	5	5	5	5	5	5	5	5	5	5	5	5

Fig. 2.7.1-7-2 Data for few-group hexagonal-z calculation (continued).

** JOYO NUCLEAR CHARACTERISTICS AT INITIAL CORE., FINE DISTRI. OF 4A4, 5A5 **

PAGE 9

COMPOSITION MAP (AXIAL MESH FROM 24 TO 24)

0	0	0	0	0	C	9	9	9	9	9	9	9	9
0	0	0	0	0	C	9	9	9	9	9	9	9	9
0	0	0	0	0	9	9	9	9	9	9	9	9	9
0	0	0	0	9	9	9	9	9	9	9	9	9	9
0	0	9	9	9	9	9	9	9	9	9	9	9	9
0	9	9	9	9	9	9	9	9	9	9	9	9	9
9	9	9	9	9	9	9	9	9	9	9	9	9	9
9	9	9	9	9	9	9	9	9	9	9	9	9	9
9	9	9	9	9	9	9	9	9	9	9	9	9	9
9	9	9	9	9	9	9	9	9	9	9	9	9	9
9	9	9	9	9	9	9	9	9	9	9	9	9	9
9	9	9	9	9	9	9	9	9	9	9	9	9	9
9	9	9	9	9	9	9	9	9	9	9	9	9	9
9	9	9	9	9	9	9	9	9	9	9	9	9	9

Fig. 2.7.1-7-3 Data for few-group hexagonal-z calculation (continued).

** JOYO NUCLEAR CHARACTERISTICS AT INITIAL CORE., FINE DISTRI. OF 444, 5A5 **

PAGE 10

DETAILED POWER DISTRIBUTION AND BURN UP FOR EACH FUEL PIN ARE CALCULATED IN THE FOLLOWING 2 ASSEMBLIES.

J	14	15
1	7	6

PIN DENSITIES	
COMP.NO.	925 926 928 949 940 941 942 999
1	4.43000E-03 C.0 1.46120E-02 3.11900E-03 7.70100E-04 1.49350E-04 2.81260E-05 0.0
2	4.64500E-05 C.0 2.29420E-02 0.0 0.0 0.0 0.0 0.0

COMPOSITION MAP OF PINS IN EACH ASSEMBLY FOR EACH AXIAL MESH	
J	1 2 3 4 5 6 7 8 9 10 11 12 13 14 15 16 17 18 19 20 21 22 23 24
14	7 0 2 2 2 2 2 1 1 1 1 1 1 1 1 1 1 1 2 2 2 2 0
15	6 0 2 2 2 2 2 2 2 2 2 2 2 2 2 2 2 2 2 2 2 0

Fig. 2.7.1-8 Data for few-group pin-hexagonal-z calculation.

** JOYO NUCLEAR CHARACTERISTICS AT INITIAL CORE., FINE DISTRI. OF 444, 5A5 **

PAGE 11

DATA FOR BURN UP CALCULATION

NO. OF TIME STEPS = 1 3-DIM. ADJOINT FLUX = 0 PRINT OPTION = 1

POWER = 7.50000E 01 MW/TON LIM. = 1.00000E 04 DELTA KEFF = 5.00E-01 MINIMUM KEFF = 9.50E-01

DELTA-T (DAYS)
45.0

INITIAL MASS (TON)

U235	U236	U238	PU239	PU240	PU241	PU242	A (EXCEPT U2361)
1.6030461E-01	0.0	8.2230358E 00	1.0367703E-01	2.5705531E-02	5.0061978E-03	9.4698765E-04	8.5186739E 00

BURNUP LIMIT = 1125.8 DAYS

END INPUT TIME = 1.15 (SEC)

END MICRO TIME = 5.24 (SEC)

Fig. 2.7.1-9 Data for burn-up calculation.

the data used mainly in §2.2.3 and §2.2.4. "Expected k_{eff} " in the upper right corner is the K_c in §2.4.5. It gives also the number of mixtures, number of nuclides in each mixture, and Kelvin temperatures (≥ 300). Figure 2.7.1-2 shows the kinds of nuclides in each mixture where the code numbers of nuclides are used as defined in TABLE 2.2.1-1. Figure 2.7.1-3 shows the smeared densities of nuclides in each mixture. The ordering of the data is common to that given in Fig. 2.7.1-2. Few-group cross sections are obtained from the above data.

Figure 2.7.1-4 gives the data for the few-group r - z calculation (see §2.4.1). The values of l in ϕ_l^n and l' in $(B_z^2)_{l'}^n$ are specified there. Figure 2.7.1-5 is the composition map for this r - z calculation corresponding to Fig. 2.1.1-2. Figure 2.7.1-6 is the data for 2-dimensional hexagonal (§2.4.2) or triangular (§2.3) calculations. The composition map corresponds to Fig. 2.1.1-1, and the BSQ-Z map shows the assignment of the values of l' in $(B_z^2)_{l'}^n$ defined in §2.4.1. Figure 2.7.1-7 is the data concerning the 3-dimensional criticality calculation (§2.4.3) and the criticality adjustment by insertion depth of control rods (§2.4.5). The composition maps are easily understood in comparison with Figs. 2.1.1-1 (up to 8-th zone) and 2.1.1-2 (left region of vertical dotted lines). The coordinates of the rods, which are going to be adjusted their insertion depth, must be less by 3 than those defined in Fig. 2.4.2-1 ($j-3, i-3$).

Figure 2.7.1-8 shows the data for pin-hexagonal- z criticality calculation and pin-burn-up calculation described in §2.6.2. Figure 2.7.1-9 is the data for the burn up calculation given in §2.6.1 and the data for the computer control of the whole time steps of burn up calculation. "Initial mass" is the integrated totals obtained immediately after input of densities, composition map and volume of each segment. The mass "A" is used in the succeeding time steps for calculating "degree of burn up" in the whole reactor region:

$$BP = [P \text{ (MW)}] \times [\text{Burn up time (day)}] / [A \text{ (ton)}].$$

In this example, only one step of burn up calculation is carried out with $\Delta t = 45$ days and $P = 75$ MW. The option for adjoint flux calculation is skipped.

2.7.1.2 Computer Time Required for Each Item of Calculation

The core memories occupied in the computer for this sample problem are 484K bites including all the library subroutines and input/output buffer areas. The time of usage of the central

TABLE 2.7.1-1 CPU time required for each segment in case of the test problem
given in §2.7.1

Overlay segment	CPU time (sec)
Reading of data cards, and some preparatory calc.	1.19
25-group effective cross sections	4.05
25-group R-Z calculation	24.90
Collapsing of group cross sections	0.18
(Initial step before burn-up)	
6-group R-Z calculation	14.83
6-group hexagonal calculation	16.69
6-group hexagonal-Z calculation	572.49(*)
6-group pin-hexagonal-Z calculation (91 pins)	630.18(*)
6-group pin-hexagonal-Z calculation (19 pins)	56.71(*)
3-group γ -ray flux distribution	41.57
Power distribution (coarse & fine mesh)	7.02
Burn-up calculation (coarse mesh)	9.97
Pin-burn-up calculation (two assemblies)	1.18
New macroscopic cross sections	12.07
(First time-step)	
6-group R-Z calculation	16.55
6-group hexagonal calculation	16.79
6-group hexagonal-Z calculation	522.03(*)
6-group pin-hexagonal-Z calculation (91 pins)	622.23(*)
6-group pin-hexagonal-Z calculation (19 pins)	55.64(*)
3-group γ -ray flux distribution	42.24
Power distribution (coarse & fine mesh)	5.10
Total	2,674.24 (about 44.5 min)

(*) means that the figure contains time for criticality adjustment.

TABLE 2.7.1-2 Variations of some integral quantities by 45 days' burn-up

Quantities	Time (day)	Burn-up (MWD/T)	Critical insertion depth of two control rods (cm)	Mass of each isotope of U and Pu (kg)						
				²³⁵ U	²³⁶ U	²³⁸ U	²³⁹ Pu	²⁴⁰ Pu	²⁴¹ Pu	²⁴² Pu
Initial step	0	0	103.0	160.3	0	8223	103.7	25.71	5.006	0.9470
First step	45	396.2	96.1	158.3	0.394	8219	105.7	25.77	4.970	0.9530
Increase	45	396.2	-6.9	-1.98	0.394	-3.82	2.04	0.0600	-0.0361	0.00606

processing unit (CPU) is shown in TABLE 2.7.1-1. The computer used is the IBM-360/K195. The number of groups is 6 and the number of axial mesh intervals is 24. One fuel assembly containing 91 pins and one blanket assembly containing 19 pins are specified to perform the pin-burn-up calculation. The CPU time is tabled following the flow of calculation of Figs. 2.1.3-1~2.1.3-3.

The variations of the main integral quantities by the 45 days' burn up are summarized in TABLE 2.7.1-2. All of output prints amounts to about 600 pages including detailed distributions of the neutron flux, power and nuclide densities.

2.7.2 Examination of Mesh Size Effects

From the comparison between hexagonal and triangular mesh criticality calculations in the 2-dimensional diffusion model (see §2.3.5), it was seen that the main problem in the coarse hexagonal mesh scheme was related to the accuracy of the neutron flux values in and around

control rods. Another question existed also in the accuracy of the flux in the blanket regions. For the former shortcoming, the correction method in §2.4.4 has been proved very effective. For the latter, the extent of error was not examined but was expected to be negligible. In fact, $\nu\Sigma_f$ in the blanket region is much smaller than that in the fuel region, so that the error in the predicted neutron flux in the blanket will not influence k_{eff} and power distribution to a significant extent.

On the above background, an extensive examination has been performed about the effects of the mesh sizes, the blackness of control rods, and the composition of fuel, blanket and reflector regions. The object of this survey is to know the limits of applicability of the coarse mesh calculation, which is an only practical way in the 3-dimensional analyses, in addition to know how much generality can be expected to HONEYCOMB in practical use. Thus, several parameters were varied so as to cover their ranges which can be considered in usual fast reactor systems. Two-dimensional 6-group criticality calculations were made with varying four kinds of parameters:

- (1) To examine the effect of control rod blackness, the densities of nuclides in the composition of control rod (mixture 2 in Fig. 2.7.1-3) were multiplied by factors 1, 3/2 and 2.
- (2) To examine the effect of the reactor scale, the compositions of a prototype FBR (MZB), an experimental FBR (JOYO) and a critical facility (ZPR-3-6F⁽⁴⁵⁾) were adopted for fuel, blanket and reflector regions.

TABLE 2.7.2-1 Calculated values of k_{eff} for various cases.
(M: Prototype FBR, J: Experimental FBR, Z: ZPR-3-6F⁽⁴⁵⁾)

Case No.	Blackness	Composition	Pitch of ○	With transport correction			Without t. c.	
				○	△ (1/6)	△ (1/24)	○	△ (1/6)
1	1	M	6	1	0.99118	0.99112	1.00610	0.98989
2	1	M	8	1	0.99131	0.99180	1.00954	0.99060
3	1	M	12	1	0.99028	0.99113	1.01251	0.99070
4	1	J	6	1	0.99343	0.99338	1.00270	0.99164
5	1	J	8	1	0.99341	0.99396	1.00520	0.99204
6	1	J	12	1	0.99259	0.99344	1.00732	0.99211
7	1	Z	6	1	0.99424	0.99354	1.00008	0.99278
8	1	Z	8	1	0.99325	0.99284	1.00143	0.99195
9	1	Z	12	1	0.99188	0.99186	1.00285	0.99098
10	1.5	M	6	1	0.98981	0.99081	1.01274	0.99025
11	1.5	M	8	1	0.98965	0.99159	1.01754	0.99093
12	1.5	M	12	1	0.98842	0.99058	1.02058	0.99118
13	1.5	J	6	1	0.99235	0.99361	1.00746	0.99139
14	1.5	J	8	1	0.99213	0.99423	1.01084	0.99175
15	1.5	J	12	1	0.99117	0.99330	1.01274	0.99193
16	1.5	Z	6	1	0.99372	0.99385	1.00232	0.99246
17	1.5	Z	8	1	0.99249	0.99316	1.00432	0.99141
18	1.5	Z	12	1	0.99085	0.99194	1.00602	0.99033
19	2	M	6	1	0.98823	0.99040	1.01963	0.99060
20	2	M	8	1	0.98786	0.99126	1.02554	0.99143
21	2	M	12	1	0.98676	0.98966	1.02810	0.99225
22	2	J	6	1	0.99103	0.99374	1.01266	0.99107
23	2	J	8	1	0.99070	0.99433	1.01666	0.99158
24	2	J	12	1	0.98990	0.99283	1.01792	0.99223
25	2	Z	6	1	0.99291	0.99411	1.00502	0.99187
26	2	Z	8	1	0.99150	0.99343	1.00765	0.99076
27	2	Z	12	1	0.98984	0.99187	1.00931	0.98995

- (3) The pitches of hexagonal lattices were made 6, 8 and 12cm.
- (4) Three cases of mesh structure were surveyed by making the number of nodal points in a hexagon 1, 6 and 24, the latter two cases of which correspond to triangular mesh structures.

Moreover, the cases without the transport correction to the control rod regions were also examined in order to confirm the effect of the correction.

The geometry used is that of Fig. 2.1.1-1 filling the 18 assemblies in the six corners with the composition of reflector. The values of k_{eff} are adjusted so that, in case of hexagonal mesh structure, k_{eff} becomes 1. (Here, the word 'hexagonal' is used to mean the cases of 1 nodal point in a hexagon.) The energy ranges of 6-group structure are: (1) 10.5MeV~1.4MeV, (2) 1.4MeV~0.4MeV, (3) 400keV~100keV, (4) 100keV~10keV, (5) 10keV~1keV, and (6) 1000eV~0.215eV.

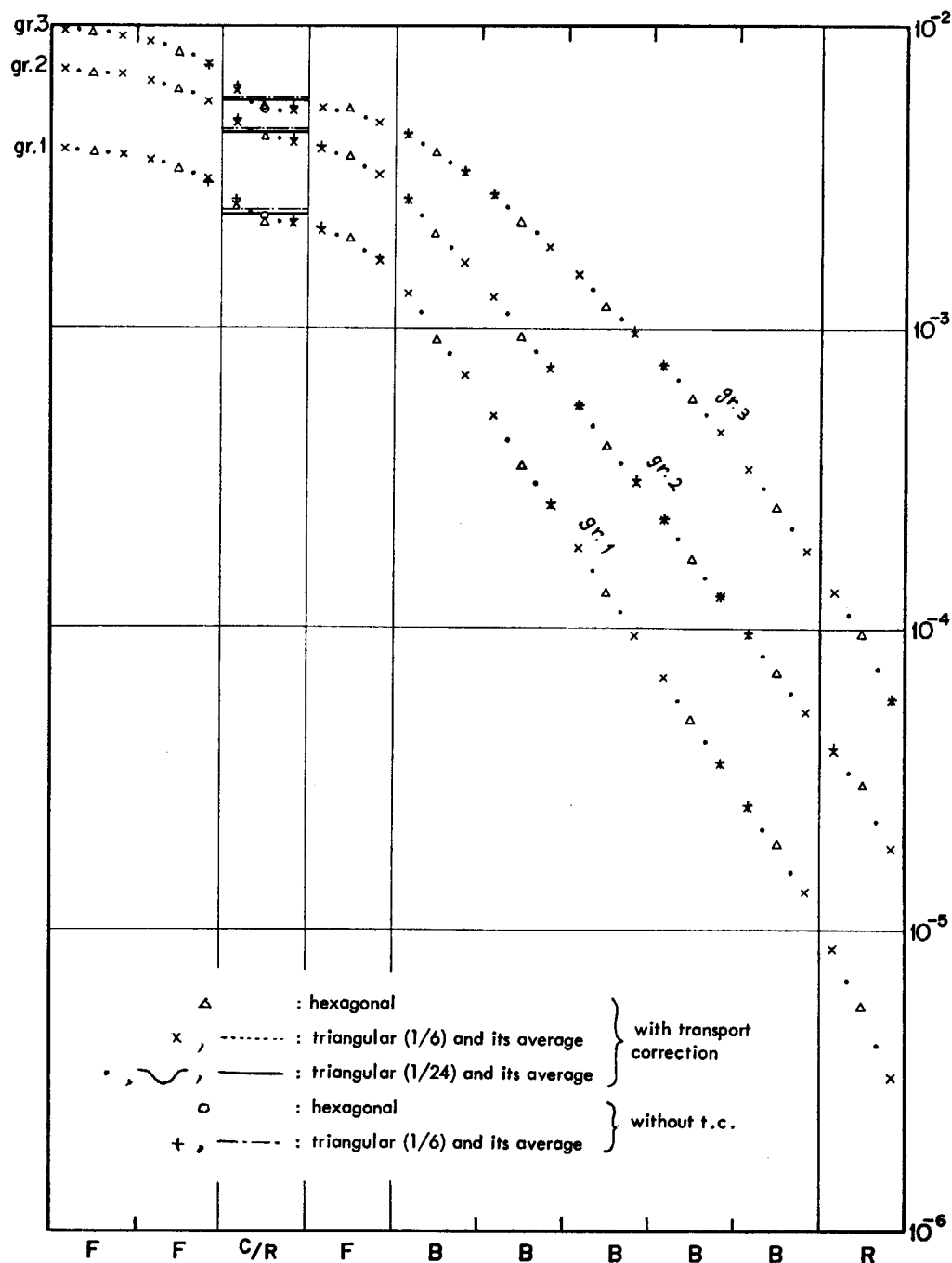


Fig. 2.7.2-1 Flux distribution for the case No. 5.

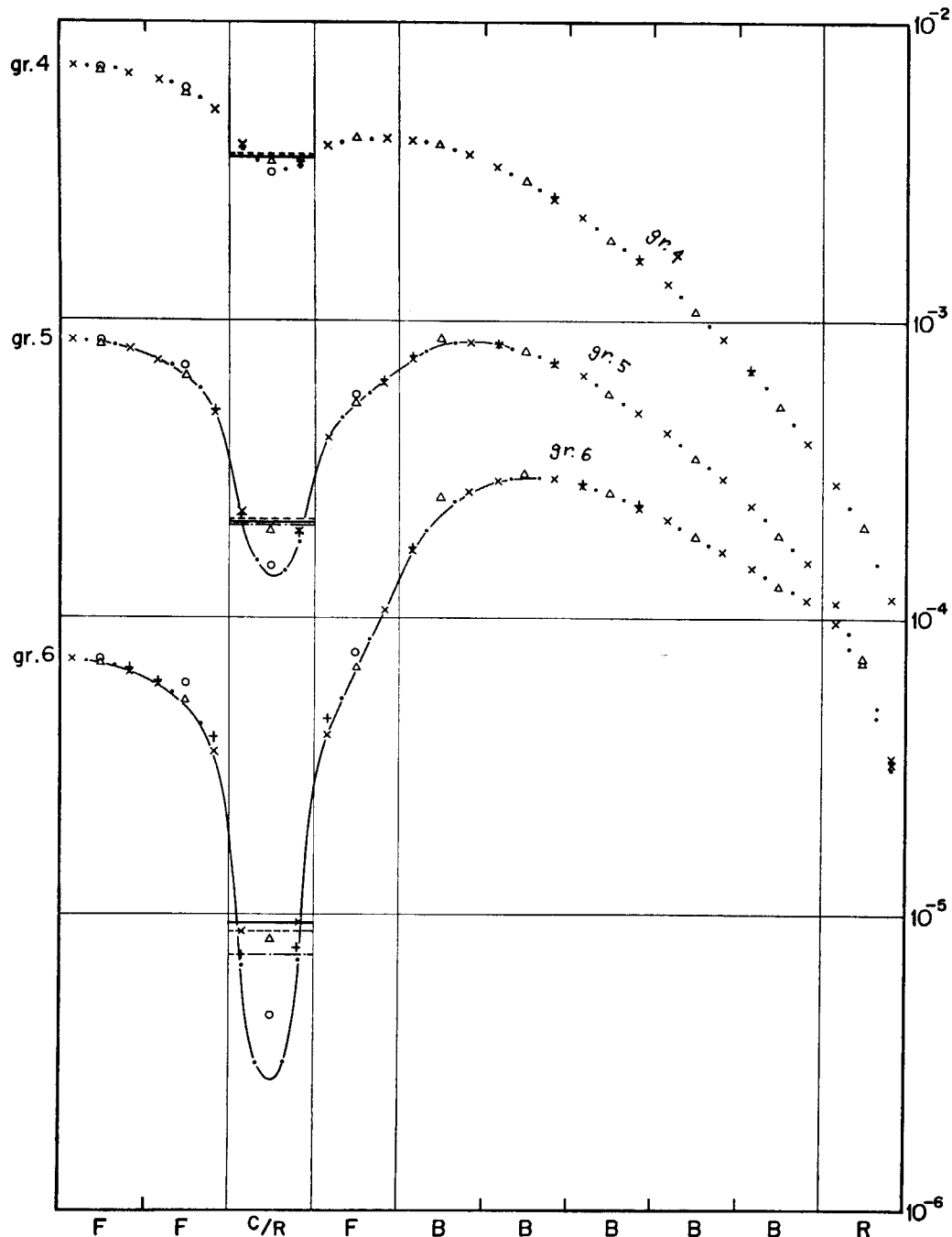


Fig. 2.7.2-2 Flux distribution for the case No. 5 (continued).

The values of k_{eff} are shown in TABLE 2.7.2-1. Considering the triangular cases (24 points) as the standard references, the errors of k_{eff} 's are within 1% except for the hexagonal cases without the transport correction. The satisfactory accuracy is obtained in the hexagonal cases with transport correction, considering the fact that the CPU time required is much shorter than that in cases of triangular mesh schemes. (The ratio of CPU time for the hexagonal, triangular (1/6) and super fine triangular (1/24) cases is about 1: 19: 280.) The error does not seem to depend on the blackness and the composition in the ranges surveyed. However, in case of composition of ZPR-3-6F, the error seems to be decreased by making the mesh sizes fine, that is, by making the pitch of hexagonal lattice small. It is known²⁴⁾ that S_n transport model evaluates k_{eff} somewhat larger than diffusion model. This fact gives an advantage to our results of hexagonal calculation with the transport correction.

Figures 2.7.2-1 and 2.7.2-2 show the flux distribution for the case No. 5, which is the typical case dealt with by this code HONEYCOMB. This distribution is along the traverse through the centers of 10 hexagons starting from the fuel assembly, which is adjacent to the upper left side of the central assembly, outgoing in the upper right direction (see the arrow shown in Fig. 2.1.1-1). Thus we can see the distribution through a control rod. In the control rod, especially for the groups 4~6, the effect of the transport correction can be observed (the mark Δ is nearer than the mark \circ to the average (—) of the finest case). For the groups 5 and 6, the gradient of the flux distribution has the opposite sign to that of the other groups, at the fuel/blanket interface. In these groups 5 and 6, the flux values (the mark Δ) in the first (lefttest) blanket assembly are estimated slightly large. The small difference of k_{eff} between hexagonal and super fine triangular methods in TABLE 2.7.2-1 will have come from the difference of flux values in the control rods and the above-mentioned blanket assemblies.

On the whole, the errors in the present method (the mark Δ) used in the code HONEYCOMB are small in the ranges surveyed here. It can be concluded that HONEYCOMB has a good applicability to the practical usages.

3. FDCAL-3, the Detailed Calculation Subsystem Predicting the JOYO Thermo-Hydraulic Characteristics

3.1 Summary of the Code FDCAL-3: the Combination of the Codes FDCAL-2 and FATEC-3

The FDCAL-3 is a combination of the FDCAL-2 which calculates a flow distribution in a reactor vessel and the FATEC-3 which analyzes a temperature distribution in a fuel assembly. The FDCAL-3 provides not only the functions, which the FDCAL-2 and the FATEC-3 possess, but also some additional options. The main features are summarized as follows;

(1) Calculation of the flow distribution in the reactor vessel

For the various flow channels between inlet and outlet plenums, the channel flow rates which correspond to pressure losses and power profiles are calculated. Dividing the flow channels into many groups depending on the channel geometry and the axial power profile, the FDCAL-3

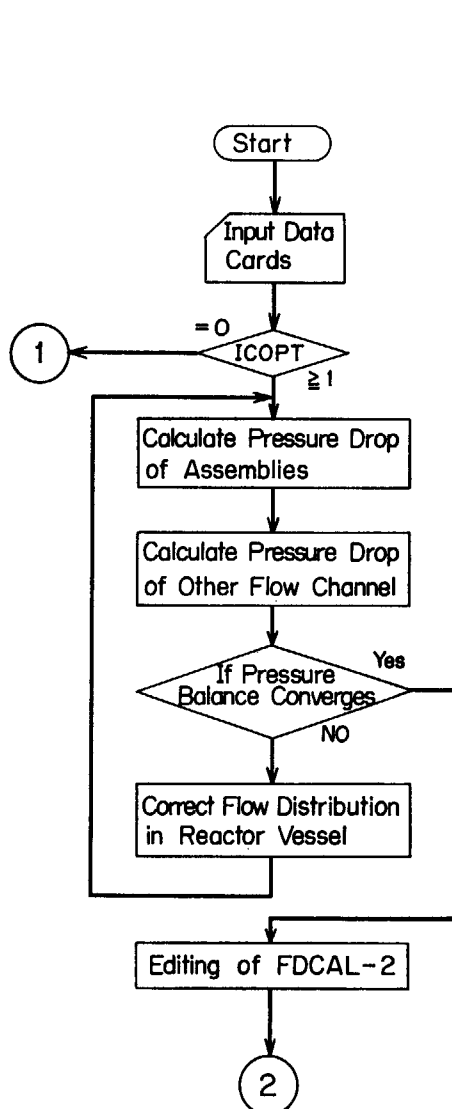


Fig. 3.1-1 Flow diagram of FDCAL-3.

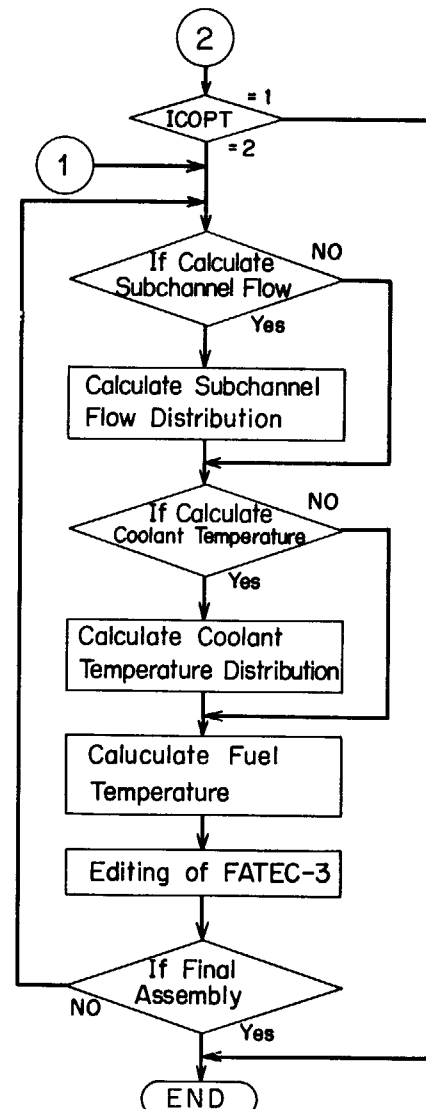


Fig. 3.1-2 Flow diagram of FDCAL-3.

treats a representative channel of the groups. The channel power distributions including the fission power and γ -ray heat are given by the code HONEYCOMB.

(2) Pressure drop of the fuel and blanket assemblies

Two options are provided for the total pressure drop calculation of an assembly depending on whether the power distribution in the fuel pins can be assumed to be uniform or not. Being assumed to be uniform, only three kinds of subchannels located at the corner, side and center in the assembly are considered without the thermal mixing effect. On the other hand, if not uniform, all subchannels in the assembly are treated with the thermal mixing effect.

(3) Calculation of the temperature distribution in the assembly

Both coolant and fuel element temperatures are calculated. The coolant temperature as well as the subchannel flow rates are obtained beforehand in the FDCAL-2 part. Thus only the fuel element temperature analysis is performed when the detailed subchannel model such as that with the thermal mixing effect is applied for calculating the pressure drop of an assembly. Except for the case mentioned above, the coolant temperature can, however, be recalculated and for temperature analysis in the assembly, the results of the FDCAL-2 can be used without recalculating the subchannel flow distribution by user's option.

The temperature of a fuel element is calculated with a 1-dimensional model (r) or a 2-dimensional model (r - θ) at each axial mesh point. That hot spot temperature analysis is also performed by the use of the nominal temperature and the uncertainty factor given by input data.

These temperature calculations are usually performed for the specified assemblies after the flow distribution calculation in the reactor vessel. The independent calculation for an assembly can also be permitted.

The conceptual flow diagram of the calculation is shown in Figs. 3.1-1 and 3.1-2.

3.2 Method for Calculating the Coolant Flow Distribution in the Reactor Vessel

3.2.1 Analytical Model and Equations for Predicting the Coolant Flow Distribution

(1) Arrangement of the coolant flow paths in the reactor vessel

The core configuration for fast breeder reactors consists of fuel assemblies, blanket assemblies, control rods, reflectors and neutron source element. In a region outside of the core, the racks (pots) for cooling spent fuel assemblies are arranged. The coolant flow paths in the reactor vessel consist of not only core components mentioned above but also auxiliary and emergency cooling systems and various leakage flows. The flow paths of JOYO are shown in Fig. 3.2.1-1 as an example.

The primary cooling system of JOYO is loop type and forms a closed loop with two primary loops, an auxiliary cooling system, and an overflow system. The primary coolant flows into the bottom of the reactor vessel through two inlet pipes and arrives at the inlet plenum. The coolant flow from the inlet plenum ramifies to the auxiliary cooling system, a leakage flow path to a low pressure plenum, fuel racks (pots) and a high pressure plenum. The coolant flow from the high pressure plenum furthermore diverges to two kinds of flow paths. One leads to the outlet plenum through core fuel assemblies, regulating rods and leakage paths through gaps. Another goes to the low pressure plenum through slit of reflectors and leakage paths, and from there, the coolant flow leads also to the outlet plenum through blanket fuel assemblies, reflectors, safety rods, and leakage paths.

FDCAL-3 calculates flow distributions in these flow channels placed between the inlet and outlet plenums. In FDCAL-3, the various flow channels are treated by grouping into six types of flow paths as shown in Fig. 3.2.1-2. The flow channels within each type are furthermore

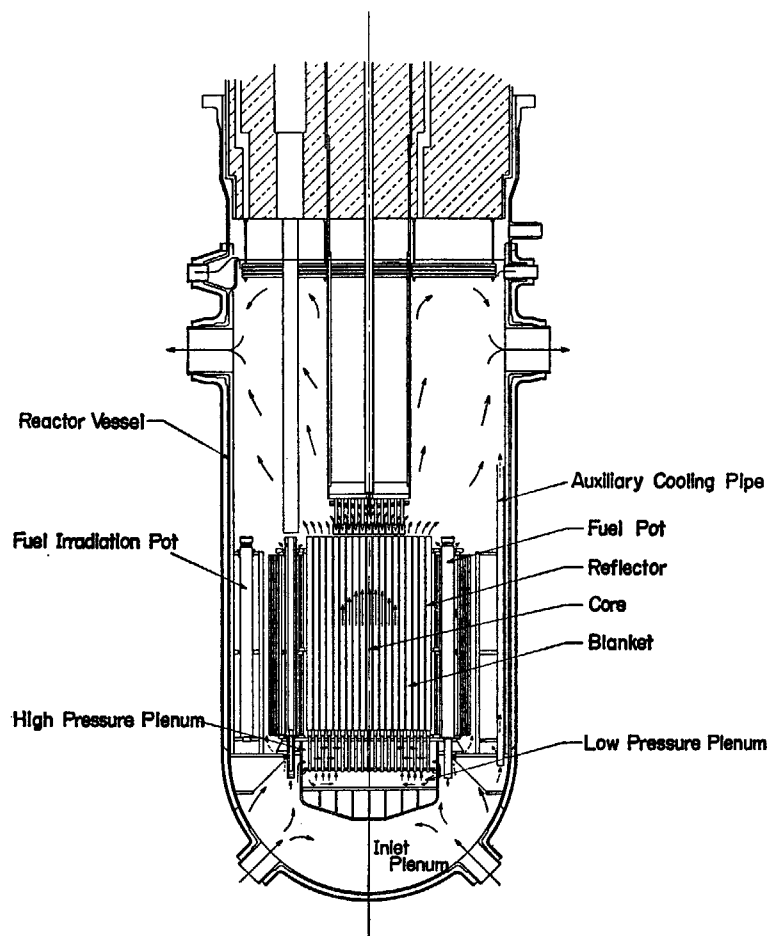


Fig. 3.2.1-1 Flow paths in the reactor vessel of JOYO.

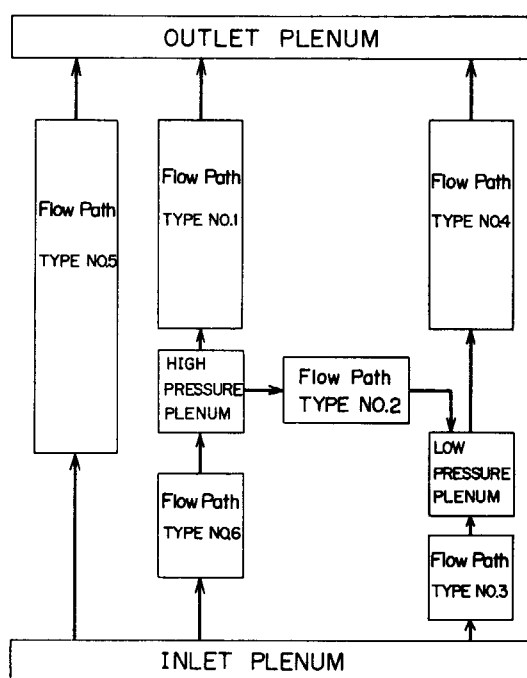


Fig. 3.2.1-2 Flow path type No. in the reactor vessel.

grouped into a number of kinds depending on geometry and axial power profile for each flow path. If axial power profile for the flow channels having the same geometry is assumed to be equal, the flow distribution in these flow channels is considered to be the same. Therefore it is sufficient to calculate the pressure drop for one of these paths.

(2) Analytical model

The flow distribution in these flow channels is calculated under following assumptions:

- (i) Pressure gradient in the high and low pressure plenums is uniform.
- (ii) Acceleration pressure drop of flow channels is neglected except for fuel and blanket assemblies.
- (iii) Frictional and gravitational pressure drops in flow channels except for the assemblies are calculated by taking account of the coolant property change due to the γ -heat generation.
- (iv) Pressure drop in the assembly is estimated by the method to be described in §3.3.
- (v) Flow distribution is calculated to achieve an equal pressure drop for each flow channel between the inlet and outlet plenums.

(3) Equations for the pressure drop calculation for flow channels except for the assembly:

The frictional pressure drop in each flow channel except for the assemblies is estimated by the use of the loss coefficient averaged over the channel.

Equation for the frictional pressure drop calculation in the flow channels (such as gas vent holes, fuel storage racks, regulating rods etc. which are contained in the Flow Path Type No. 1, 2, 3 and 5) is given by

$$\Delta P = K \frac{\gamma_0}{\gamma} \left(\frac{\gamma_0}{\gamma} \right)^{N-2} \left(\frac{\nu_0}{\nu} \right)^{N-2} W^N, \quad (3.2.1-1)$$

where

ΔP = frictional pressure drop (kg/m²),

W = coolant flow rate (kg/sec),

γ = coolant specific weight (kg/m³),

γ_0 = coolant specific weight at the reference temperature (kg/m³),

ν = coolant kinematic viscosity (m²/sec),

ν_0 = coolant kinematic viscosity at the reference temperature (m²/sec),

K = frictional loss coefficient,

N = exponent.

In the flow channels included in those of the Flow Path Type No. 2, the frictional pressure drops are calculated by the following two equations:

$$\Delta P = C_1 W_T^{n_1} + C_2 W^{n_2} \quad (3.2.1-2)$$

and

$$\Delta P = C W^N, \quad (3.2.1-3)$$

where

ΔP = pressure difference between high pressure and low pressure plenums (kg/m²),

W = coolant flow rate to low pressure plenum (kg/sec),

W_T = flow rate at connecting pipe inlet,

C_1, C_2, C = frictional loss coefficients,

n_1, n_2, N = exponents.

Eq. (3.2.1-2) is applied to the leakage paths through the connecting pipe gaps of the core assemblies and the regulating rods. This pressure drop is given by a function of the flow rate at the connecting pipe inlet and of the leakage flow rate to the low pressure plenum, whereas Eq. (3.2.1-3) is used for the leakage paths through the connecting pipe gaps of the safety rods, inner and outer blanket assemblies, and reflectors. The gaps of reflectors consist of two kinds such as mere connecting gap and a slit which is provided to regulate the flow rate to the low pressure plenum.

By using Eqs. (3.2.1-1)~(3.2.1-3) with the constants based on experiments, the frictional pressure drop from inlet to outlet for each flow path is calculated. Average coolant properties used for this calculation are estimated by considering the coolant enthalpy rise due to the γ -ray heat generations. The outlet enthalpy for each flow channel is given by

$$h_{\text{out}}^i = h_{\text{in}}^i + Q^i / W^i, \quad (3.2.1-4)$$

where

h_{out}^i = outlet coolant enthalpy in the i -th flow channel (kcal/kg),

h_{in}^i = inlet coolant enthalpy in the i -th flow channel (kcal/kg),

Q^i = heat generation rate in the i -th flow channel (kcal/sec),

W^i = mass flow rate in the i -th flow channel (kg/sec).

The relation of coolant enthalpy with temperature through the isobaric specific heat capacity $C_p(t)$ is given by

$$h(t) = \int_{98}^t C_p(t') dt'. \quad (3.2.1-5)$$

where $C_p(t)$ can be fitted by the following polynomial function of temperature²⁵⁾,

$$C_p(t) = C_{p0} + C_{p1}t + C_{p2}t^2, \quad (3.2.1-6)$$

where C_{p0} , C_{p1} and C_{p2} are specified constants. Thus Eq. (3.2.1-5) becomes an algebraic equation and its solution is obtained by Newton's method for a given value of $h(t)$. The outlet coolant density and the dynamic viscosity are calculated by the following two equations⁵¹⁾, respectively :

$$\gamma(t) = \gamma_0 + \gamma_1 t + \gamma_2 t^2, \quad (3.2.1-7)$$

$$\log_{10} \mu(t) = A_0 + \frac{A_1}{t + 273.2} - A_2 \log_{10}(t + 273.2), \quad (3.2.1-8)$$

where γ_0 , γ_1 and γ_2 , and A_0 , A_1 and A_2 are specified constants and $\mu(t)$ is the dynamic viscosity. Channel average coolant properties; γ and ν ($=\mu/\gamma$) are estimated in terms of algebraic mean.

3.2.2 Numerical Method for Pressure Balance Calculation

Flow distribution is calculated to make the pressure drop in each flow channel equal. The pressure balance is obtained from iteration procedures. Firstly, assuming the flow distribution in reactor vessel, the total pressure drops in all channels are calculated by the use of the equations given in §3.2.1 and §3.3.1. The iteration is continued until the total pressure drops in all channels converge within an acceptable tolerance.

The initial guess of the flow distribution is given as input data or calculated in the program by using the frictional loss coefficient. In the initial flow rate calculation, it is assumed that the gravitational pressure drops are equal for all channels and the accelerational pressure drops are neglected. By using these guesses, the pressure drops in channels are first calculated for each flow path type shown in Fig. 3.2.1-2. The program checks whether the convergence criterion is satisfied or not by the inequality :

$$\left| \frac{\Delta P_{\text{max}} - \Delta P_{\text{min}}}{\Delta P_{\text{min}}} \right| < \epsilon, \quad (3.2.2-1)$$

where

ϵ = input convergence criterion,

ΔP_{max} = maximum pressure drop between the inlet and outlet plenums,

ΔP_{min} = minimum pressure drop between the inlet and outlet plenums.

The ΔP_{max} and ΔP_{min} are obtained by taking account of the pressure drops for all channels from Flow Path Type No. 1 to No. 5. If the condition (3.2.2-1) is not satisfied, the assumed flow distribution is modified on the basis of the current average pressure drops in each flow path and between the inlet and outlet plenums. The average pressure drop without including

the gravitational force is obtained by means of the conservation of the total flow rate:

$$\Delta P_{av,f} = \left\{ \sum_i^N W_i \left/ \sum_i^N \sqrt{\frac{W_i^2}{(\Delta P_i - \Delta P_{ig})}} \right. \right\}^2, \quad (3.2.2-2)$$

where

W_i = flow rate in the i -th channel,

ΔP_i = total pressure drop in the i -th channel,

ΔP_{ig} = gravitational pressure drop in the i -th channel,

$\Delta P_{av,f}$ = average pressure drop without including the gravitational force,

N = total channel number.

On the other hand, the average gravitational pressure drop is calculated in terms of the algebraic mean written as

$$\Delta P_{av,g} = \sum_i^N \Delta P_{ig} / N. \quad (3.2.2-3)$$

The average pressure drop in each flow path or between the inlet and outlet plenums is given by

$$\Delta P_{av} = \Delta P_{av,f} + \Delta P_{av,g}.$$

By using these average pressure drops, the mass flow rate for each channel is corrected to give the following form:

$$W_i' = \left\{ W_i^2 \frac{\Delta P_{av} - \Delta P_{ig}}{\Delta P_i - \Delta P_{ig}} \right\}^{1/2}, \quad (3.2.2-4)$$

where

W_i = uncorrected flow rate in the i -th channel,

W_i' = corrected flow rate in the i -th channel,

ΔP_{av} = average pressure drop,

ΔP_{ig} = gravitational pressure drop in the i -th channel,

ΔP_i = total pressure drop in the i -th channel.

Finally, the corrected mass flow rate W_i' is renormalized by the total flow rate, and then new channel pressure drops are calculated. The flow diagram of these calculations is illustrated in Fig. 3.2.2-1.

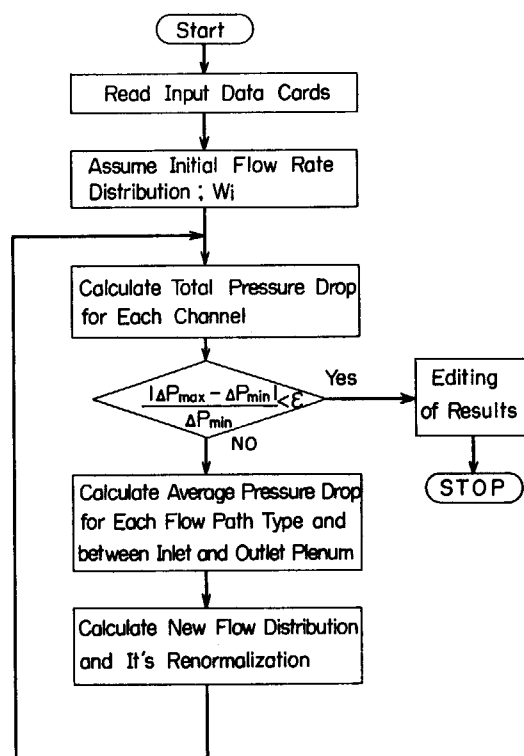


Fig. 3.2.2-1 Flow diagram of pressure balance calculation.

3.3 Method of Pressure Drop Calculation for the Assembly

3.3.1 Analytical Model and Equations for Pressure Drop Calculation

(1) Analytical model

The pressure drop calculation is carried out by dividing axially the assembly into the pin bundle part and other parts. The net pressure drop for the pin bundle part, in which fuel pins are triangularly arranged, is predicted by taking account of flow distribution because power distribution is already given three-dimensionally. The pressure drop for other parts is estimated by using the friction factor of Fanning type.

The flow distribution in the pin bundle is calculated by the use of a triangular subchannel model²⁶⁾. The subchannel analysis is an important tool to establish the thermal performance of the assembly because it deals with the distribution of coolant flow and enthalpy in the pin bundle. To predict the flow and enthalpy in selected regions of the pin bundle, FDCAL-3 uses a mathematical model taking account of the lateral mixing process, details of which will be described in §3.4. In this approach, the cross section of the pin bundle is divided into discrete flow subchannels as shown in Fig. 3.3.1-1. By making a suitable assumption concerning the flow and lateral mixing process in these subchannels, the equations expressing mass, momentum and energy balance can be derived for each subchannel. This set of equations can then be solved numerically by using the finite difference method.

Basic assumptions for deriving this set of equations are as follows.

- (i) For the lateral mixing process, FDCAL-3 considers only the thermal mixing effect between adjacent subchannels. This effect, which results from thermal conduction and turbulent crossflow, is assumed to be expressed in terms of an apparent heat transfer coefficient.
- (ii) Momentum interchanges are neglected between adjacent subchannels.
- (iii) Steady and one-dimensional single phase flow exists in each subchannel.
- (iv) The pressures over the cross sections of the pin bundle inlet and outlet are uniform, respectively.
- (v) FDCAL-3 also provides another subchannel model neglecting the mixing effect for the simplified calculations.

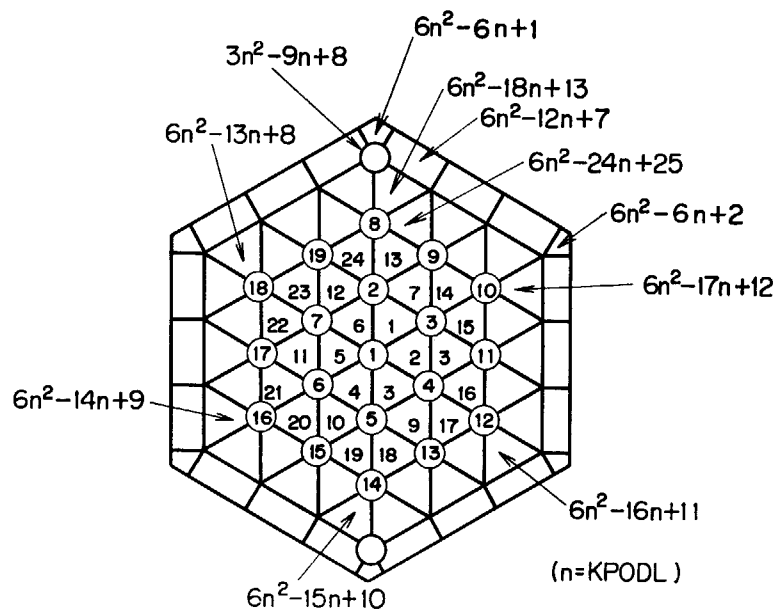


Fig. 3.3.1-1 Position and number of fuel element and flow subchannel.

(2) Analytical equations

In this section, equations are described for the pressure drop calculation in the assembly. The axial flow channel in the assembly consists of the pin bundle and other parts such as entrance nozzle, handling head etc. The frictional pressure drop in the assembly except for the pin bundle is calculated by the following two equations:

$$\Delta P = \frac{K}{\gamma} W^2 \quad (3.3.1-1)$$

where ΔP = frictional pressure drop (kg/m²),
 K = frictional loss coefficient,
 W = flow rate (kg/sec),
 γ = coolant specific weight (kg/m³).

This equation is applied to the entrance nozzle and to the diffuser in the JOYO assembly.

Another equation is given by

$$\Delta P = f \frac{L}{D} \frac{\gamma v^2}{2g}, \quad (3.3.1-2)$$

where f = Fanning friction factor,
 L = length of flow channel (m),
 D = equivalent diameter (m),
 g = gravitational acceleration (m/sec²),
 v = coolant velocity (m/sec).

Equation (3.3.1-2) is applied also to the flow channel below and upper the pin bundle, and handling head in the JOYO assembly.

The gravitational pressure drop for the flow channel is calculated in the same way as in §3.2. The accelerational pressure drop for flow channels except for the pin bundle is ignored because the power generation rate in this part can be assumed to be very small comparing with that in the pin bundle.

The equations of continuity of mass, momentum and energy for the pin bundle may be derived by using the basic assumptions. This gives a set of 3N first order ordinary differential equations, where N is the number of subchannels. These transport equations for the i -th subchannel can be written as follows:

$$\frac{dW_i}{dz} = 0 \quad (\gamma_i A_i v_i = \text{const.}), \quad (3.3.1-3)$$

$$\frac{W_i}{g} \frac{dv_i}{dz} + \frac{\gamma_i}{2g} \frac{f_i}{D_i} v_i^2(z) + \frac{\gamma_i(z_0)}{2g} f_{0i} v_i^2(z_0) \delta(z - z_0) + \frac{\bar{\gamma}_i}{2g} \bar{f}_i \bar{v}_i^2 + \gamma_i = -\frac{dP}{dz}, \quad (3.3.1-4)$$

$$W_i \frac{dh_i}{dz} = Q_i(z) + u_{ji} \{t_j(z) - t_i(z)\} + u_{ki} \{t_k(z) - t_i(z)\} + u_{li} \{t_l(z) - t_i(z)\}, \quad (3.3.1-5)$$

where W_i = flow rate in the i -th subchannel (kg/sec),
 v_i = coolant velocity in the i -th subchannel (m/sec),
 γ_i = specific weight in the i -th subchannel (kg/m³),
 f_i, f_{0i}, \bar{f}_i = Fanning friction factor in the i -th subchannel (kg/m³),
 D_i = equivalent diameter in the i -th subchannel (m),
 P_i = pressure in the i -th subchannel (kg/m²),
 h_i = enthalpy in the i -th subchannel (kcal/kg),
 Q_i = power addition rate to coolant in the i -th subchannel (kcal/sec·m),
 t_i = coolant temperature in the i -th subchannel (°C),

u_{ji} = apparent heat transfer coefficient to the j -th adjacent subchannel
(kcal/sec·°C·m),

A_i = flow cross-sectional area of the i -th subchannel (m²),

$\delta(z-z_0)$ = delta function,

$\bar{\gamma}_i$ = channel average specific weight (kg/m³),

\bar{v}_i = channel average coolant velocity (m/sec).

The continuity equation (3.3.1-3) states that the mass flow rate is axially constant for each subchannel. In the momentum equation (3.3.1-4), the terms on the left-hand side include the friction, spatial acceleration and elevation components of the pressure drop. The third term represents the friction component due to local sudden changes in the cross-sectional area. The fourth term gives the friction component expressed as channel average quantities. The right-hand side of the energy equation (3.3.1-5) describes mechanisms of thermal energy transport between the subchannels in the pin bundle. The first term is the power addition to the fluid of a subchannel and gives the rate of enthalpy change if no thermal mixing occurs. Other terms on the right-hand side represent the apparent heat transfer rate due to the thermal conduction and turbulent cross flow.

If the radial power distribution in the pin bundle is assumed to be uniform, FDCAL-3 permits an option for the subchannel model neglecting the thermal mixing effect. In this optional calculation, it is sufficient to set up only the flow channels with different shapes of the cross-sections as the subchannels. For the JOYO calculation, three subchannels of the corner, side and center subchannel are considered.

The Fanning friction factor correlation is assumed to be of the form:

$$f_i = a \{Re_i(z)\}^b + c, \quad (3.3.1-6)$$

where a , b and c are specified constants that depend upon the subchannel geometry, roughness and the Reynolds number; Re .

3.3.2 Numerical Method of Pressure Balance Calculation in Subchannels Consisting of Pin Bundles of Nuclear Fuel Elements

Equations (3.3.1-3) through (3.3.1-5) are solved as an initial value problem by using the finite difference method with the given inlet total flow rate, inlet coolant temperature, and axial power distribution for each fuel pin. Firstly, it is assumed that the flow rate for each subchannel is available to start the calculation. The energy equation (3.3.1-5) is solved by using the forward difference equation:

$$\begin{aligned} h_i(z+\Delta z) = & h_i(z) + \frac{Q_i(z)\Delta z}{\gamma_i(z)v_i(z)} + u_{ji} \{t_j(z) - t_i(z)\} \Delta z \\ & + u_{ki} \{t_k(z) - t_i(z)\} \Delta z + u_{li} \{t_l(z) - t_i(z)\} \Delta z. \end{aligned} \quad (3.3.2-1)$$

By using Eq. (3.2.1-5), the coolant temperature $t(z+\Delta z)$ is solved by the Newton method and coolant properties are calculated from Eqs. (3.2.1-6) and (3.2.1-7). The average specific weight $\gamma_{i,\Delta z}$ and average temperature $t_{i,\Delta z}$ between axial mesh points z and $z+\Delta z$ are estimated in terms of algebraic mean. By using this $\gamma_{i,\Delta z}$, the continuity equation is solved by

$$v_i(z+\Delta z) = \frac{W_i}{\gamma_{i,\Delta z} A_i}. \quad (3.3.2-2)$$

The momentum equation is also solved by the forward finite difference method:

$$\begin{aligned} \Delta P_i(z+\Delta z) = & P_i(z) - P_i(z+\Delta z) \\ = & \gamma_{i,\Delta z} \Delta z + \frac{\gamma_{i,\Delta z}}{2g} f_i \left\{ \frac{v_i(z) + v_i(z+\Delta z)}{2} \right\}^2 \frac{\Delta z}{D_i} + \dots \end{aligned}$$

$$+ \frac{W_i}{gA_i} \{v_i(z + \Delta z) - v_i(z)\}. \quad (3.3.2-3)$$

For calculating the Reynolds number, use is made of the average coolant properties and average velocity between axial mesh points z and $z + \Delta z$.

After these calculational steps proceed to the final mesh point, the program checks if the total pressure drop for each subchannel converges to within an acceptable tolerance. If convergence criterion is not satisfied, the assumed flow rate for each subchannel is corrected in the same manner as in §3.2.2 and the iteration proceeds until the criterion is satisfied.

3.4 Method of the Temperature Distribution Calculation in Coolant and Fuel Elements in the Assembly

3.4.1 Analytical Model and Equations for the Temperature Calculation

(1) Analytical model²⁶⁾

In order to calculate the temperature distribution in coolant and fuel elements in an assembly, we assume the following:

- (i) Fuel elements in an assembly are arranged in a triangular pattern.
- (ii) The cross section of subchannels remains constant for all axial locations.
- (iii) Coolant flows in a single phase.
- (iv) Coolant temperature in the subchannel is uniform in an axial plane.

For the calculation, first, the fuel assembly is divided into subchannels as shown in Fig. 3.4.1-1, and the subchannel and the element are numbered to form a relation with each other. Secondly, the coolant temperature in the subchannel is calculated and the fuel element temperatures (clad and pellet) are obtained by using the coolant temperature in the subchannels adjoined to that fuel element.

(2) Analytical equations

(a) Coolant temperature

We introduce an apparent heat transfer coefficient which is defined as representing an effect of thermal mixing between adjacent subchannels on the coolant temperature. Therefore, the differential equation for the coolant temperature rise is obtained from the heat balance using a differential quantity for the subchannel as shown in Fig. 3.4.1-1 in the z -direction. This has led to Eq. (3.3.1-5).

(b) Fuel element temperature

Two models are provided for the fuel element temperature calculation. The first is a simplified 1-dimensional model. This procedure may be suitable for the calculation of the case where the variation of the coolant temperature is small in subchannels adjoined to the fuel element.

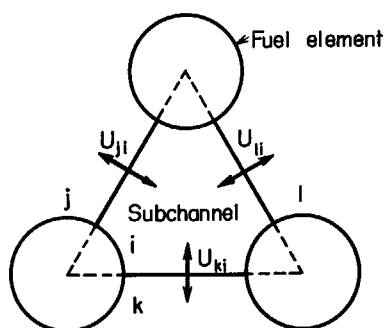


Fig. 3.4.1-1 Triangular lattice model.

For example, the radial power peaking is small in an assembly which is located near the center of a core. The second is a numerical 2-dimensional model. This method gives the results which are more realistic than the former and may be suitable for the assembly which has a large radial peaking factor²⁷⁾.

1) One-dimensional method

In order to calculate the temperature of clad and pellet in the axial direction with the 1-dimensional model, an average coolant temperature is defined as follows:

$$t_c(z) = \frac{\sum_i t_i(z) W_i}{\sum_i W_i}, \quad (3.4.1-1)$$

where t_c = average temperature of coolant adjoined to a fuel element (°C),
 t_i = coolant temperature in the i -th subchannel obtained by Eq. (3.3.1-5) (°C),
 W_i = flow rate in i -th subchannel (kg/sec).

The outer surface clad temperature is calculated by

$$t_{p1}(z) = \frac{q_L(z)}{h_1 \pi d_{p1}} + t_c(z), \quad (3.4.1-2)$$

where t_{p1} = outer surface clad temperature (°C),
 q_L = linear heat rate of a fuel element (kcal/m sec),
 d_{p1} = outer diameter of clad (m),
 h_1 = heat transfer coefficient (kcal/m²sec°C).

The heat transfer coefficient is written as:

$$h_1 = \frac{k}{de_p} Nu, \quad (3.4.1-3)$$

where $Nu = CON \cdot Re^\alpha \cdot Pr^\beta$, (3.4.1-4)

$$Re = \frac{de_p}{\nu} \cdot \frac{W_p}{\gamma A_p}, \quad (3.4.1-5)$$

k = coolant thermal conductivity (kcal/m sec°C),
 ν = coolant kinematic viscosity (m/sec²),
 γ = coolant specific weight (kg/m³),
 Pr = Prandtl number,
 W_p = flow rate related to the fuel element (kg/sec),
 (W_p is not the flow rate in the subchannel itself but is separately prepared.)
 de_p = hydraulic diameter (m),
 A_p = flow area (m²),

CON, α , β = constants.

The coolant properties are evaluated at the average coolant temperature for subchannels surrounding the fuel element. The W_p , de_p and A_p are arithmetic mean values for ambient subchannels.

On the other hand, the inner surface clad temperature is calculated by

$$t_{p2}(z) = \frac{q_L(z)}{2\pi k_p} \ln(d_{p1}/d_{p2}) + t_{p1}(z), \quad (3.4.1-6)$$

where t_{p2} = inner surface clad temperature (°C),
 k_p = clad thermal conductivity (kcal/m sec°C),
 d_{p2} = inner diameter of clad (m).

The outer surface fuel temperature is obtained from

$$t_{f1}(z) = \frac{q_L(z)}{h_2 \pi d_i} + t_{p2}(z), \quad (3.4.1-7)$$

where t_{f1} = outer surface fuel temperature (°C),

h_2 =gap conductance (kcal/m²sec°C),

d_f =fuel diameter (m).

In addition, the central fuel temperature is calculated by

$$t_{f2}(z) = \frac{q_L(z)}{4\pi k_f} + t_{f1}(z), \quad (3.4.1-8)$$

but, in the case where k_f is a function of temperature, the code uses the following equation,

$$\int_{\text{const}}^{t_{f2}(z)} k_f dt = \int_{\text{const}}^{t_{f1}(z)} k_f dt + \frac{q_L(z)}{4\pi}, \quad (3.4.1-9)$$

where

t_{f2} =central fuel temperature (°C),

k_f =fuel thermal conductivity (kcal/m sec°C).

2) Two-dimensional method

The fuel element is divided into six azimuthal sections in the case where defining lines of subchannels are drawn at the center line of the fuel element, but five sections for the fuel element adjoining to the wrapper tube. The fuel element is also divided into some sections in radial direction, and hence the sectors are formed. The heat balance for a typical sector (see Fig. 3.4.1-2) leads to the following equation:

$$\dot{Q}_1 = \sum_{i=1}^5 K_{i1}(t_i - t_1) + \dot{Q}_1'', \quad (3.4.1-10)$$

where

\dot{Q}_1 =total heat flow rate from the adjacent to the 1st sector (kcal/sec),

\dot{Q}_1'' =heat source in the 1st sector (kcal/sec),

K_{i1} =thermal conductance between the i -th and 1st sectors (kcal/m sec°C).

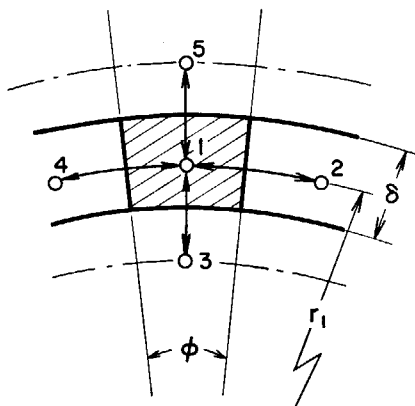


Fig. 3.4.1-2 General sector of fuel element.

General	Center	Boundary		
$K_{21} = K_{41} = k \frac{\delta}{r\phi}$ $K_{31} = k_{31} \frac{(r - \frac{\delta}{2})\phi}{\delta}$ $K_{51} = k_{51} \frac{(r + \frac{\delta}{2})\phi}{\delta}$	$K_{21} = K_{31} = \dots = K_{71}$ $= k \frac{\phi}{2}$	$K_{21} = k_{21} \frac{\delta}{2r\phi}$	$K_{21} = h_1 \cdot \phi \cdot r$	$K_{21} = h_2 \cdot \phi \cdot r_1$ $K_{12} = h_2 \cdot \phi \cdot r_2$

Fig. 3.4.1-3 Thermal conductances for various sectors.

The thermal conductances are evaluated for various sectors shown in Fig. 3.4.1-3. The dimension of the conductance is the same as the thermal conductivity for the unit axial length of the sector. For steady state conditions, the left-hand side of Eq. (3.4.1-10) is zero.

The fuel element temperature can now be calculated by applying Eq. (3.4.1-10) to all the sectors of the fuel element and using the coolant temperatures obtained from Eq. (3.3.1-5) for the boundary condition. An iteration method is used in the core. After the calculation of the k -th step, the $(k+1)$ st step temperature in the 1st sector is calculated from the following:

$$t_{1(k+1)} = \frac{\sum_{i=2}^5 K_{i1}^{(k)} t_i^{(k)} + \dot{Q}_1''}{\sum_{i=2}^5 K_{i1}^{(k)}} \quad (3.4.1-11)$$

(c) Hot spot temperature

The nominal temperature differences in the fuel element, obtained in the previous section, are defined as follows:

- coolant temperature rise Δt_1 ,
- temperature rise through film Δt_2 ,
- temperature rise through clad Δt_3 ,
- temperature rise at gap Δt_4 ,
- temperature rise through fuel Δt_5 .

Using these temperature differences Δt_j and uncertainties factors F_{ij} related to these differences, the statistical temperature effect Δt_s and cumulative temperature effect Δt_c are obtained as

$$\Delta t_s = \sqrt{\sum_{i=1}^I \left[\sum_{j=1}^5 \{ \Delta t_j (F_{ij} - 1) \} \right]^2} \quad (3.4.1-12)$$

$$\Delta t_c = \sum_{i=1}^I \left[\sum_{j=1}^5 \{ \Delta t_j (F_{ij} - 1) \} \right] \quad (3.4.1-13)$$

where I and I' are the numbers of statistical and cumulative uncertainty factors, respectively. Therefore, the hot spot fuel temperature t_{HS} can be expressed in the following way:

$$t_{HS} = t_N + \Delta t_s + \Delta t_c \quad (3.4.1-14)$$

where t_N is the nominal fuel temperature.

3.4.2 Numerical Method for Temperature Calculation

(1) Relation between fuel element and subchannel

As the fuel assembly is divided into sectors as explained in the previous section, the fuel element and subchannel numbers can be related as given in TABLE 3.4.2-1.

The addresses of the fuel elements and subchannels in the assembly are defined by the clockwise numbers in the code, as shown in Fig. 3.3.1-1. These relations can be described using the following parameters:

- (i) KPC is the number related to the i -th subchannel and the adjacent fuel elements as indicated in Fig. 3.4.2-1.
- (ii) NCC is the number of the other parts adjoining to the i -th subchannel (see Fig. 3.4.2-1).

TABLE 3.4.2-1 Relation between fuel elements and subchannel numbers

Concentric circle No. (KPODL)	2	3	4	5	6	7	8	9	10
Fuel element No. (KPMAX)*	7	19	37	61	91	127	169	217	271
Subchannel No. (NCMAX)*	18	42	78	126	186	258	342	438	546

* $KPMAX = 1 + 3(KPODL - 1) \times KPODL$, $NCMAX = 6\{1 + (KPODL - 1) \times KPODL\}$

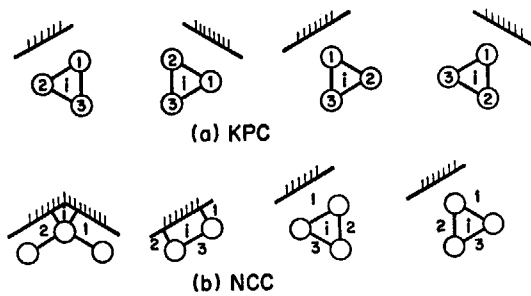


Fig. 3.4.2-1 Parameter of fuel elements and subchannel numbers.

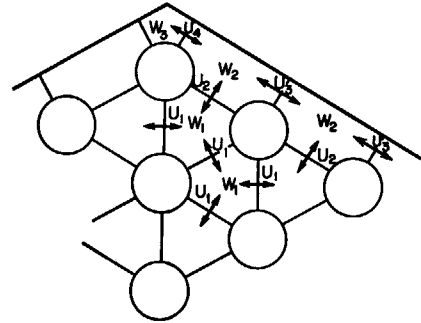


Fig. 3.4.2-2 Flow rate and apparent heat transfer coefficient in each subchannel.

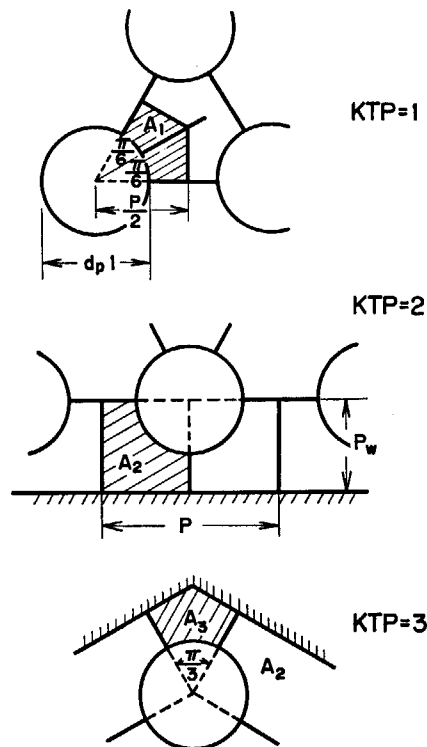


Fig. 3.4.2-3 Flow area corresponding to the place of fuel element.

(iii) NUC is the number of the apparent heat transfer coefficients corresponding to the i -th and adjacent subchannels as shown in Fig. 3.4.2-2.

(iv) KTP is the index related to the place of fuel elements in the assembly (see Fig. 3.4.2-3).

(v) NTC is the index related to the arrangement of subchannels, distinguishing between center, corner and side subchannels.

(2) Coolant temperature in subchannel

To obtain the coolant temperatures in the subchannels, the simultaneous ordinary differential equations, Eq. (3.3.1-5), is solved with the finite difference method under the following set of the boundary conditions:

$$\Delta t_1(0) = \Delta t_2(0) = \dots = \Delta t_N(0) = 0. \quad (3.4.2-1)$$

In the equations, the apparent heat transfer coefficients are expressed as a function of the Reynolds number in the following form:

$$U = A + B(Re)^C, \quad (3.4.2-2)$$

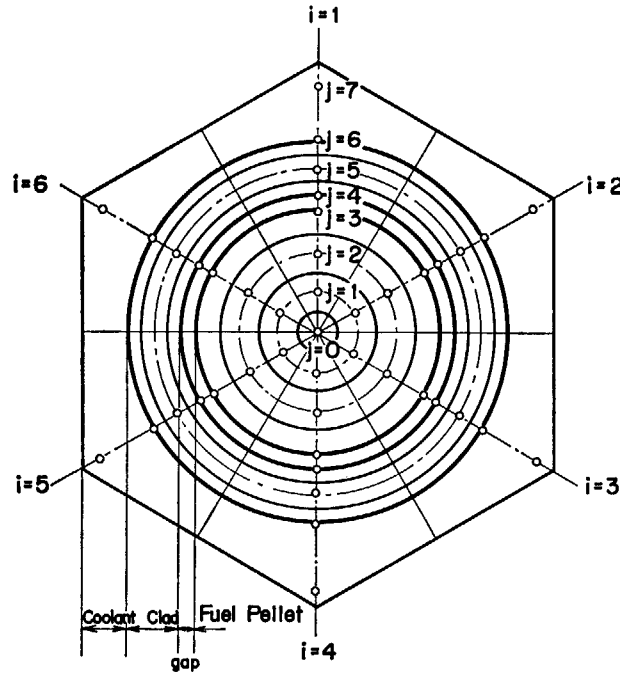


Fig. 3. 4. 2-4 Sector of a fuel element in two-dimensional model.

where A , B and C are constants that depend on the subchannel geometry, and the Reynolds number is the average over two subchannels. Also, the coolant flow rate in a subchannel can be calculated in such a manner that every pressure drop in a subchannel is the same. This calculational procedure is described in §3.3.1.

(3) Fuel element temperature calculations

In the code, there are two methods for the calculation of fuel element temperature as described in §3.4.1 (2). For the 1-dimensional procedure, the temperatures can be obtained analytically from Eq. (3.4.1-1) to Eq. (3.4.1-8). But, in the case where the fuel thermal conductivity varies with the fuel temperature, Eq. (3.4.1-9) is solved by an iteration method and the convergence is assumed to be achieved when the following condition is satisfied by all fuels:

$$\left| \int_{\text{const}}^{t_n} k_i dt - \int_{\text{const}}^{t_n} k_i dt - \frac{qL}{4\pi} \right| \leq \epsilon_t. \quad (3.4.2-3)$$

For the 2-dimensional procedure, the fuel element is divided into three sections of the clad and four of the fuel in the radial direction, while six sections for the fuel element at the central part and five sections for the fuel element adjoining to a wrapper tube in the azimuthal direction as shown in Fig. 3.4.2-4. To solve Eq. (3.4.1-11) for these sectors, we can rewrite it in the form:

$$t_1^{(k+1)} = t_1^{(k)} + \omega \left\{ \frac{\sum_{i=2}^5 K_{i1}^{(k)} t_i^{(k)} + \dot{Q}_1''}{\sum_{i=2}^5 K_{i1}^{(k)}} - t_1^{(k)} \right\}, \quad (3.4.2-4)$$

where ω is an acceleration factor. If the heat of each sector will be balanced, the brackets on the right-hand side of Eq. (3.4.2-4) approaches zero. Therefore, to decide the convergence of Eq. (3.4.2-4), a parameter is defined as follows:

$$e_1^{(k)} = \omega \left\{ \frac{\sum_{i=2}^5 K_{i1}^{(k)} t_i^{(k)} + \dot{Q}_1''}{\sum_{i=2}^5 K_{i1}^{(k)}} - t_1^{(k)} \right\}, \quad (3.4.2-5)$$

In the calculation, the iterations are continued until the largest value of e_1 for all sectors is less than or equal to a given value of ϵ_s . That is, the convergence criterion results in

$$\max |e_1| \leq \epsilon_s. \quad (3.4.2-6)$$

The heat transfer coefficient in the sector adjoining to the coolant is calculated by Eq. (3.4.1-3), and flow area, hydraulic diameter and flow rate are obtained with the configuration as shown in Fig. 3.4.2-3.

3.5 Examples of Calculational Results of the Code FDCAL-3

In this section, calculational results are presented about an example problem for the code FDCAL-3. For the calculational object, we adopted an almost similar model of MARK 1 core configuration of "JOYO", but not the exact one.

The core includes sixty-seven fuel assemblies and fifteen reflectors with slit, and is at power output of 50 MW. The fuel assemblies are divided into five zones according to the friction loss coefficients for the entrance nozzles. In calculating the flow distribution over the reactor vessel, the detailed subchannel model with the thermal mixing effect is applied to one assembly in the central zone.

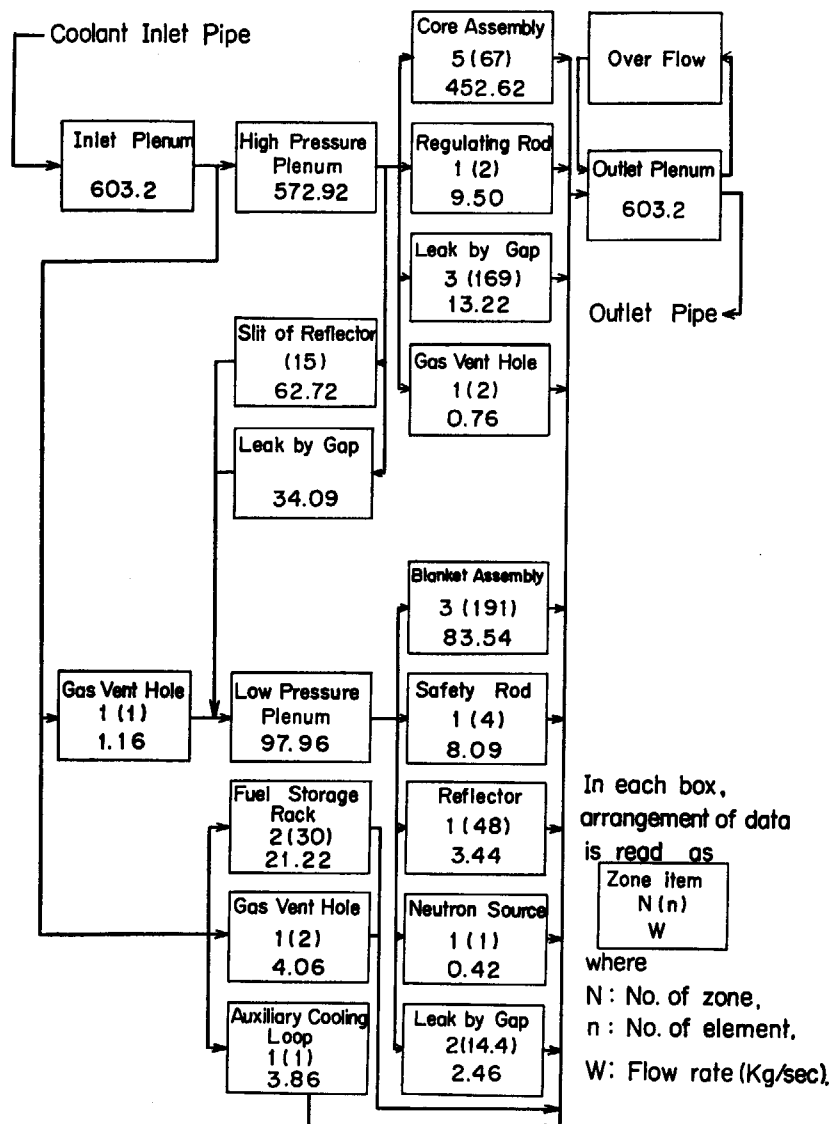


Fig. 3.5-1 Calculated values of flow distribution for the sample problem.

TABLE 3.5-1 Pressure drops in the reactor vessel for the sample problem

Pressure drops	Low pressure plenum to outlet plenum	High pressure plenum to outlet plenum	Inlet plenum to outlet plenum
kg/cm ²	0.362	2.473	2.602

TABLE 3.5-2 Subchannel flow rate and outlet temperature for the assembly in the central zone

Subchannel number	1 (center)	180 (side)	186 (corner)
Subchannel flow rate (kg/sec)	0.0346	0.0770	0.0164
Outlet temperature with thermal mixing (°C)	506.2	465.9	465.3

For the other assemblies, the subchannel model without thermal mixing has been used. The axial power profile is assumed to be common for the assemblies in each zone and the radial power distribution in each assembly is assumed to be uniform.

Figure 3.5-1 shows the values of the obtained flow distribution over the reactor vessel. The results of the pressure drops corresponding to this flow distribution are given in TABLE 3.5-1. In this calculation, the convergence criterion in Eq. (3.2.2-1) equals 10^{-3} . These calculational results seem comparable to the JOYO design calculations.

TABLE 3.5-2 shows the coolant flow rates and the outlet temperatures in such three representative subchannels as center, side and corner subchannels. These flow rates and outlet temperatures are calculated in the model with the thermal mixing effect, that is, by Eq. (3.3.1-5).

From these results, it can be said that the FDCAL-3 has proved the reasonable applicability of the calculational models. However, it is a future problem to confirm the accuracy of the results obtainable by the FDCAL-3 by various kinds of experiments including the full scale experiments.

4. Concluding Remarks

We have described, in this Part 2, the outline of the detailed nuclear and thermo-hydraulic calculation subsystems, HONEYCOMB, FDCAL and FATEC, which have been developed since 1971.

Many special efforts were necessary to realize the 3-dimensional criticality calculations in HONEYCOMB with sufficient accuracy and within the practical limit of computation time. For this purpose, an effective method has been developed for enhancing the accuracy of predicted neutron fluxes inside and in the vicinity of control rods. In addition, another efficient method has been developed to obtain the detailed power distribution for each pin in the fuel and blanket assemblies. The burn up can also be predicted for fuel pins in a few assemblies. It has become possible to perform the criticality search by adjusting insertion depth of control rods, as well as the calculation of kinetics parameters and 3-dimensional distribution of adjoint neutron flux. Moreover, the distribution of power generation rate is estimated containing the effect of neutron-induced γ -rays.

The FDCAL and FATEC have been combined into one thermo-hydraulic subsystem, FDCAL-3. This subsystem gives flow distributions in many coolant channels in the reactor vessel as well as temperature distributions. In addition, the hot spot temperature can be estimated in some specified assemblies. Thus, the method has been established for confirming the operational safety.

These detailed calculations supply the fundamental data to the SMART-MASTOR combination described in Part 1. They are also used for producing reference solutions of nuclear and thermo-hydraulic characteristics, which are used to confirm the accuracy of the simplified calculations performed by SMART.

On the basis of the present subsystems for detailed calculations, more general code systems will be able to be developed in the future, for dealing with not only the experimental fast reactors but also the prototype and commercial fast reactors. For this purpose, it is necessary to adopt the feed-back of informations from the experiments, and to enhance the accuracy of various data as well as methods of analyses.

Acknowledgments

The authors are indebted to Dr. T. Asaoka for his critical reading of this report. They are also grateful to Miss Y. Kaibara, Mrs. N. Hokari, Miss Y. Suzuki and Miss N. Ohnuki for their sincere helps in typing of this manuscript and tracing of figures.

References

- 1) KATSURAGI, S., TONE, T. and HASEGAWA, A.: "JAERI Fast Reactor Group Constants Systems, Part I", JAERI 1195, (1970).
KATSURAGI, S., ISHIGURO, Y., TAKANO, H. and NAKAGAWA, M.: "JAERI Fast Reactor Group Constants Systems, Part II-1", JAERI 1199 (1970).
KATSURAGI, S., TAKANO, H., NAKAGAWA, M. and HASEGAWA, A.: "JAERI Fast Reactor Group Con-

- stants—Supplement No. 1—”, JAERI 1199 (Supplement), (1971).
- 2) SUZUKI, T.: “EXPANDA-4, The One-Dimensional Diffusion Equation Code for Fast Reactors Using the JAERI-Fast Set”, JAERI-memo 3660, (1969) (in Japanese).
 - 3) ABAGYAN, L. P., BAZAZYANTS, N. O., BONDARENKO, I. I. and NIKOLAEV, M. N.: “Group Constants for Nuclear Reactor Calculations”, Authorized translation from the Russian, Consultants Bureau Enterprises, Inc., (1964).
 - 4) SUZUKI, T. and KATSURAGI, S.: “EXPANDA-2, Improvement of EXPANDA, The One-Dimensional Diffusion Equation Code for Fast Reactors”, JAERI 1118, (1966) (in Japanese).
 - 5) SUZUKI, T.: “SDRC, The Ultra-Fine Spectrum Calculation Code in Resonance Energy Region”, JAERI-M 4481, (1971) (in Japanese).
 - 6) SUZUKI, T. and KATSURAGI, S.: “EXPANDA-5, The One-Dimensional Diffusion Equation Program for Fast Reactors Consisting of Two-Region Hexagonal Lattices”, JAERI 1210, (1972).
 - 7) MIYASAKA, S., TAJI, Y. *et al.*: “A Code System for the Calculation of Radiation Heating”, Proceedings of AESJ 1973 Topical Meeting on Fast Reactor Physics, B10, p. 190, (1973) (in Japanese).
 - 8) FORD, W. E. and WALLACE, D. H.: “POPOP 4, A Code for Converting Gamma-Ray Spectra to Secondary Gamma-Ray Production Cross Sections”, CTC-12, (1969).
 - 9) DUDZIAK, D. J.: “ENDF Format and Procedures for photon Production and Interaction Data”, LA-4549 (ENDF-102), Rev. Vol. II, (1971).
 - 10) HASEGAWA, A. and KATSURAGI, S.: “A Code System PROF-GROUCH-G-II”, (to be published).
 - 11) DUDZIAK, D. J., SEAMON, R. E. and SUSCO, D. V.: “LAPHANO, A P_0 Multigroup Photon-Production Matrix and Source Code for ENDF”, LA-4750-MS (ENDF-156), (1972).
 - 12) MIYASAKA, S., TAJI, Y. *et al.*: “Code System for the Radiation-Heating Analysis of a Nuclear Reactor, RADHEAT”, JAERI-M 5794, (1974) (in Japanese).
 - 13) FOWLER, T. B. and Tobias, M. L.: “EQUIPOISE-3, A Two-Dimensional, Two-Group, Neutron Diffusion Code for the IBM-7090 Computer”, ORNL-3199, (1962).
 - 14) SUZUKI, T.: “Improvement of Coarse Mesh Difference Diffusion Scheme about Control Rods”, *J. Nucl. Sci. Technol.*, **12** [11], 695~702 (Nov., 1975).
 - 15) FRANCESCON, S.: “The Winfrith DSN Programme”, AEEW-R 273, (1963).
 - 16) HONECK, H. C.: “THERMOS, A Thermalization Transport Theory Code for Reactor Lattice Calculations”, BNL-5826, (1961).
 - 17) DAVISON, B. and SYKES, J. B.: “Neutron Transport Theory”, Chap. XV (1958), Oxford Univ. Press.
 - 18) SUZUKI, T.: “FURNACE, The Two-Dimensional Burn-up Code for Fast Reactors”, JAERI 1164, (1968) (in Japanese).
 - 19) LATHROP, K. D.: “GAMLEG, A Fortran Code to Produce Multigroup Cross Sections for Photon Transport Calculations”, LA-3267, (1965).
 - 20) KEEPIN, G. R.: “Physics of Nuclear Kinetics”, Chap. 2-1 (1965), Addison-Wesley Publishing Co. Inc.
 - 21) SUZUKI, T. and KATSURAGI, S.: “A Method of Calculation of Detailed Power Distribution in Fuel Assemblies”, *J. Nucl. Sci. Technol.*, **13** [7], 348~357 (July, 1976).
 - 22) COURANT, R. and HILBERT, D.: “Methods of Mathematical Physics”, Vol. II, “Partial Differential Equations” by R. COURANT, Chap. IV (1962), Interscience Publishers.
 - 23) MORSE, P. M. and FESHBACH, H.: “Methods of Theoretical Physics”, Pt. 1, § 7.2 (1953), McGraw-Hill Book Company Inc.
 - 24) BAKER, A. R.: “Comparative Studies of the Criticality of Fast Critical Assemblies”, ANL-7320, pp. 116~129 (1966).
 - 25) GOLDEN, G. H. *et al.*: “Thermophysical Properties of Sodium”, ANL-7323, (1967).
 - 26) MIYAMOTO, Y.: “Temperature Analysis for the Fuel Subassembly of Sodium Cooled FBR (Code; FATEC-2-ROD)”, JAERI-M 5119, (1973) (in Japanese).
 - 27) MIYAMOTO, Y.: “Method of Core Thermal Calculation for Multichannel on Sodium Cooled FBR”, *J. Nucl. Sci. Technol.*, **9** [3], 186~188 (March, 1972).
 - 28) KATSURAGI, S. *et al.*: “JOYPAC System, Part 1” JAERI 1246, (1976).